CZECH TECHNICAL UNIVERSITY IN PRAGUE

FACULTY OF MECHANICAL ENGINEERING

MASTER´S THESIS

2018

JAN RŮŽIČKA

Affidavit

I hereby declare that this document has been written only by the undersigned under the supervision of Ing. Hygreeva Kiran Namburi from Research Center Řež. Furthermore, I confirm that no sources have been used in the preparation of this document other than those indicated in the thesis itself.

Čestné prohlášení

Prohlašuji, že tento dokument byl napsán pouze níže podepsanou osobou pod vedením Ing. Hygreeva Kiran Namburi z Centra výzkumu v Řeži. Dále prohlašuji, že při tvorbě tohoto dokumentu nebyly použity žádné jiné zdroje než ty, které jsou v dokumentu uvedené.

Date: ………………., Location: ………………., Signature: ………………..

(Datum)   (Místo)   (Podpis)

Abstract

This master´s thesis deals with high-temperature nanoindentation testing of ferritic/martensitic steels, specifically the EUROFER 97. The content of this work starts with a study of present reactor materials, their behaviour and degradation. Conventional methods of mechanical testing to determine the irradiated material properties are briefly described, to be able to compare them with nanoindentation technique that is introduced in greater context. The work then continues with an experimental part that contains metallography, microscopy and the nanoindentation itself. The nanoindentation was conducted on three areas - electro etching/polishing and OPS, at temperatures ranging from 23°C up to 700°C under load range of - 5, 10, 50 and 100 mN. Finally, a series of recommendations based on presented results and subsequent discussion was derived as a conclusion of this thesis.

Key words: ferritic/martensitic steel, EUROFER 97, nanoindentation, hardness, reduced modulus, high-temperature testing

Abstrakt

Tato diplomová práce se zabývá vysokoteplotní nanoindentací feriticko-martenzitických ocelí, konkrétně oceli EUROFER 97. Obsah práce začíná studií o současných reaktorových ocelích, jejich chování a degradaci. Následuje stručný popis metod mechanického testování ozářených materiálů za účelem porovnání s technikou nanoindentace, která je popsána v širším kontextu. Experimentální část zahrnuje metalografickou přípravu, analýzu pomocí několika metod mikroskopie a samotnou nanoindentaci. Ta byla provedena na třech oblastech s odlišnou finální povrchovou úpravou – elektrolytické leptání/leštění a OPS, při teplotách od 23°C do 700°C, v rozsahu zatížení – 5, 10, 50 a 100 mN. Na závěr jsou uvedena doporučení týkající se postupu přípravy vzorků i nanoindentace založená na diskutovaných výsledcích.

Klíčová slova: feriticko-martenzitické oceli, EUROFER 97, nanoindentace, tvrdost, redukovaný modul pružnosti, vysokoteplotní zkoušky

Acknowledgement

This master´s thesis would not be possible without a support from many researchers and technicians from the Department of Structural and System Diagnostics in Research Center Rez. I am very grateful especially to Bc. Ondřej Libera for his guidance through the operation of the nanoindenter, to Ing. Jan Procházka for a help during the software evaluation of acquired data and to Ing. Klára Řezánková, Ph. D. for the atomic force microscopy. Last, but not least, I thank to Ing. Hygreeva Kiran Namburi for his expert advices and comments over the entire period of working on this master´s thesis.

Poděkování

Sepsání této diplomové práce by nebylo možné bez podpory mnoha vědeckých i technických pracovníků oddělení Strukturální a Systémové Diagnostiky Centra výzkumu v Řeži. Jsem velmi vděčný zejména Bc. Ondřeji Liberovi za jeho vedení při práci s nanoindentorem, Ing. Janu Procházkovi za pomoc při softwarové analýze naměřených dat a Ing. Kláře Řezánkové, Ph.D. za provedení mikroskopie atomárních sil. V neposlední řadě bych chtěl poděkovat Ing. Hygreeva Kiran Namburimu za jeho odborné rady a připomínky v průběhu tvorby této diplomové práce.

Contents

Abbreviations

AFM … Atomic Force Microscopy

BCC … Body-Centered Cubic Structure

CSM … Continuous Stiffness Measurement

EAC … Environmentally Assisted Cracking

EBSD … Electron Back-Scatter Diffraction

EDX/EDS … Energy Dispersive X-ray Spectroscopy

EE … Electrolytical Etching

EP … Electrolytical Polishing

FCC … Face-Centered Cubic Structure

FM … Ferritic/Martensitic

Gen IV … Gereration IV Reactors

IAEA … International Atomic Energy Agency

ISE … Indentation Size Effect

LOM … Light Optical Microscopy

LWR … Light Water Reactor

NPP … Nuclear Power Plant

ODS … Oxide Dispersion-Strengthened

OPS … Colloidal Silica Polishing Suspension

PWR … Pressurized Water Reactor

RAFM … Reduced Activation Ferritic/Martensitic Steel

RPV … Reactor Pressure Vessel

RT … Room Temperature

RVI … Reactor Vessel Internals

SC … Structures and Components

SCC … Stress Corrosion Cracking

SEM … Scanning Electron Microscopy

SPM … Scanning Probe Microscopy

SS … Stainless Steel

VVER … Water-Water Power Reactor

1. Introduction

As of January 7th 2018, there are 448 nuclear power reactors in operation worldwide according to the International Agency for Atomic Energy (IAEA) Power Reactor Information System. Vast majority of them (367) are light water cooled and moderated reactors (LWRs), out of which 291 are pressurized water reactors (PWRs) that were developed in 60's from the technology originally used as a propulsion for navy ships and submarines. Although the PWRs serve as a very reliable source of energy for many decades, currently emerging technologies - Generation IV (Gen IV) and fusion, have very different operational conditions and environments that require new structural materials to be developed as well as qualify the current materials applicability in advanced technologies. Knowledge about material behavior and degradation under extreme operational conditions (neutron irradiation, high temperatures, high stresses and coolant environment) is crucial for a successful life extensions of nuclear power plants and possible improvements. An in-depth understanding about irradiated material behavior is achieved by bridging link between experimental testing, modelling and simulations. (1)

1.1.   Review on PWR Materials and Their Chemical Composition

PWRs use in their primary circuit wide variety of materials. The piping and vessel is usually forged out of ferritic/martensitic (FM) steel using the austenitic steel as an inner cladding. Then there is a zirconium alloy creating the wall of the fuel rod and nickel alloys that are used on steam generator tubes. Materials can be also divided on in-core and ex-core, according to their exposure to neutron fluence. This work focuses primarily on FM steels (specifically the EUROFER 97) as structural materials and their development for the purposes of Gen IV and fusion. FM steels were chosen mostly because of their higher swelling resistance, higher thermal conductivity, lower thermal expansion and better liquid-metal compatibility than e.g. austenitic steels.
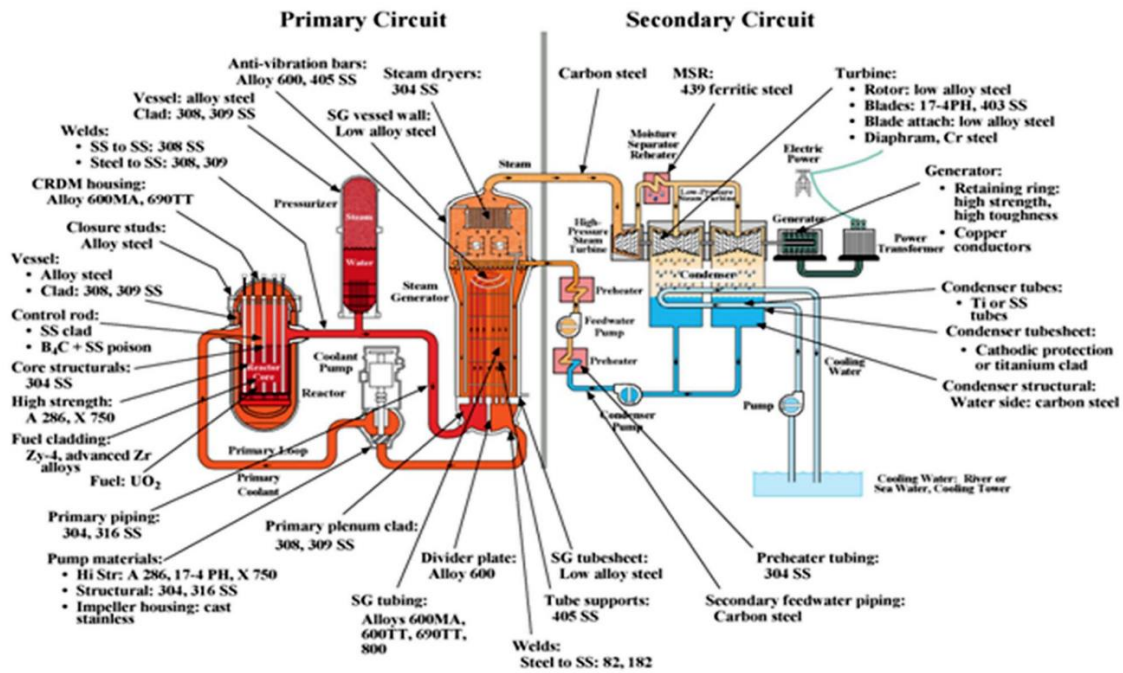
Figure 1: Sampling of the typical materials in a pressurized water reactor; from: Light Water Reactor Sustainability - Materials Aging and Degradation Pathway Technical Program Plan, U.S. DoE, September 2012

An ordinary steel is made mostly of ferrite (α-phase iron) with a small amount of pearlite (α-phase iron + cementite Fe_3C). Because the ferrite is ductile, it is desirable to increase the portion of pearlite in material, which is much harder, but also a brittle phase. This is done by increasing the level of carbon in the steel. In order to get austenitic material, the austenitic phase (γ-phase iron) must be stabilized with some alloying elements like nickel that prevents the recrystallization of austenite back into ferrite/pearlite mixture at temperatures of approximately 770°C. The body-centered cubic structure of an α-phase iron meanwhile transforms into face-centered cubic structure of the austenite. If the austenite is quenched rapidly under the critical temperature, a meta-stable phase called martensite is obtained. The martensite is a brittle phase, with very high strength and low ductility. On the contrary to the cubic configurations of all preceding phases, the martensite has a tetragonal body-centered structure. This change in the structure happened during an abrupt reorientation of Fe and C atoms caused by quenching. For a better idea about the phase transformations you can see the Fe – Fe_3C diagram shown in the figure 2. Unfortunately, as a metastable non-equilibrium phase the martensite cannot be shown in the diagram. Properties of all four mentioned phases are utilized with respect to the specific structure or component within the NPP. (2)
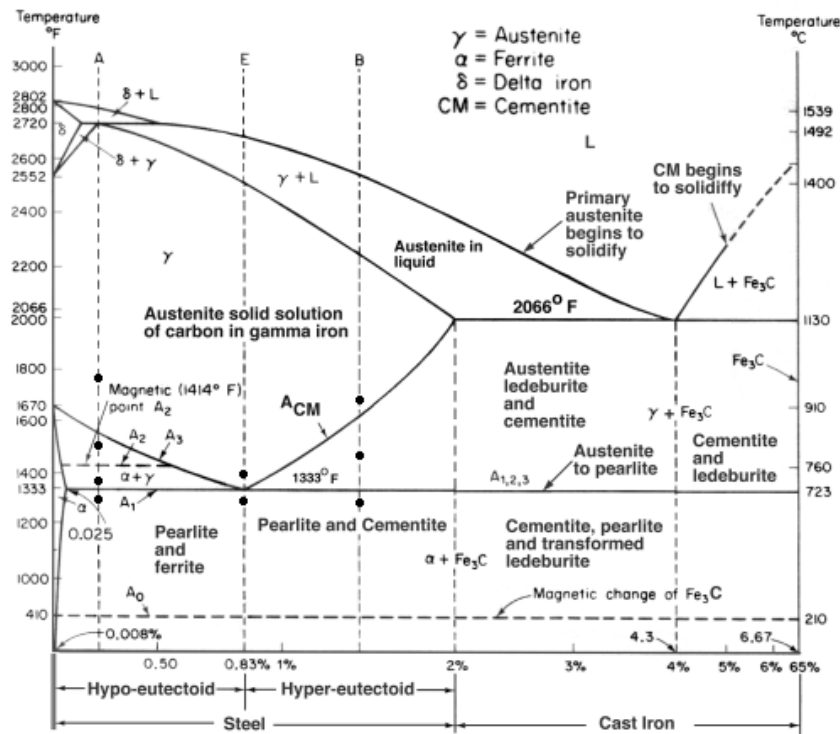
Figure 2: Fe-Fe₃C Phase Diagram, from: Materials Science and Metallurgy, 4th ed., Pollack, Prentice-Hall, 1988

To describe structural materials of current reactor fleet, four most common steels were selected and briefly characterized in following paragraphs. As it was mentioned in the introduction, PWRs represent roughly two thirds of all units, which means their structural materials can be considered the most common. Pressurized water reactors can be divided in two groups – western PWRs and eastern VVERs. Both are different in many aspects. Construction materials are also slightly different regarding their chemical composition and in their fabrication routes, but they logically fulfill similar demands. Usual structural materials for primary circuit in case of PWRs are SS 304L, 308, 309 and 316L. The letter "L" stands for low carbon, which means the amount of C is limited to 0.03% on the contrary to the classic SS 304 and SS 316 that contain 0.08% of C. Carbon content had to be reduced due to the carbide precipitation in the weld area, which led to the embrittlement of the material. The first one, SS 304L, is a very common construction material used for fabrication of reactor vessel internals (RVI), some parts of primary piping and then also very often in secondary circuit on components like preheaters, steam driers and so on. SSs 308 and 309 are thanks to their good weldability used as inner cladding materials together with SS 316L, which is the most corrosion resistant material from the entire 300 series due to addition of molybdenum. Chemical composition of SS 304 and SS 316 is described in tables 1 and 2, respectively. (3) (4)

SS 304L								
Element	Ni	Cr	Mo	Fe	Si	Mn	C	P	S
wt %	9.25	19	0	Balance	1	2	max 0.03	max 0.045	max 0.03

Table 1: Chemical composition of SS 304, from: http://www.espimetal.com/index.php/technical-data/

SS 316L								
Element	Ni	Cr	Mo	Fe	Si	Mn	C	P	S
wt %	12	17	2.5	Balance	1	2	max 0.03	max 0.045	max 0.03

Table 2: Chemical composition of SS 316, from: http://www.espimetal.com/index.php/technical-data/

On the other hand, reactor pressure vessel (RPV) of VVER (specifically the VVER 1000/V-320) is made of SS 15Ch2(N)MFA and its variants, while the RPV inner cladding is from austenitic SS 04Ch20N10G2B. RVI are mostly made of SS 08Ch18N10T, that is also austenitic SS stabilized with titanium. For the belt region around the reactor core is used a steel labelled as 15Ch2NMFA-A, which is a material less susceptible to the irradiation damage. This susceptibility is mostly affected by the amount of impurities and restricted elements in the material, such as phosphor, sulphur, copper and cobalt etc. Chemical composition of both main stainless steels is described in following tables. (how to cite a lecture?) (5) (6)

15Ch2NMFA								
Element	Ni	Cr	Ti	Fe	Si	Mn	C	P	S
wt %	1.1	2.1	0.6	Balance	0.23	0.5	0.15	0.02	0.02

Table 3: Chemical composition of 15Ch2NMFA, from: http://konsys2.tanger.cz/files/proceedings/21/papers/3732.pdf

08Ch18N10T								
Element	Ni	Cr	Ti	Fe	Si	Mn	C	P	S
wt %	10	18	0.5	Balance	0.8	1.5	0.08	0.035	0.02

Table 4: Chemical composition of 08Ch18N10T, from: http://konsys2.tanger.cz/files/proceedings/21/papers/413

1.2. Material Development for Gen IV and Fusion

The development of materials for Generation IV (Gen IV) and fusion is intertwined due to similar environments of fast reactor in-core component and first wall of fusion reactor. At the beginning of Gen IV development, standard structural steels for PWRs were considered as possible construction material. For example, the SS 316 was tested for application in liquid metal-cooled reactors. However, experiments revealed the alloy is susceptible to swelling, which causes the dimensional instability of structures and components. Swelling was partially

mitigated by cold working, but not to a sufficient level. World wide coordinated material research for Gen IV and fusion begun in 1970s. Materials developed for these applications mainly need to keep desired mechanical properties at elevated temperatures, withstand bombardment of high energy neutrons around 14 MeV causing up to 200 dpa and minimize the activation regarding eventual decommissioning process (decrease of irradiation rate [Sv/h] and decay heat [W/kg]). Attention was initially given to nickel-based superalloys, molybdenum or niobium -based alloys, titanium-stabilized austenitic steels etc. Out of this group of candidate alloys FM steels came out as a preferred material. The target for the researchers was not only to reduce swelling, but also the irradiation hardening and to increase creep resistance. FM steels afterwards replaced austenitic steels as a construction material of fast breeder reactors. Structural components of breeder reactors are exposed to fast neutron flux density of approx. 10^{15} n/cm^{2}s while in PWRs the thermal neutron flux density is roughly 10^{13} n/cm^{2}s. (7)

Originally, FM steels containing Cr and Mo were considered as suitable structural materials for liquid metal-cooled fast breeder reactors as well as for the first wall and tritium breeding blanket of fusion reactor. Two main alloys were picked, the first one containing 12% Cr, 1% Mo, 0.2% C and additions of W and V got a name HT-9, while the second one with 9% Cr, 1% Mo, 0.1% C, 0.25% V, 0.1% Nb and 0.05% N was called T91. Both alloys, that were developed in the United States, have very good high-temperature mechanical properties, but HT-9 showed better corrosion and swelling resistance. On the other hand, the T91 is less susceptible to irradiation embrittlement. The HT-9 steel was used straightaway for fuel cladding and in-core ducts of US experimental reactor Fast Flux Test Facility. In-core structurals of two US reactor designs - Power Reactor Inherently Safe Module and Sodium Advanced Fast Reactor, were also supposed to be made of HT-9. (7)

Further development of fast reactor and fusion materials around the world started to be focused on low activation steels. Concentrations of impurities like S and P, alloying elements such as Ni, Mo, Nb and other elements (Co, Bi, Cd, Ag, etc.) had to be restricted, if the future activation of the material should be minimized. In some cases, materials had to be isotopically tailored in order to reduce the concentration of unwanted isotopes, but to keep the qualities of the alloying element in general. Isotopic tailoring was applied for example on HT-9 where the amount of ^{92}Mo had to be reduced. Because the reduction of only certain isotopes is much more expensive than a replacement of the entire alloying element, researchers started to look for suitable substitutions. W and V were found as convenient replacement for Mo, while the Ta seemed to

be the substitute for Nb. To be able to get a martensitic structure, suitable austenite stabilization elements like Mn and C also had to be involved. These changes in chemical composition led to an introduction of so called reduced activation FM (RAFM) steels that should have approximately two times smaller final activation than preceding generation of steels. This is especially important when dealing with decommissioning and consequent storage of activated waste. RAFM should meet criteria for shallow land waste disposal approximately 100 years after the plant shut-down. The most favorable chemical composition was shown by 9Cr steels with W amount up to 2%. These alloys kept very good mechanical properties and remained microstructurally stable at high temperatures with relatively low susceptibility to most effects of irradiation. The biggest issue was void swelling induced by helium generation within the material. However, the investigation of this effect requires high energy neutron sources, that are not a common equipment till now. Out of all candidate materials, steel labelled as 9CrWVTa had one of the best results and was subsequently given a name EUROFER 97. As the name itself suggests, the material was developed in Europe thanks to European Fusion Development Agreement – Structural Materials. EUROFER 97 is officially an European reference material for a DEMO (demonstration power station) intended to be built upon the ITER experimental fusion reactor. Table 5 shows the chemical composition of EUROFER 97. (7) (8)

EUROFER 97											
Element	Ni	Cr	Mo	Ta	V	W	Fe	Si	Mn	C	P	S
wt %	0.02	9	0.05	0.12	0.2	1.1	Balance	0.05	0.6	0.11	0.005	0.005

Table 5: Chemical composition of EUROFER 97, from:
http://www.iaea.org/inis/collection/NCLCollectionStore/_Public/36/026/36026402.pdf

According to the IAEA, there are currently two main RAFM steels with large database of material properties and proved capability of forming plates and tubes of required dimensions. Apart from the EUROFER 97 it is the Japanese F82H. (9)

Although the mechanical properties of a fresh material are promising, the effect of thermal aging causes microstructural changes that certainly result in their aggravation. At elevated temperatures microstructural changes like creation of precipitates and element segregation are induced. Such changes affect material properties as tensile strength, fracture toughness and low cycle fatigue. Therefore, the material degradation under high temperatures and irradiation must be further investigated. (8)

RAFM steels with 9% of Cr generally show better corrosion resistance in steam generator environment than low-alloy steels and have comparable results with austenitic steels. Assuming the super critical pressurized water conditions (23.5 MPa, 550°C) the corrosion rate is estimated to 40 μm/yr. Considering the He cooled Pb-Li breeding blanket of e.g. a DEMO fusion reactor, RAFM steels show a corrosion rate of 700 μm/yr. (9)

Welding will have the same importance for Gen IV and fusion as it has now at present reactor technologies. Good weldability is therefore a key quality of each candidate material. Welded joints will have to be tight enough to prevent helium from leaking. They will also need to withstand severe neutron fluence causing embrittlement of the welded material. Thanks to the martensitic transformation the weld metal region becomes very hard and brittle. The metal in the heat-affected zone will become over-tempered and because the A_1 temperature (showed in fig. 1) will be exceeded in the bond region, the metal there will undergo an austenitic transformation. Such austenitic transformation will cause varying grain structure and size reaching from the heat-affected zone to the bond region. Therefore, we obtain hard and brittle material in the middle of the weld, but on the other hand also relatively soft weld peripheries. As a result, the joint requires a post-welding heat treatment, so it regains mechanical desired properties of the base metal. RAFM steels are weldable by electron beam as well as in tungsten inert gas. The electron beam method provides satisfying results, although the procedure has to be strictly obeyed. The advantage of welding in tungsten inert atmosphere is a lower embrittlement of the weld metal. (9)

Mechanical properties of RAFM steels must be at least comparable with mechanical properties of conventional nuclear grade construction steels. Direct comparison is shown in the table 6.

	EUROFER 97	SS 316	SS 304	15Ch2NMFA	08Ch18N10T
Rm [MPa]	671	480 – 686	481 – 672	608	500 - 750
Rp_{min}[MPa]	568	186	181	490	205
E [GPa]	213	203	199	208	200

Table 6:Comparison of mechanical properties
EUROFER 97 data from: Reith, M. et. al.; EUROFER 97 – Tensile, Charpy and Structural Tests

SS 316 data from: ČSN 41 7346; SS 304 data from: ČSN 41 7240; 08Ch18N10T data from: ČSN 41 7247

15Ch2NMFA data from: Mahmoud, H., Vlasic, F. and Mazal, P. Simulation of Operational Loading of Pressure Equipment by Means of Non-destructive Testing

Material properties are generally affected by chemical composition, structure and fabrication procedures. Concerning the chemical composition, desired qualities are achieved by adding specific alloying elements in well-defined amounts. However, the impurities will always be present, as well as drawbacks associated with them. There are two main approaches to enhance material properties. The first one is based on reduction of impurities to the minimum, ideally to zero. This attitude appears to be efficient when speaking about reduction by several percent, nevertheless, once the concentration of specific impurity approaches zero, it becomes much more difficult and expensive to lower its amount. That is why a lot of efforts is now given into the second approach based on implementation of inclusions that would increase mechanical properties to the level acceptable in Gen IV and fusion reactor applications. Oxide dispersion strengthened (ODS) steels are the typical example of such approach. This group of materials is especially resistant to the irradiation damage and high-temperature creep thanks to the number of precipitates placed in their structure. (10)

The EUROFER 97 also has an ODS modification. This material has almost identical chemical composition as a classic EUROFER with the exception of homogenously dispersed nanoparticles. These particles minimize the irradiation effects and enhance the thermal stability of the steel. Moreover, the maximum operating temperature was increased from 550°C of a standard EUROFER to 650°C in case of the ODS variant. For the application involving a fluence of high energy neutrons particles of Y_2O_3 were found as most suitable. These so called nanoclusters are preventing the movement of dislocations and therefore increase the mechanical properties and creep resistance of ODS steels in general. The ODS EUROFER is fabricated from a steel powder, that was atomized in inert gas. Particles of Y_2O_3 (approximately 0.3 wt. %) are added mechanically also in the inert atmosphere. The mixture is then consolidated by a hot isostatic pressure method at 1150°C and 100 MPa for two hours. This fabrication procedure creates a carbide film along grain boundaries. This unwanted side effect is being mitigated by subsequent thermo-mechanical treatment. (10)

1.3.   Operational Conditions of Reactor Materials

Going from LWRs towards technologies with better efficiency means mainly increasing of operating temperatures. Nuclear power generation is now running mostly on light water moderated and cooled reactors, majority of them are PWRs. Typical operating conditions in

the primary circuit of a 1000 MWe PWR are T ≈ 320°C, p ≈ 15 MPa. This operating pressure is quite high compared to most of the other reactors, apart from those designs using supercritical water. Nevertheless, the general trend today is to decrease primary circuit pressure in order to use thinner walls and save the material. On the contrary, the operating temperatures are being increased not only to achieve better efficiency, but also to be able to utilize the NPP for other purposes, such as hydrogen production, process heat, water desalination and so on. For example, HTGRs operate mainly in around 4 MPa, which reduces the demands on material toughness compared to the PWRs, but the operating temperatures are reaching up to 1000°C. This suggests that new materials will have to be more temperature resistant and heat stable, than the present ones.

We also need to consider an increased corrosivity, because many of proposed coolants for future reactor technologies (e.g. molten salts and super critical water) are more corrosion aggressive than conventional PWR coolant (demineralized water with diluted boric acid). Corrosion represents a big issue especially when speaking about Gen IV reactors. It is impossible to create a material, that would be resistant to all types of corrosion, but global efforts are made to increase resistivity to certain NPP specific types of corrosion, as described further in this work.

Another problem represents a neutron fluence. LWRs work with neutrons in thermal spectrum, that interact with structural materials differently than neutrons in fast spectrum. Furthermore, the damage induced by fast neutrons is much more severe and occurs significantly faster than in case of neutrons with lower energies. Irradiation induced damage together with creep are currently subjected to most intensive studies within material development for Gen IV and fusion.

1.4.   Material Degradation

Materials used for nuclear power reactor applications need to withstand many severe conditions, that will eventually lead to an aggravation of their properties. Lifetime of materials used for fabrication of reactor pressure vessel (RPV), reactor vessel internals (RVI), primary piping and so on is a key factor determining the life time of the NPP. Regarding the total investment necessary to build a new NPP, it is more than desirable to operate the facility as long, as possible. This is not just a case of NPPs built in future. Considering the present situation, when almost two thirds of running units approach the end of their designed life time,

the decision whether to decommission the NPP or keep it in operation might have not only economical, but also a strategic importance. Example of such situation might be seen in Armenia. If the residual life time of the power plant is to be assessed, the knowledge of material behaviour and degradation is essential. Degradation mechanisms relevant for the nuclear power devices in general will be briefly introduced in following paragraphs.

Aging degradation affects the entire NPP including mechanical and electrical equipment and also civil structures. The form of degradation depends on material and environmental conditions that need to be fully understood and managed. Degradation mechanisms are fundamental processes of aging degradation and are often referred to as aging mechanisms. Aging effects are then the results of such mechanisms that can be observed, measured or detected on structures and components (SCs). It is also important to realize, that it is usually a combination of aging mechanisms that affects the material simultaneously.

1.4.1. Cavitation

Cavitation occurs as result of pressure fluctuations in flowing coolant. The damage is caused by growth and collapse of vapor bubbles and can be observed on pumps impellers, valves seats, letdown orifices, nozzle edges, reactor internals and many other SCs. Occurrence of this degradation mechanism depends on inlet and outlet pressure, coolant temperature and flow rate. Heat removal in case of Gen IV and fusion requires high flow rates that are associated with high velocities of flowing coolant. Such conditions might create severe cavitation damage (11)

Noise, vibration and erosion that might result in a damage or failure of SC are possible effects of cavitation. However, precautions concerning this degradation mechanism should be made during the design phase and respected while setting the operational parameters that should be subsequently maintained with regards to the plant efficiency and safety. (12)

1.4.2. Corrosion

Corrosion represents the greatest menace for primary and secondary systems. Because it is a complex process depending on various aspects (environment, material condition and composition, etc.), it can occur in many forms that usually act simultaneously. Loss of material from the component due to corrosion leads to release of corrosion products into the coolant and might subsequently lead to fouling or sludge creation, if not filtered or skimmed. Besides that,

released corrosion products can be subsequently activated and cause further contamination. The main alloying elements used to mitigate corrosion of steels are Cr, Ni and Mo. Corrosion is divided in two major groups on general and localized corrosion. (13)

General corrosion occurs in a homogenous manner. From the PWR experience materials most often encounter following types of general corrosion mechanisms: (14)

a) <u>Boric Acid Corrosion</u>: This PWR specific form of corrosion is especially dangerous in combination with elevated temperatures and access of air. Low-alloy and carbon steels are very vulnerable.

b) <u>Flow Accelerated Corrosion</u>: Wall thinning due to this corrosion mechanism in carbon steel piping is not only because of the mechanical effect. The protective magnetite film that is normally formed on the internal pipe surface is diluted, so the corrosion progresses further into material.

c) <u>Erosion-Corrosion</u>: This corrosion mechanism is similar to the previous one, with the difference that the protective magnetite film is not diluted, but mechanically removed from the surface. Both corrosion types require low-alloy steels, two phase flow of high velocity and change in the geometry of the pipe.

Localized corrosion mechanisms affect smaller areas but with much higher rate than general corrosion. Again from PWR experience, the most significant types localized corrosion: (14)

a) <u>Crevice Corrosion</u>: Very low coolant flow in the crevice allows a development of corrosive environment. Joints, connections, contact surfaces and crevices between gaskets or bolt heads are susceptible to such degradation, especially when the metal materials are not similar. Vulnerable materials are carbon steel, cast iron, low alloy steels, stainless steel, copper, and nickel base alloys. Crevice corrosion may also occur after cladding/lining degradation.

b) <u>Galvanic Corrosion</u>: This type of corrosion is accelerated due to electrochemical process when a less noble metal degrades preferentially to a more noble metal in a corrosive electrolyte.

c) <u>Pitting Corrosion</u>: This corrosion is limited to a point or small area, which takes the form of cavities called pits. Components made of borated steel and exposed to steam environments are vulnerable.

1.4.3. Fatigue

This degradation is caused by fluctuating stresses with smaller value than the tensile stress of the material. It results in progressive fractures that consequently grow as the stresses continue to fluctuate. Fluctuating stresses can come from cyclic mechanical loading, vibrations and also from cyclic thermal loading. The crack is being initiated on microscopic level after a sufficient amount of microstructural damage is accumulated in the most vulnerable sections of SCs. Mechanical fatigue mostly affects rotating equipment, supports and piping attached to large components. Vibrations are one of the most frequent fatigue causes. They may originate from the outside of SC, but they are often induced by the internal flow. Special attention during the design and operation need to be given to resonance frequencies, which can significantly speed up the occurrence of SC failure. (14)

SCs subjected to thermal loading or thermal cycling are susceptible to thermal fatigue. In general, the higher the temperature fluctuations are, the greater thermal stresses are reached and the greater decrease of fatigue strength is achieved. Thermal fatigue involves two important terms – thermal stratification and turbulent penetration, which induce temperature fluctuations. Thermal stratification means a separation of hotter and colder fluid due to density difference. This phenomenon happens more markedly when fluids are mixed slowly and creates a temperature gradient in the radial section of pipe or vessel. The material is therefore subjected to greater thermal stresses. Phenomenon of turbulent penetration occurs mostly in T-junctions when the flow velocity of main line is greater than flow velocity in the branch. Bits of the turbulent main flow may then enter the branch causing additional thermal cycling. The most vulnerable part of NPP to both mentioned phenomena is probably the pressurizer surge line. (15)

1.4.4. Irradiation / Neutron Fluence

Two major sub-mechanisms of this aging mechanism are material embrittlement and void swelling. While the first one influences mostly the RPV base material and welds, void swelling occurs on components of reactor internals such as baffle bolts. (13)

1.4.4.1.   Irradiation Embrittlement

This time dependent degradation results in embrittlement of carbon and low-alloy steels. It may produce changes in mechanical properties by increasing tensile and yield strengths with a corresponding decrease in fracture toughness and ductility. The extent of embrittlement

depends on neutron fluence, temperature, and trace material chemistry (nickel alloying additions, trace impurities of copper and phosphor increase embrittlement). Irradiation embrittlement is usually characterized by the increase in a ductile-to-brittle transient temperature (DBTT) that marks the transition between low toughness brittle and high toughness ductile fracture regimes. (14) (16)

It is probably the most life-limiting aging mechanism, which can decide about life extension feasibility. It was especially life-limiting for older types of reactors such as VVER 440/V-230 due to relatively high exposure of belt line region including the welds. Surveillance specimen programme is then a key activity for monitoring of material behaviour under this aging mechanism. The problem is a limited amount of specimen material, that can be fitted into the RPV. It rises a demand for mechanical testing requiring small amounts of material like nanoindentation. (14) (17)

High-energy neutrons are the dominant source of embrittlement, which is also why the research carried out on fast reactors is very helpful also for reactors using thermal neutrons. Neutrons with high energy knock atoms off the original atomic structure of the metal causing changes not only in the structure, but also in the chemical composition by the activation. Fusion neutrons with energy of 14 MeV cause severe displacement per atom (dpa) damage as well as He and H production from the decay of Fe and Cr atoms. The dpa stands for an average number of displacements each atom in the structure has encountered. Fast neutrons cause so called primary knock-on of the atom from its position. This leads to a chain reaction and production of cascade damage in the atomic structure. The H and He production from Fe and Cr is due to significantly higher cross-section of both elements for neutron energies in order of MeV, as shown in figures 3, 4, 5 and 6. Induced changes create defect clusters that are blocking the motion of dislocations under applied stress. The material then looses its ductility and becomes more brittle. (9) (18)
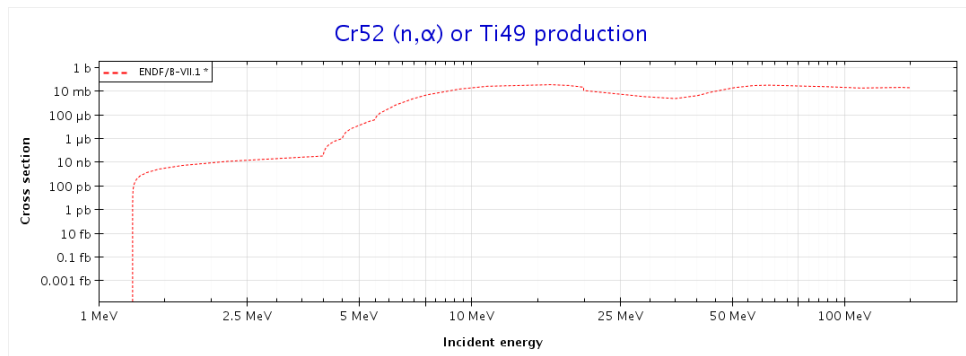
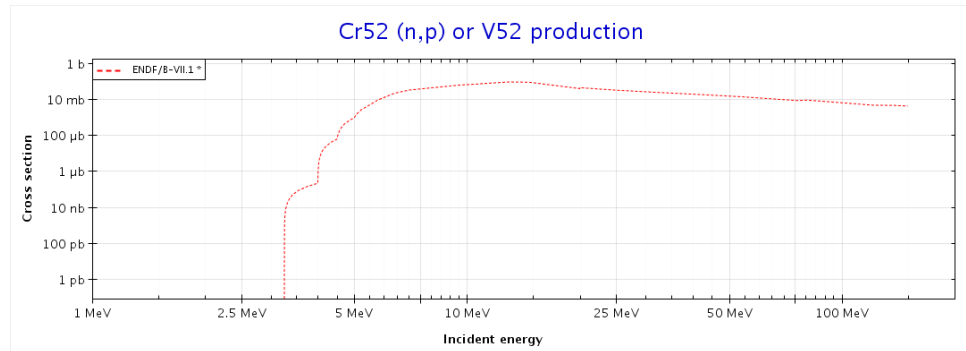Figure 3: Cr52 (n, α) reaction probability, from: http://www.oecd-nea.org/janisweb/book/neutrons/

Figure 4: Cr52 (n, p) reaction probability, from: http://www.oecd-nea.org/janisweb/book/neutrons/
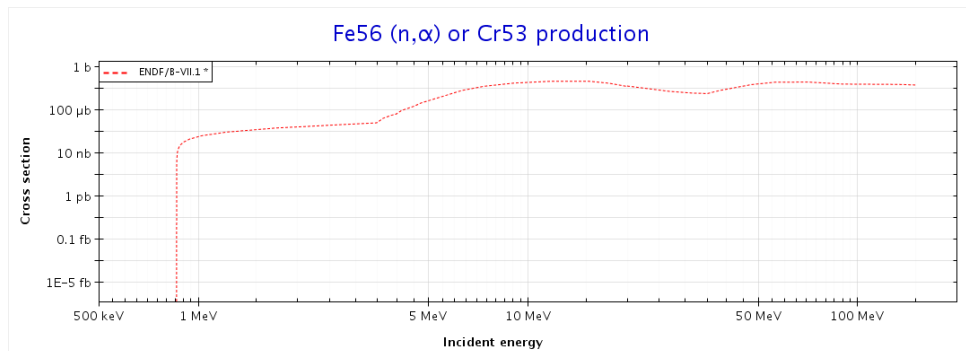
Figure 5: Fe56 (n, α) reaction probability, from: http://www.oecd-nea.org/janisweb/book/neutrons/
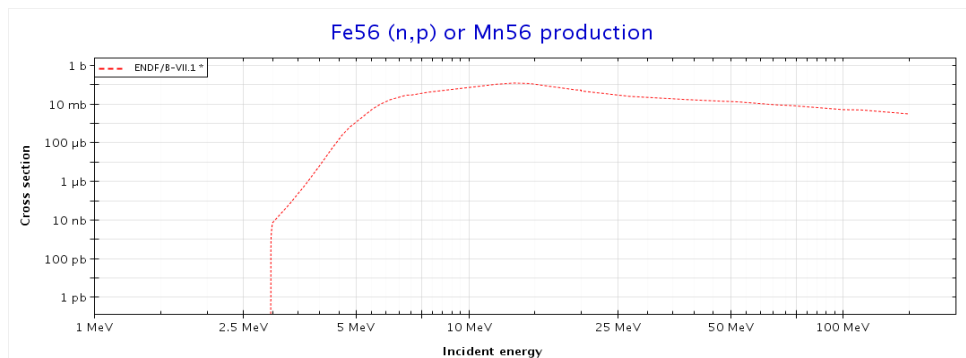
Figure 6: Fe56 (n, p) reaction probability, from:http://www.oecd-nea.org/janisweb/book/neutrons/

1.4.4.2.   Void swelling

This aging mechanism is based on neutron radiation that induces changes in material structure, dimensions and properties. Atoms of material are affected by impacting neutrons, which results

in creation of vacancies and dislocations that subsequently lead to the formation of voids. The effect of this process is then the increase of volume at the expense of density. (13) (14)

As it was mentioned above, He and H are produced from the interaction of high energy neutrons with atoms of Fe and Cr. These gasses then fill the voids created in the material and so they contribute to swelling as well. The effects of void swelling may be aggravated in case of synergy with other degradation mechanisms such as creep. Motion of vacancies can accelerate the creep rate and contribute to faster stress relaxation and deformation. Apart from creep, the void swelling can also significantly contribute to irradiation assisted stress corrosion cracking and irradiation embrittlement. (13) (19)

While swelling is typically a greater concern for fast reactor applications, where it can be very life-limiting, voids have recently been observed in LWR components too. Void swelling may moreover occur after an extended incubation period, which worsens the ability of material behaviour prediction. Especially in +60years scenarios, this could be an issue for near-core reactor internals made of austenitic stainless steel. (14) (20)
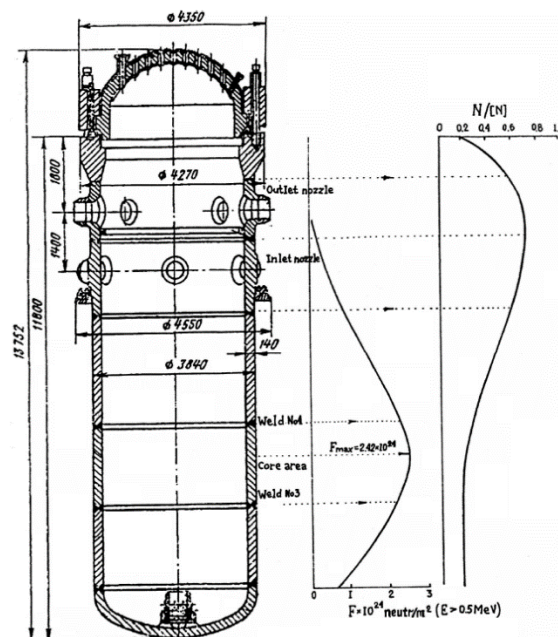
Figure 7: Neutron fluence and fatigue damage distribution through RPV of VVER-440 – source: Karzov, G.; Timofeev, B. Main Mechanisms of Material Properties Degradation Under Reactor Pressure Vessel Operating Conditions, 1999

1.4.5. Selective Leaching

As it is obvious from the name of this degradation mechanism, it targets on preferential alloying elements such as Sn, Ni, Al, Si, Cd and Be that are being removed from the material. It results

in a consequent enrichment of remaining alloying elements and change in material properties and behaviour. That is why selective leaching is often called "de-alloying". In general, this mechanism is based on selective corrosion. Conditions that lead to selective leaching are high temperatures, stagnant flow and corrosive environment. Susceptible materials are copper alloys and grey cast iron that are facing dezincification (leaching of zinc from brass) and graphitization (leaching of iron from cast iron) respectively. (14)

1.4.6. Stress Corrosion Cracking

Environmentally assisted cracking (EAC), which is a generic term for stress corrosion cracking (SCC), is a form of degradation that combines influences of corrosion and stress. In such environment the SCC enables crack initiation and sub-critical crack growth of susceptible materials. SCC can occur on internal surfaces usually in weld vicinity, but also on external surfaces, where it is often chloride related. There are two basic modes of SCC that may occur in the same alloy depending on the environment, microstructure and stress/strain state. The first one is intergranular SCC (IGSCC) and the second one is transgranular SCC (TGSCC). Both modes have a brittle-like appearance due to small or no macroscopic plastic deformation. IGSCC propagates the crack along grain boundaries, whereas TGSCC goes through the grains. Austenitic stainless steels and nickel based alloys, which have undergone sensitization or cold working, are vulnerable to IGSCC due to formation of chromium carbide precipitates at grain boundaries. On the other hand, the TGSCC occurs frequently in presence of chlorides and affects mostly SCs made of stainless steel. The most relevant types of SCC for PWR technology are: (13) (14) (21)

1. Primary water stress corrosion cracking
2. Irradiation-assisted stress corrosion cracking
3. Low-temperature crack propagation

Figure 8: Scheme of SCC conditions – source: Stress Corrosion Cracking in Light Water Reactors :Good Practices and Lessons Learned, 2011, pg. 4

1.4.7. Thermal Aging

This aging mechanism can be also called thermal embrittlement and is dependent on time and temperature. As all embrittlement degradations it results in decrease of material toughness. Thermal aging involves two types of mechanisms – temper embrittlement and strain aging embrittlement. Temper embrittlement consists in segregation of impurity elements such as antimony, sulphur and phosphor to grain boundaries that were originally austenitic. It generally occurs at higher temperatures during slow heat up or cooldown. Strain aging embrittlement is a mechanism that disables the slip of dislocations. This is achieved when smaller atoms of alloying elements like carbon, nitrogen or hydrogen substitutes for iron in the material structure. Both phenomena affect ferritic and low-alloy steels, but not the wrought stainless steel. (14)

1.4.8. Wear

Wear is defined as removal of material surface layers due to relative motion in between two parts or abrasive particles. It may occur because of insufficient lubrication or loss of clamping force that allows not intended relative motion. Mechanical wear and fretting affects mostly rotating equipment and RVIs due to flow induced vibrations, while binding occurs at components within pumps and valves. The effects of normal wear mechanisms are amplified by an environment typical for NPP – elevated pressures and temperatures in addition with corrosive conditions. (14)

1.5.   Methods of material properties evaluation

Following paragraphs are describing methods that are commonly used to evaluate material properties for research or monitoring purposes. Because this work focuses on evaluation of material properties through indentation testing, the description of other methods will be brief.

1.5.1. Tensile testing

This is one of the basic standardized methods how to determine material properties (tensile stress, shear stress, etc.). A controlled load is applied on the specimen until the failure occurs, while the specimen elongation is continuously measured. The specimen must be well aligned in order to prevent creation of bending moment.

Because the dimensions of the specimen are known as well as the force applied on it, the stress can be easily calculated as the force divided by the cross-sectional area. For the calculation of strain is enough to divide the specimen elongation, which is a measured value, by the original length of the standardized specimen. Strain gauges are often used when the Poisson´s ratio is being measured. The dimensions of a standard tensile test specimen are shown in the figure 9.
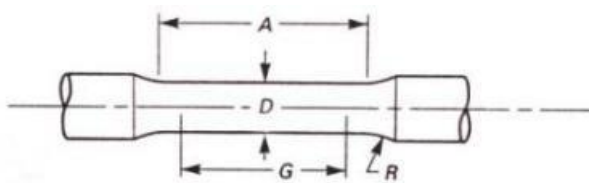
Figure 9:Tensile test specimen, from: www.practicalmaintenance.net/?p=948

- G = 50 mm

- A = 60 mm

- D = 12,5 mm

- R = 10 mm

- + material used for fixture

To obtain reliable results a series several measurements must be conducted. Each measurement means one destructed specimen. If an average steel density of 8 000 kg/m^3 and a specimen volume of 1.98 x 10^{-5} m^3 are considered, the resulting weight of produced waste in case of 10 conducted tests will be 1.59 kg. Such amount of the waste represents significant expenses in case of active material that needs to be consequently stored. Such specimens would be to large for a surveillance specimen program, therefore specimens of reduced dimensions (Ø 4 x 22 mm) are usually used in this case.

1.5.2. Charpy V-notch test

This is again a standardized testing method designed to evaluate the amount of energy dissipated in the material during its crack. It is used to determine the temperature dependence

of ductile-to-brittle fracture. This method is frequently used in the industry thanks to relatively simple preparation of specimens.

The main part of the measuring apparatus is a pendulum with known weight and height from which it is going to swing. This pendulum impacts a notched specimen that consequently fractures and the height reached by the pendulum after the impact is recorded. This is enough to determine the energy absorbed in the specimen material. Testing is usually conducted under various temperatures to be able to determine at which temperature the fracture changes from ductile to brittle.
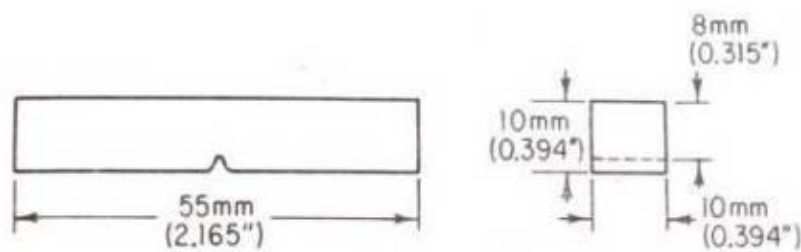
Figure 10: Charpy V-notch test specimen, from: www.practicalmaintenance.net/?p=968

Because such specimens are quite large to be placed inside the surveillance program boxes in sufficient number, only the central section (14 mm long) is usually inserted. Both ends are then welded by electron beam, so the final length of the specimen is 55 mm, as mentioned above. If 10 tests are conducted, the resulting amount of waste will be 0,44 kg, assuming the same metal density of 8 000 kg/m^3.

1.5.3. Measurements of hardness

Hardness is associated with material's strength and its ability to resist plastic deformation such as penetration, scratching and wear in general. Moreover, the value of hardness is also changing under the influence of several other degradation mechanisms and therefore it can reveal a lot about residual lifetime of the material. Phase transformations, that might be induced within the material, can also be evaluated by hardness measurement. (22) (23)

1.5.3.1.   *Standard methods*

Methods for material hardness testing were developed in the second half of 19th century. They became commercially available and popular very quickly at the beginning of 20th century together with other standard techniques like Charpy V-notch test and tensile test. The reason was probably the launch of mass production in automotive, tools production and so on, where

all the products require fast and reliable quality testing. Moreover, preceding methods of testing the wear resistance ("file" & scratch tests) were also not considered as sufficiently accurate. (24)

Not all types of hardness testing are based on indentation principle like Rockwell, Brinell and Vickers, although these quasi-static tests are the most common. Then there is a group of dynamic measurements involving the scleroscope tests, when a rebound of small metallic hammer with a diamond tip or a steel ball is measured, while in another method called "file test" it is assessed how well is the file cutting the specimen material. Even though there are many ways to determine the hardness, there is no exact recalculation procedure that would enable to convert results of one method to another. (22)

During both, quasi-static and dynamic tests, a certain level of work hardening might be encountered, which consequently affects the hardness results. In case of the quasi-static measurement the work hardening is caused by increase of the load and by an increase of the indentation area. Work hardening is also observed at the scleroscope measurement which has been done repeatedly on the same spot. Concerning quasi-static tests, there was another issue of measuring initially also the elastic response of the material. That was solved by Rockwell in 1919, when he came up with a method of applying small load at the beginning, then adding much higher load and subsequently removing the initial small load, so the elastic hardness influence is eliminated. (24)

Concerning indentation based methods, it is usually the applied load and indentation depth or indent area that are measured and after used for hardness calculation. Because of that a geometry of the tip plays a key role in indentation experiments and it is not only a question of choosing the correct tip – material combination, but also a wear of the tip needs to be monitored and regarded. Tips can have various shapes from cones and pyramids to spherical or flat contact surfaces. They are made of the hardest materials like diamond and cubic boron nitride, but also from tungsten-carbide or steel depending on the specimen. The tip selection affects possible load interval as well.

Hardness measurements in comparison with other methods do not require a difficult sample preparation and it is generally considered as non-destructive, which makes it much cheaper and sometimes also more convenient than the other methods like tensile test. Furthermore, basic setups can be easily modified so it is possible to perform tests at various conditions

corresponding with material operating conditions. Standard hardness testing methods, regardless the tip that is being used, are working on the similar principle as more advanced techniques that are measuring in much smaller scales and therefore it is necessary to mention them too. The main kinds of indentation tips are:

1) Brinell:
   - Sphere with Ø = 10 mm
   - Ø of the indent is measured through microscope (source of errors)
   - Possible to apply high loads (30 kN)
   - Requires a specimen 10x thicker than the indent depth
     (not for thin layers of hard materials)
   - Specimen surface can be rough
   - Can be used on heterogenous materials

2) Rockwell:
   - Cone with tip angle of 120°
   - Hardness is obtained directly from the machine that measures indentation depth
     (less error, quick and cost effective)
   - The wear of the tip and material composition have significant effect
     (at least 3 measurements needed)
   - Simple preparation of the specimen required

3) Vickers:
   - Four-sided pyramid with tip angle of 136°
   - Requires ground and polished specimen
   - Indent evaluated optically
     (lower precision, more time needed)
   - Can be used on any material

4) Knoop:
   - Asymmetric four-sided pyramid
   - Requires polished specimen
   - Indent measured optically
   - Suitable for smaller specimens and brittle materials

Decrease of hardness reveals a lot about temperature resistance of tested material. Softening of iron-based alloys depends mostly on their crystallographic structure. For example, austenitic steels show more significant softening rates than other steels within the range from RT to 400°C. The creep was generally observed to be a dominant mechanism causing steep drop of the hardness at temperatures higher than 0.4 times the melting temperature (T_m). Such temperatures are easily reached during the operation of many present technologies, especially in power engineering, which has a huge effect on material strength, wear resistance and overall safety of the operation. Chemical composition of the steel also plays a significant role, when e.g. Mo and B are capable to decrease the softening rate, while V and W contribute to the RT hardness by forming carbides. Material processing, treatment and mechanical history affect the structure too, so it needs to be regarded as well. Due to all those reasons the material behaviour at elevated temperatures cannot be predicted simply based on the knowledge obtained at room temperature, which is the main motivation that drives the demand for high-temperature (HT) testing. (23)

1.5.3.2. *Micro scale hardness testing*

Boom of these methods is often associated with the development of Micro-Electro-Mechanical Systems (MEMS). Their invention was driven by the need to understand material behaviour for small-scale applications such as electronics, biomedicine and so on, where mechanical properties of thin foils, films and wires need to be verified. The hardness value is usually calculated from applied load and indent area, that can still be measured using optical microscope, which makes it easily applicable. (25)

The measurement system is composed of five subsystems:

- Specimen
- Fixturing/positioning system
- Actuating system
- Load cell
- Deformation measurement system
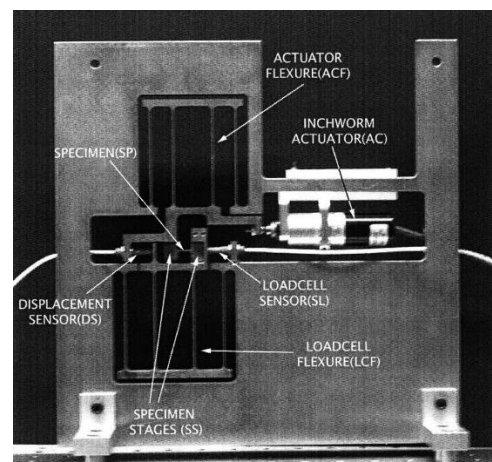
Figure 11: Example of micro-mechanical testing device, from: Gudlavalleti, S.; Mechanical Testing of Solid Materials at the Micro-Scale

Four-sided pyramid indenters like Vickers and Knoop encountered an accuracy problem when they were applied in micro scale. This problem originated during the indenter manufacturing where it was very difficult to fabricate the tip as pointy as required for precise measurement. Four-sided indenters therefore usually have a small edge instead of a sharp tip. Such issue was noticed by Berkovich, who has later introduced the three-sided pyramid indenter. Berkovich indenter was designed, so the area-to-depth function was similar to Vickers indenter. This fact means, that hardness values obtained by Berkovech indenter are comparable to those obtained by Vickers. (24)

1.6.   Nanoindentation

Speaking about measuring parameters in sub-micrometer scales, the undisputable advantage is the ability to analyze very specific areas of material like grains or even grain boundaries. It is also possible to focus on inclusions and thin coating or oxide layers, that are often affecting material behaviour. On the contrary, there are several distortions mostly associated with very high sensitivity of the appliances.

Although classic indentation technics for hardness measurements like Brinell and Rockwell have been developed since 1900s, the first so called Nanoindenter was introduced in the second half of 80s, in response to the boom of nano-scale technology that has occurred by that time. This technology was initially used in biomechanics, electronics etc., where thin layers of material required mechanical testing. In 1986 the nanoindentation was used for the first time by S. J. Zinkle and W. C. Oliver in order to evaluate the irradiation induced damage on specimens made of high-purity copper and AMZIRC alloy. Both specimens were irradiated by 14 MeV copper ions reaching the dose level of 40 dpa and thickness of irradiated layer 3.5 µm. Such small thickness of measured layer was the original reason to use the nanoindenter, because conventional microhardness testers were not able to measure it. (26) (27)

1.6.1. Pros & Cons

Motivations to carry out the nanoindentation are mostly associated with the fact, that a very small volume of material is required for comprehensive testing. Sample with smaller dimensions is also easier to handle and produces less waste, which plays significant role especially in case of activated materials. Because the nanoindentation testing is not as material consuming as conventional methods, it represents great advantage when speaking about life extension of nuclear power devices as well as research for Gen IV and fusion. The amount of

material within a surveillance specimen programme is very limited particularly in case of life extensions reaching up to 80 years of operation. Moreover, the nanoindentation is in most cases considered as non-destructive testing, so one sample can be examined multiple times. In addition, the preparation procedure of the sample, which will be closer described in experimental part, is composed of basic metallographic activities and requires no specific fabrication or modifications. Last, but not least, the nanoindentation apparatus is controlled via computer and the whole operation is relatively simple. (28)

On the contrary, samples intended for nanoindentaion must have an ideal surface. Sample roughness should be minimal, usually less than 30 nm. Dust particles or any debris settled on the sample can distort results if located between the sample surface and the indenter tip. Surface forces and adhesion cannot be neglected as well, if the applied load is in range of µN. If individual material phases are tested, the load must be applied adequately, so the volume of material influenced by the indenter tip is as localized as possible. The entire measurement is therefore very sensitive to external influences as vibrations or air circulation, which can cause significant thermal drift. Mainly during the high-temperature nanoindentation vibrations and drift induced by the flow of auxiliary gases might encountered. Temperature equilibrium between the specimen and indenter tip is important too. Any oxidation or temperature gradients can have severe impact on the precision. Quality of nanoindentation results can be generally enhanced if measurement conditions are conformed to the characteristics of both, indenter and sample material. (28)

1.6.2. Applications of nanoindentation

Nano-scale testing already has many applications in the development of coating layers and electronics. There is a wide variety of possible applications of nanoindentation. Thanks to relatively trivial sample preparation procedures, this method is suitable to many materials. Nanoindentation is especially convenient for testing of biological materials like bones and tissues, but it plays an important role in metallurgy and also in the development of composites. Apart from hardness and modulus measurements, this technique can be used to analyze creep relaxation, energy absorption, phase transformations, strain hardening and cracking. For example, due to very restricted volume of plastically affected material, the nanoindentation is ideal for the examination of welds. Nanoindentation at high temperatures represents a major challenge within material research for power engineering, as the structural changes induced by

high operating temperatures lead to degradation of material properties. Issues encountered while high-temperature nanoindentation will be addressed later in this work. (28)

1.6.3. Data acquisition and processing

Because it is barely possible to measure the nanoindent optically, another method of indent evaluation must be applied. During the nanoindentaion the applied load is recorded together with indentation depth, out of which the contact area between the specimen and the tip ca be determined, if the tip geometry and properties are known. It is possible say that the more accurate the measurement of indentation depth is, the more precise is the calculation of material hardness and Young's modulus. That obviates the need of optical measurement of the indent, which simplifies the evaluation process in some aspects. Indentation hardness and modulus need to be subsequently recalculated on bulk-equivalent properties via several computational models. Bulk equivalent hardness, or simply material hardness, later on serves as an input for calculations of Young´s modulus, yield stress and fracture toughness. Many models have been developed in order to obtain as true data as possible, out of which only those, that are being used most frequently, will be briefly described. (25) (29) (30)

1.6.3.1. Measurement modules

Nanoindentation measurements can be done in dynamic or quasi-static module. If we want to measure at a very specific point of the sample, so we can obtain only one indent, we can use continuous stiffness measurement (CSM). This dynamic module provides continuous hardness values from a single indent as a function of indentation depth. On the contrary, once we would like to analyze larger area, it is more convenient to define a matrix of indents, where each indent has a load value assigned from a certain range defined at the beginning of the measurement. Such quasi-static approach gives us multiple results which we can subsequently average or relate to the distance in between the indent and e.g. a grain boundary. (31)

CSM has been used since late 1980s. The principle is based on adding small but relatively fast oscillations into the main loading function, which allows us to obtain much more data from a single indentation than in case of quasi-static measurement. It enables to better determine values of hardness and Young's modulus through the cross-section of ion-irradiated or coated material. Despite its broad utilization, there is the issue of work hardening and fatigue damage, that could be induced by the load oscillations. This phenomenon was investigated and as it was revealed later, it occurs at frequencies much higher than those used during nanoindentation.

The amplitude was also reduced to the minimum value allowed by the measurement noise, as it was noticed that higher amplitudes distorted the results for materials with higher modulus to hardness ratio. (32)

1.6.3.2.   Computational methods

Calculations of material properties are done from measured values of load and displacement according to multiple computational models. These models are based on certain assumptions of material behaviour that have to be validated prior each experiment. If not, the results might be significantly distorted. Two main computational models are introduced in following paragraphs.

W. C. Oliver and G. M. Pharr have in 1992 introduced an improved technique to determine hardness and modulus from load-displacement curve recorded by the indentation sensing apparatus. Their approach was based on the method established before by Doerner and Nix, who assumed the initial third of unloading curve to be linear, so it seemed to be convenient to extrapolate it to the zero load and obtain an extrapolated depth. Extrapolated depth was leading to better results than peak load depth or final depth that were being used before, but, as Oliver and Pharr have found out, the initial part of unloading curve is hardly ever linear, so the extrapolated value also isn't that accurate. Therefore, they came up with a method, in which the initial curvature of unloading curve was regarded. (30) (28)

According to the Oliver-Pharr method, we can define the indenter tip geometry using the area function F(h). The value of this function at the contact depth (h_c) determines the projected contact area at the peak load (A_c), which can be expressed as

$$A_c = F(h_c) \qquad\qquad Eq.(1)$$

In case of ideally sharp Berkovich indenter the contact area function (further labelled as tip area function) is $A_c = 24.5 h_c^2$. In order to express non-ideal or mechanically worn tip, the function is further developed into the form of eq. 2:

$$A_c = 24.5 h_c^2 + C_1 h_c^1 + C_2 h_c^{1/2} + C_3 h_c^{1/4} + C_4 h_c^{1/8} + C_5 h_c^{1/16} \qquad Eq.(2)$$

The function itself needs to be established experimentally, while the contact depth results from subtraction of surface displacement depth (h_s) from peak load depth (h_{max}). The surface displacement depth at the contact perimeter is a crucial value which can be determined from

load-displacement data or from a tip specific equation using the final depth of residual hardness impression (h_f).

Figure 12: Oliver, W. C. a Pharr, G. M. An improved method for determining hardness and elastic modulus using load and displacement sensing indentation experiments; Fig. 19

The contact depth can be also calculated from an empiric relation with h_{max} shown in eq. 3:

$$h_c = \frac{\beta h_{max} - \varepsilon P_{max}}{S} \qquad \qquad Eq.(3)$$

where constants $\varepsilon = 0.75$ and $\beta = 1.05$ for a Berkovich indenter. Anyways, because the h_c cannot be measured directly, certain assumptions specific for each computational model must be made. For the Oliver-Pharr model there are three following assumptions:

1) The elastic recovery is only in vertical direction
2) There is no mutual influence between plastic and elastic deformation
3) Swelling effects and surface roughness can be neglected

Having all mentioned above, we can calculate the hardness (H) from the eq. 4:

$$H_{O-P} = \frac{P_{max}}{A_c} \qquad \qquad Eq.(4)$$

As we can see, the main issue is to determine the unloading stiffness of the material. This was originally done using the initial part of unloading curve. That part is significantly influenced by creep, which causes higher slope at the beginning of the curve and therefore it has negative effect on the results. In order to minimize the creep influence, we hold the load at the peak value for a certain period of time, so we reduce the time dependent plastic effect. Then it was observed, we can use a power law relation that describes the unloading data

$$P = C \cdot (h - h_f)^m \qquad\qquad Eq.(5)$$

where C, m and h_f are constants. Eq. 5 accurately depicts unloading curves for Berkovich indenter. Once we differentiate this equation and substitute the displacements and peak load, we get the slope of that initial part of unloading curve. This method was originally carried out on tungsten sample and proven that it has lower sensitivity to creep, which is why it became frequently used. (30)

Because the sample stiffness measurement is affected by the stiffness of the entire system (load frame), it is necessary to conduct so called machine/frame compliance test. This is basically a calibration procedure, during which we measure displacement induced in the load frame of the nanoindenter. The effect of load frame displacement is more significant for samples made of material with high Young's modulus and for larger indents in general. According to Oliver and Pharr, machine compliance test can also be used to determine the tip area function. This was originally done by direct imaging of a set of indents, which is very inconvenient in nano scale. Assuming the modulus to be independent of indentation depth and a known value of calibration specimen stiffness, we can start with the expression of total stiffness as a sum of specimen and load frame stiffness. Precise determination of system compliance is essential for subsequent calculations of reduced modulus. (30)

$$C = C_f + C_s \qquad\qquad Eq.(6)$$

Then we can assume an elastic contact between the specimen and the tip and express specimen compliance using the inverse of the contact stiffness $C_s = \frac{1}{S_s}$ as

$$C = C_f + \frac{\sqrt{\pi}}{2E_{eff}} \frac{1}{\sqrt{A_c}} \qquad\qquad Eq.(7)$$

from which we can easily express tip contact area as

$$A_c = \frac{\pi}{4} \frac{1}{E_{eff}^2} \frac{1}{(C - C_f)} \qquad\qquad Eq.(8)$$

From eq. 5 it is obvious, that incorrectly determined value of frame compliance affects the results through tip contact area. Frame compliance lower than actual value increases the contact area and therefore underestimates both results, hardness and modulus, while modulus shows

larger deviation. The trend of modulus values in relation to indentation depths can be also distorted by wrong frame compliance. (33)

E_{eff} stands for the reduced modulus, which involves non-rigid behaviour of the indenter and can be calculated according to eq. 9:

$$\frac{1}{E_{eff}} = \frac{(1 - v^2)}{E} + \frac{(1 - v_i^2)}{E_i} \qquad\qquad Eq.(9)$$

where v is a Poisson's ratio, E is the modulus and index i stands for the indenter. (30)

Another relation between the indentation hardness and depth was established in 1998 by Nix and Gao, as there was a need to take into account multiple effects that influence the measurement, such as indentation size effect. Their method was based on the Taylor's dislocation model and on a concept of geometrically necessary dislocations beneath the indenter tip.
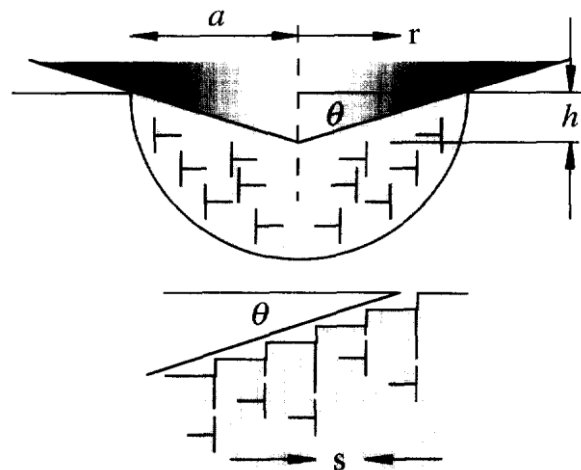
Figure 13: Nix, W. D. and Gao, H. Indentation Size Effects in Crystalline Materials: A Law for Strain Gradient Plasticity; Fig. 2

Basic inputs for this method are indentation depth and contact area function, which we use to determine at first the contact radius a and then a contact angle θ.

$$tan\theta = \frac{h}{a} = \frac{b}{s} \qquad\qquad Eq.(10)$$

where b stands for Burgers vector and s represents spacing between individual slip steps on sample surface. Then we express *s* from this equation and substitute it into the formula for total

length of injected loops, which has following form for a conical indenter (simplified Berkovich)

$$\lambda = \frac{\pi h a}{b} \qquad\qquad Eq.(11)$$

Together with a hemispherical volume underneath the indenter tip ($V = \frac{2}{3}\pi a^3$) we use λ to calculate the density of GNDs according to the formula

$$\rho_G = \frac{\lambda}{V} = \frac{3h}{2ba^2} \qquad\qquad Eq.(12)$$

Then we use the Taylor relation to find a shear strength.

$$\tau = \alpha \mu b \sqrt{\rho_G + \rho_S} \qquad\qquad Eq.(13)$$

This formula consists of an empirical constant α, shear modulus μ and a sum of ρ_G and a density of statistically stored dislocations ρ_S. Shear strength can be converted to the flow stress by applying von Misses rule and subsequently converted to hardness using value of 3 as a Tabor's factor.

$$\tau\sigma = \sqrt{3}\tau \quad \rightarrow \quad H = 3\sigma \qquad\qquad Eq.(14)$$

By substituting this relation into eqs. 12 and 13 we can obtain following formula that relates hardness with indentation depth

$$\left(\frac{H}{H_0}\right)^2 = 1 + \frac{h^*}{h} \qquad\qquad Eq.(15)$$

where H stands for material hardness at given indentation depth h, while H_0 is a hardness in a limit of infinite depth and h^* is a characteristic length dependent on indenter shape, material shear modulus and H_0. The h^* is basically the characteristic dimension of material microstructure. Unfortunately, this method correspondents better with micro-indentation behaviour than with the nanoindentation, so certain modifications had to be made. (34) (35)

There are two issues with the implementation of the original Nix-Gao method on nanoindentation. The first is that the model assumes an ideally sharp tip with no radius, that occurs on the indenter from fabrication or due to wear. Such tip then leads to smaller values of indentation hardness. Then there is the assumption that all the geometrically necessary

dislocations are stored in material hemisphere given by the indentation contact radius, which is not entirely correct in case of nanoindentation, so the considered volume needs to be reassessed. Last, but not least, there is the issue of surface roughness that has much more significant effect in case of nanoindentation. (35)

1.6.4. Microscopy

Although the evaluation of nanoindentation is not based on optical analysis, different methods of microscopy can be utilized when investigating the state of the sample surface, the shape of the indent or the distance from certain points of interest. Both mentioned have a significant influence on the results obtained from the nanoindentation measurements and can help to determine which method of data evaluation is the most suitable for certain material and conditions. Therefore, it is necessary to understand principles behind particular methods of microscopy in order to assess which method is convenient for which analysis.

Basic inspection of sample surface is usually done on light optical microscope (LOM). Continuous optical evaluation of grinding, polishing and etching procedures is necessary to achieve desired state of the sample. LOM can be also used for simple evaluation of shape and position of the indent. For more specific analyses the following methods are used.

Scanning Probe Microscopy

Surface roughness is a key parameter for a successful nanoindentation experiments. The most common microscopy method, that is able to create a profile of sample surface, is the Scanning Probe Microscopy (SPM). During the SPM the tip is in direct contact with the surface which is being scanned, basically scratching the whole area with a minimal force applied. The biggest advantage of this method is that it usually can be carried out on the nanoindenter directly, so there is no need to transport the sample from one device to another, remount it and then search for desired location. In-situ realization of SPM is not only time saving, but in case of active samples it is also more economic. SPM scanning is normally used for an inspection o indentation analyses where it can i. e. measure the pile-up for subsequent correction of contact area. It is also used to obtain the surface roughness profile prior the indentation itself. The usual output of SPM analysis are two sets of pictures – the first depicts the tip displacement and the second depicts forces induced between the tip and specimen surface. Each set contains one picture taken during a left-to-right movement of the tip and another taken during a right-to-left

movement. Such outcome enables better analysis of the character of obstacles that are located on the surface.

Atomic Forced Microscopy

Another method of direct indent analysis is the Atomic Forced Microscopy (AFM), which is very similar to the SPM. On the contrary to the SPM, this method provides much better resolution thanks to a smaller tip radius and multiple forces that are affecting the scanning tip. In another words, the tip is not sensing only mechanical forces induced by a direct contact, but it is capable to sense also chemical bonding, electrostatic forces, van der Waals forces and so on. Although some nanoindenters already offer the possibility of in-situ AFM measuring, the AFM is usually conducted on a separate device.

Scanning Electron Microscopy

With the scanning electron microscopy (SEM), it is possible to acquire surface images in high resolution. SEM uses an electron source which is producing a focused beam of electrons with high energies. Such electrons undergo many interactions within the sample and therefore do not penetrate the material into significant depths. This beam is then able to raster the image or steadily analyze one exact position on the surface. The interaction between electrons emitted from the source and sample electrons generates two types of out coming signals – X-rays and electrons (back-scattered electrons, secondary electrons, auger electrons, etc.). Thanks to both signals, the SEM can be utilized not only for surface profile examination, but also for chemical composition, grain structure analysis and so on.

To characterize the material texture, grain orientation, size and distribution the method of electron back-scatter diffraction (EBSD) is used. Within the EBSD the electron beam is aimed at a sample surface tilted under 70° angle, while the diffracted electrons are depicting certain pattern on a phosphor screen. The electrons loose some of their energy in material surface and then they are scattered back towards the fluorescent screen. Before they reach the screen, they are once more scattered by a set of lattice planes, which forms the beam of back-scattered electrons into a conical shape. The intersection of this shape with the screen creates Kikuchi bands, a pattern of parallel lines perceived by the camera behind the screen. The width of each Kikuchi band is related to a crystallographic plane, which is subsequently used for determination of grain size, structure and orientation.

Chemical composition of the sample can be studied by the energy dispersive X-ray spectroscopy (labelled as EDX or EDS). This is usually done as an in-situ measurement on SEM as well. The method uses a detection of characteristic X-rays emitted after the interaction of high energy electrons with electrons in sample material. High energy electrons excite electrons in material which subsequently deexcite and emit photons with the energy characteristic for each element. By detecting these X-rays and assigning their energies to separate channels, specific elements can be subsequently determined from a database.

1.6.5.   Indentation tips & materials

For the purposes of nanoindentation is possible to utilize pyramidal, conical and also spherical tips. Each geometry has its advantages that are predetermining the tip for a specific use. The advantage of conical tip is its axial symmetry. Regarding spherical tips, their main advantage is a smooth transition between elastic and plastic contact. Therefore, they are often used for testing of rather soft materials or to imitate the contact damage while simulating service conditions. Specific type is then the sphero-conical indenter, which is a conical indenter with a semi-spherical tip.

The most common pyramidal tips are Berkovich, Knoop and cube-corner. Berkovich indenter tip is often used for very small applications as the precision of its manufacturing is the highest of all three mentioned pyramidal indenters. The tip radius is in case of a brand new Berkovich indenter usually between 50-100 nm, while the wear normally increases the radius to around 200 nm. Cube-corner indenter can be considered as an alternative to the Berkovich, but with a much sharper tip angle of 35,26°. The Knoop indenter is due to its asymmetricity used mainly for very hard materials and for the investigation of sample surface anisotropy. (28)

Tips for nanoindentation are usually made of material as hard as possible. Diamond, sapphire or cubic-boron-nitride (cBN) are often used because they obtain the least damage due to their high hardness. It is basically just the wear that is affecting the tip at RT. Environmental changes associated with elevated temperatures induce chemical reactions with atmosphere and sample material. Thus, the material selection specifically for high-temperature nanoindentation must be considered. Diamond tips for example have the highest hardness, so they are most frequently used in RT applications, but they have significant limitations concerning their use at higher temperatures. Diamond is more susceptible to the oxidation than sapphire that does not have such high mechanical properties, but shows better thermal stability as shown bellow. Once the

volume of the tip material is very small, even slight change in its dimensions or properties have severe impact on the results. (36)

From practical point of view, it is desired that materials have predictable development of their mechanical properties as a function of the temperature. Following graphs show hardness and Young's modulus of multiple materials as a function of the temperature.
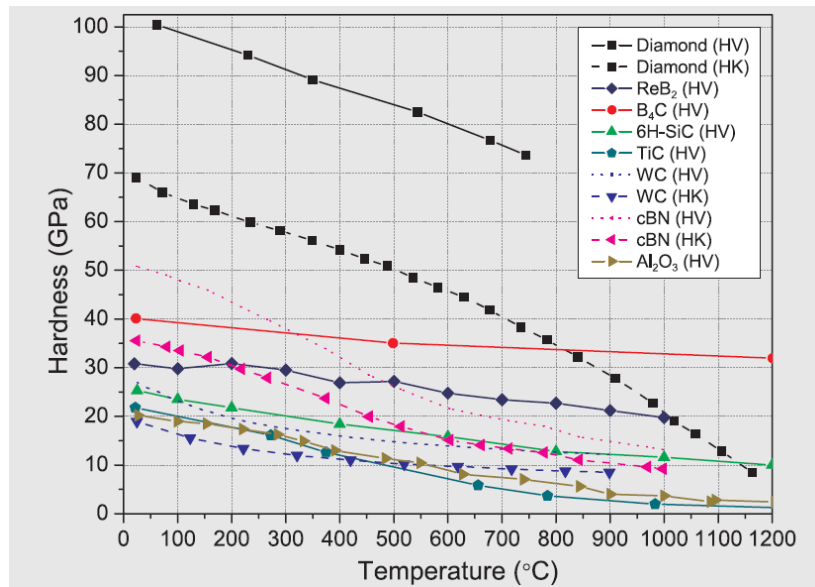
Figure 14: Hardness as a function of temperature, from: Wheeler, J. M. a Michler, J. Review of Indenter Materials for High Temperature Nanoindentation, fig. 2

As it is obvious from the graph, carbides of boron (B4C), silicon (SiC) and tungsten (WC) keep their hardness the most leveled compared with other materials. Hardness of diamond remains superior up to around 800°C, but steep decrease of its value is obvious within the entire temperature range. (36)
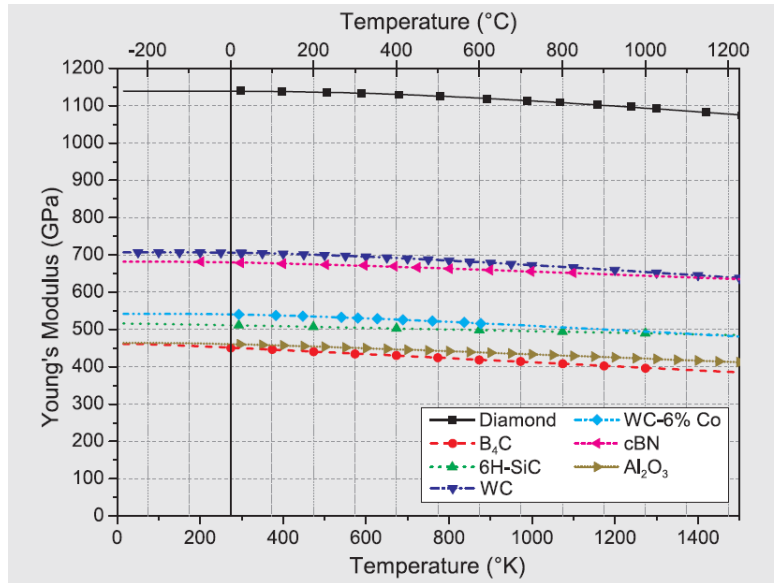
Figure 15: Young´s modulus as a function of temperature, from: Wheeler, J. M. a Michler, J. Review of Indenter Materials for High Temperature Nanoindentation, fig. 3

The most leveled function indicates sapphire (Al2O3) and cBN. Even though, most of the materials show quite leveled characteristics, the smaller the changes in tip material properties, the less calibration measurements and corrections must be done. According to these criteria, the best values has sapphire that changes its modulus within the range of approximately 6%. As it was already mentioned, the main limitation for diamond tips is the oxidation. Research experience and various experiments have proven, that these tips undergo severe damage at temperatures higher than 400°C, although the show a good resistance up to this temperature. CO and CO2 is being produced when the diamond oxidation occurs. On top of it, reaction of the diamond and steel results in the creation of Fe3C carbides, that destroys the tip rapidly. Sapphire on the other hand appears to be inert in contact with oxygen at elevated temperatures and shows only slight degradation in contact with high chromium steels at temperatures around 700°C. Tip degradation in general can be also boosted by humidity. (36)

1.6.6. Nanoindentation issues

A manor of contact surface deformation represents one of the most significant distortions of nanoindentation results. The material at the contact periphery can either cave in, which is called the sink-in, or pour out above the surface level, which is called the pile-up. Both events affect the contact between the tip and the sample and because commercial nanoindenters can not directly measure neither of them, they can spoil the measurement if not considered during data evaluation.
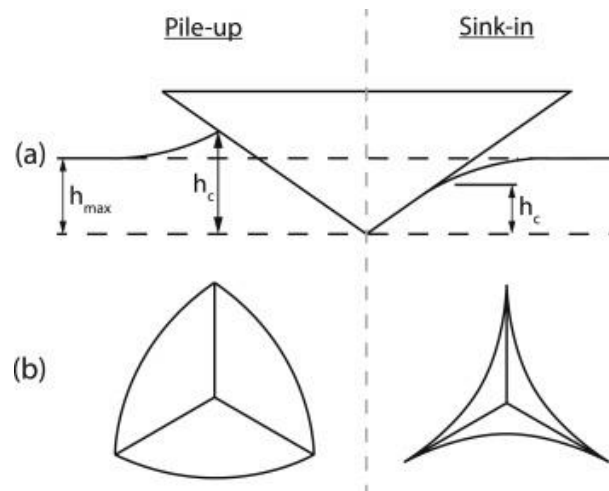
Figure 16: Side view (a) and top view (b) of the swelling events, from: Hardiman, M.; Vaughan, T.J.; McCarthy, C.T. - The effects of pile-up, viscoelasticity and hydrostatic stress on polymer matrix nanoindentation

Pile-up usually occurs at materials with small ratio of yield strength to Young's modulus (Y/E = 10^{-4} – 10^{-2}) and it causes an increase of measured hardness. Softer materials generally have larger plastic zone beneath the tip, so there is more material that could be displaced upwards by the plastic flow. On the contrary, the sink-in can be observed at materials with high Y/E and it causes rather underestimated results. Due to both phenomena we have to distinguish between residual contact area (A_r), which involves the area of pile-up or sink-in material, and therefore is larger or smaller than projected contact area (A_c), that is supposed to approximate the tip-specimen contact area accurately. Because the tip-specimen contact area is an important input into the hardness calculations, its estimation should be as precise as possible in order to achieve reliable result. (25)

Mutual thermal drift of the tip and the sample also must be taken into account when measuring in nano-scale. The drift in general might be caused by mechanical influences or by a temperature gradient (thermal drift) and it is expressed as the displacement versus time [nm/s]. Mechanical influences are usually external vibrations or vibrations induced by the flow of cooling or inert gases during high-temperature measurements. Both can be prevented by setting appropriate measurement conditions. Thermal drift can distort the data about indentation depth as well. To eliminate the temperature gradient, it is necessary to maintain the measurement temperature as constant as possible. Temperatures of the tip and sample should be also equal, which is being achieved by bringing the tip in the proximity of the sample surface for a certain time period prior the indentation begins. During calibration measurements the thermal drift is mitigated by the selection of material with low thermal expansion such as fused silica or fused quartz. (33)

The creep may also represent an issue during the nanoindentation. It manifests as a change in the indentation depth under a constant applied load. The problem is that the same behavior is also induced by the thermal drift, which makes it difficult to distinguish. As it was already mentioned, the creep is minimized/analyzed by maintaining a constant load for certain dwell time. Unlike the thermal drift, the creep is expressed as a percentage difference between the indentation depth at the beginning and at the end of the dwell time. The analysis of material relaxation can be considered as an analogy to the creep measurement, when the tip is kept in the constant depth and the change in the load is calculated.

Many observations of hardness changing with the indentation depth have been made. It was discovered that at small depths (dozens of nm) the hardness decreases as the tip goes deeper into the metal. This phenomenon was called the indentation size effect (ISE). ISE was documented for instance during an experiment with Fe-10Cr alloy irradiated by helium and hydrogen ions. While performing the nanoindentation, the hardness was observed to be increasing until the tip reached the depth of 50 nm (reverse ISE) and then, once the tip went deeper than 50 nm, the hardness started to decrease with further penetration. Such behavior can have many reasons. Metals tend to oxide on the atmosphere, which leads to the creation of hard oxidic layer. Another hard surface layer can be formed during the sample preparation, when grinding and polishing procedures induce strain hardening and residual stresses. The ion irradiation also creates a thin layer with different properties on the surface. Apart from the presence of surface layers, the ISE occurrence is associated with dislocations in crystalline materials. When the indentation influenced volume of the material has dimensions close to the distance between individual dislocations, the number of dislocations within this volume is small. It means that the contact stress required for the initiation of plastic flow must be higher. Such effect of present dislocations increases the influence of mechanical and thermal treatment of sample material. ISE is regarded in Nix-Gao, but not in the Oliver-Pharr computational method. (33)

Additional issues for the nanoindentation can be produced when speaking about irradiated samples. There are two ways to irradiate specimens for subsequent nanoindentation - neutron irradiation and ion irradiation. Neutron irradiation provides satisfactory results, but on the other hand, it involves many difficulties. The exposure of irradiated material in the reactor takes long time to achieve sufficient level of displacement per atom (dpa). The specimen gets highly activated, which dramatically complicates any manipulation or transportation and requires

involvement of radiation control during post-irradiation experimentation. Because of all above mentioned negatives, the ion irradiation is currently a preferred way to obtain samples. Ion beam has a high damage rate, which shortens the time needed for irradiation. It also significantly reduces sample activation and transmutation effects, which then simplifies manipulation with the sample. All that decreases the cost of sample preparation. Furthermore, irradiation parameters like dose, ion flux, ion energy and irradiation temperature can be controlled more accurately than in the case of neutron irradiation. Usually the heavy ions are being accelerated and especially self-ion irradiation brings results of high quality. The sample can be also implanted by helium and/or hydrogen while being irradiated. Concerning disadvantages, there is a limited depth of ion beam penetration (in order of μm) and also relatively inhomogeneous damage profile when compared with neutron irradiation. (29) (37) (38)

Apart from the ISE, other effects induced by the irradiation such as Damage Gradient Effect (DGE) can influence the measurement. Accelerated ions going through the material are not causing evenly distributed damage, which can also affect the measurement. Additional complications can be induced by the fresh material underneath the irradiated layer. This material is more ductile and it is located within the plastic zone surrounding the indent, therefore it affects the measurement of the upper layer even before the tip touches it, causing so called Soft Substrate Effect (SSE). The depth since which we can't neglect the SSE is then called critical indentation depth. (29)

2. Experimentation

Primary objective of this diploma thesis is to establish a common method for nanoindentation testing of ferritic/martensitic steels used in nuclear applications and furthermore to apply the developed methodology to irradiated materials testing in hot cells to determine the irradiation induced material degradation. Knowledge of micromechanical behaviour is also applicable within the plant life extension programs, when it is necessary to determine influences of aging degradation mechanisms. Material testing at temperatures same or close to operating temperatures can provide better understanding of degradation effects impending in the structure. A series of preparation procedures and characterisation techniques were used in order to standardize the method for high-temperature nanoindentation on FM steels.

2.1.   Metallography

Samples used for nanoindentation in this work were cut from a bulk piece of EUROFER 97. Cutting was done on Struers Accutom-100 in rectangular geometry from given bulk piece of material, as shown in figures 17 and 18. Dimensions of cut specimens were 1 x 1.3 cm with 3 mm thickness. Although the nanoindentation can deal with much smaller samples, such size of the sample was chosen because of easier manipulation.

Figure 17: Struers Accutom-100

Figure 18: cutting of the sample

Once the specimens were cut, they have been embedded into a mounting resin, so they could be subsequently grinded and polished. Mounting resin could be either conductive or non-conductive, depends on the microscopy analysis method that will be used in further steps. The Struers CitoPress-30 shown in figure 19 was used to fix the specimens into the ConduFast polymer resin.
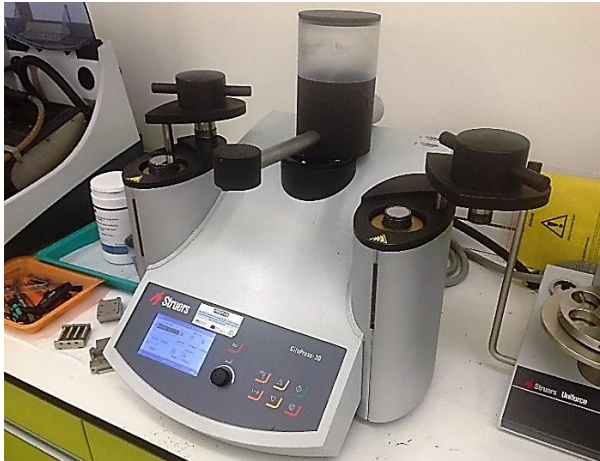
Figure 19: Struers CitoPress-30
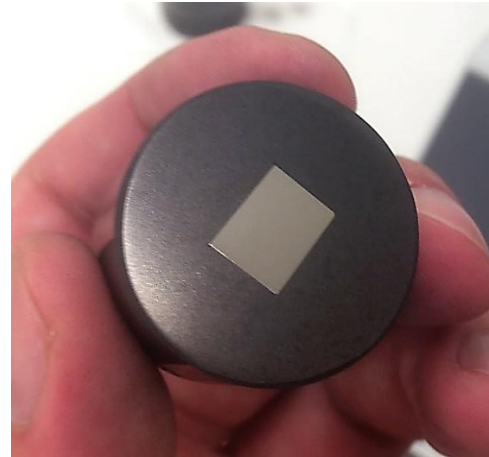
Figure 20: polished sample embedded in the resin

The figure 20 shows the specimen embedded in the resin. After embedding of specimens in resin the most vital step is to prepare a scratch free specimen surface for nanoindentation by grinding, coarse polishing and fine polishing. This is done using Struers Tegramin grinding and polishing tools as in shown in figures 21 and 22. Grinding and polishing steps were performed using different emery papers with varying particle diameters at different force and time. Grinding and polishing steps are described in table 7 below. The final step of fine polishing is done with OPS solution. In between each step the samples were cleaned in the Struers Lavamin automatic cleaner, to remove particles on surface from previous steps.

	Disc	Dosing	Force [N]	Rotation [rpm]	Time [min]
Step 1	SiC foil #320	Water	80	300/150 co-rotation	3:00
Step 2	MD - Largo	DiaPro All	120	150/150 co-rotation	5:00
Step 3	MD - Dac	DiaPro Dac3	90	150/150 co-rotation	5:00
Step 4	MD – Nap	DiaPro Nap1	60	150/150 counter-rot.	3:00
Step 5	MD – Chem	OPS	40	150/150 counter-rot.	2:30

Table 7: Parameters of grinding and polishing
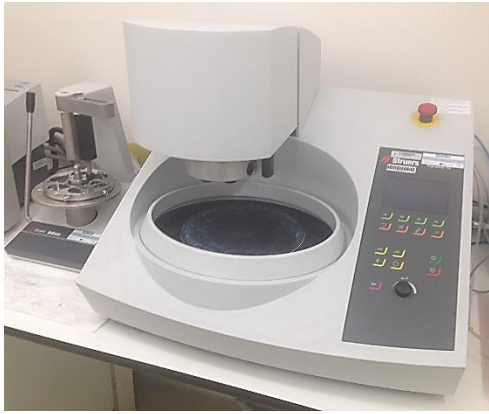
Figure 21: Struers Tegramin-25
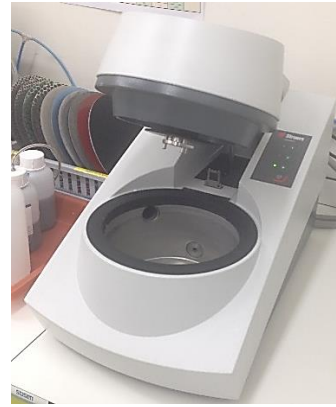
Figure 22: Struers Lavamin automatic cleaner

To determine the microstructure of the specimen additional metallographic sample preparationds methods are required, such as electro polishing or electro etching. Furthermore advantage of electrolytic methods is to reduce the residual stress in the specimen produced from classical grinding. This is done at the expense of aggravated surface roughness, as shown in contact microscopy resuts. The Electro etching on the other hand reveals more of the materail structure, which is done If the specimen is meant to be electro etched/polished, it needs to be at first removed from mounting resin. This has to be done carefully, so there are no scratches are created on the polished surface. After cutting out from the resin, the samples had to be cleaned in the ultrasonic cleaner as in figure 23.

Figure 23: Ultrasonic cleaner

Figure 24: Struers LectroPol-5

Both electrolytic ethichg as well as polishing were carried out automatically on Struers LectroPol-5 as in figure 24. Multiple combitions of electrolyte, temperature and voltage were tried to reveal the microstructure of EUROFER 97 (FM steel). A final recipe was prepared that is optimal to reveal the structure - room temperature 22°C, 10% solution of oxalic acid, 5V. Electro etching/polishing was done in 3 steps of 10 seconds each, so the surface quality could be monitored. The etchant did not come into a contact with the entire surface, but its effects

were limited on the area of 0.5 cm^2 thanks to a mask, so the whole specimen could be devided in separated areas with different surface treatment. The quality of specimen surface for microstructural studies produced by fine polishing with OPS, electrolytic polishing and electrolytic ecthing are shown and discussed in chapter 3.1.

2.2. Microscopy

Various surface roughness techniques and methods as described below (2.2.1-2.2.4) are used to determine if the surface quality and roughness of prepared samples are in required conditions for nanoindentation experiments. The key parameter to be evaluated is roughness, specifically the arithmetic average of roughness profile (Ra), which should not exceed 30 nm. Final treatments applied on surfaces of both samples were different, resulting in diverse roughness parameters for each sample. Apart from the surface profile the grain structure and chemical composition is also determined through SEM.

2.2.1. Light Optical Microscopy

First tool to examine the sample surface is the analysis on the light optical microscope. The LOM is equipped with image acquisition software to visualize the basic structural details like precipitates, inclusions, cavities and grain boundaries. The structure obviously becomes more visible with increasing time of electro polishing/etching. Under the light optical microscope it was possible to see reminders of boundaries of former austenitic grains. To be able to see the martensite at much higher magnification or using scanning electron microscopy. LIECA LOM was used as shown below in figure 25.

Figure 25: Light optical microscope

2.2.2. Scanning Probe Microscopy

In order to check if the surface parameters during sample preparation were met, SPM and AFM scans were conducted. Starting with the SPM, firstly the specimen was attached on the magnetic table of the nanoindenter. Then the optical head was moved above the specimen surface and the view was focused, so a sharp image was obtained, which helped the machine to estimate the contact height. Once the optical head was focused, sampling areas were selected on the surface and the quick approach was conducted with a standard load head. The software of the nanoindenter then kept the height at which the contact occurred so the following approaches were faster. Both specimens had the surface divided into areas that have been treated differently. It was therefore convenient to place a sampling area into each part of the surface, so it was possible obtain multiple results. Once sampling areas were created, parameters of SPM scanning were set and the approach with standard load head was initiated (high load head is not suitable for SPM scan). Parameters used in this SPM scanning were – scanning area 50 x 50 µm, tip velocity 50 µm/s (0,5 Hz), force applied 2 µN.

Figure 26: Sample mounted on the magnetic table of the nanoindenter

2.2.3. Atomic Force Microscopy

AFM scanning was done on Dimension Edge apparatus by Bruker shown in the picture below. On the contrary to the magnetic table of the nanoindenter, the sample is mounted for the AFM scan by the vacuum chuck. The device also has the optics for sample navigation, which helps to select suitable surface area for scanning. Unlike the SPM scan, the AFM is more sensitive to any surface pollution, so an area as clean as possible has to be selected. This particular AFM is capable of scanning two sizes of the surface – 50 x 50 µm and 100 x 100 µm. Due to relatively long duration of scanning procedure the 50 x 50 µm area was chosen. The resolution of the scan was set up to 512 lines with the tip frequency of 0,5 Hz.

Figure 27: AFM edge, from: www.bruker.com

Figure 28: Sample mounted on the AFM table

2.2.4. Scanning Electron Microscopy

Both analyses, EDX and EBSD, were done on Tescan Mira3 SEM, which was also placed inside the semi-hot cell, so it can analyze active samples. The SEM is capable of high resolution images different using kinds of electrons for better contrast and chemical and structural analyses of the sample surface, as mentioned in chapter 1.7.4. This particular model of SEM uses back-scattered and secondary electrons.
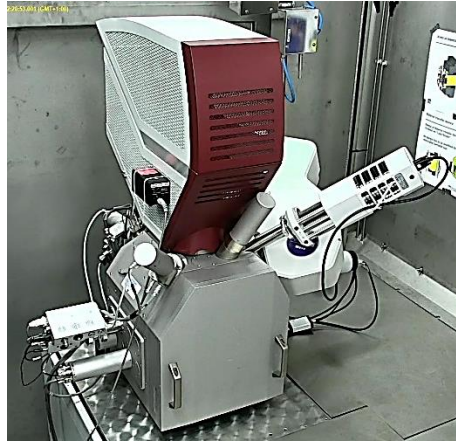
Figure 29: Tescan Mira3 SEM

2.2.4.1. EDX

To verify chemical composition of sample material the energy dispersive X-ray spectroscopy was conducted on the first sample. The EDX measurement was done by electrons with energies of 20 keV and resolution of 10 eV per channel. The results in table 9 might be compared to the chemical composition from the literature mentioned in table 5.

2.2.4.2. EBSD

The purpose of the EBSD analysis was to determine the grain orientation and eventually assign particular phase to the specific grain. Such information is necessary if the site-specific nanoindentation is meant to be done. Sample material was attached to a special holder by a solution of colloidal silver and placed into the SEM´s chamber that was then vacuumed. The surface, which was going to be scanned, was positioned at a specific angle towards the EBSD probe. Although the chamber is not transparent, probe approach was observed via infra camera.

2.3. Nanoindenter assembly

Nanoindentation measurements were done on the TI 950 TriboIndenter from Hysitron. This setup is equipped by the head capable of SPM scanning and therefore the SPM images showed

in the chapter 3.2. were also taken on this device. TI 950 was chosen because of its mostly automated and therefore precise feedback control. The software used to operate the TI 950 is a Tribo Scan 9 also provided by Hysitron. Calculation of data is done by the Oliver-Pharr method, which was already described in chapter 1.6.3.2. Because the device is intended to perform nanoindentation on active samples, the entire assembly is divided into active (inside the semi-hot cell) and non-active part (outside the semi-hot cell). The active part consists of granite desk and frame with three vertically movable heads. The standard load head, which is the first one from the left side, is used for nanoindentation and SPM scanning. The high load (microindentation) head is in the middle and the optical head that enables the navigation on the sample surface is on the right side. The load range of the standard head is from 0.1 µN to 10 mN, while the high load head is capable of measuring between 10 mN and 2 N.
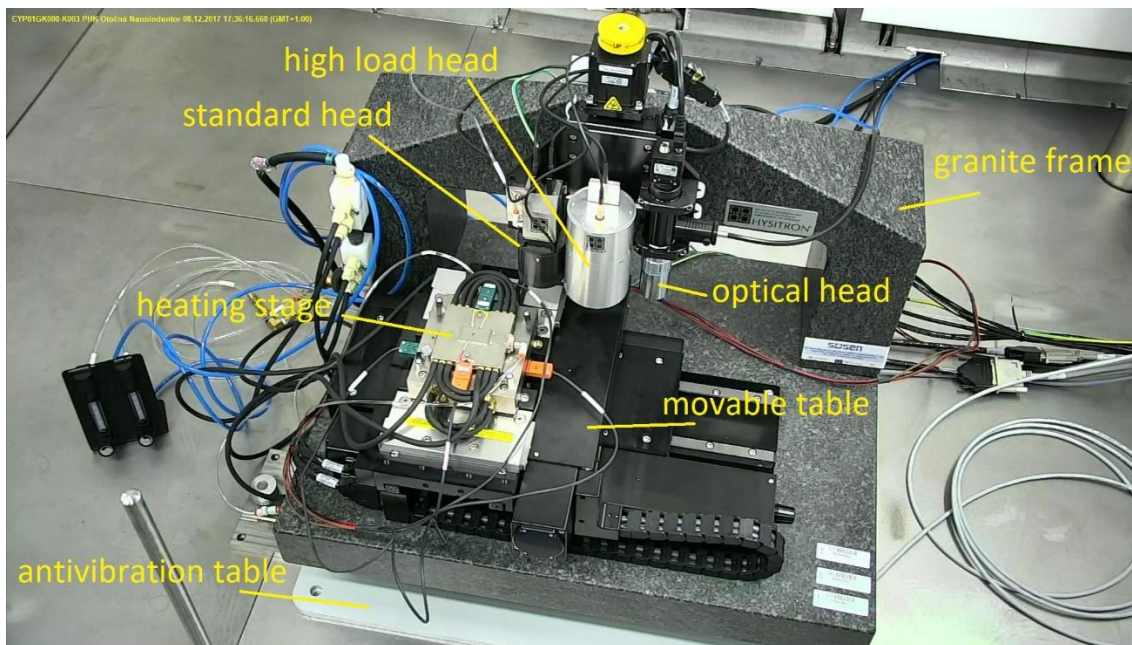
Figure 30: TI 950 TriboIndenter - basic model, from: www.hysitron.com

Rough vertical positioning of all three heads is done through an electro motor, while the precise control of indenter load and position in vicinity from the sample is assured by a piezo movement. Its displacement resolution in indentation axis is 0.006 nm with a load range from 0.07 µN to 10 mN. The resolution of SPM scan claimed by the manufacturer is 20 nm. Feedback control for the piezo mechanism is provided through a three-plate capacitive transducer that sends signal to the dedicated digital-signal processor and field-programmable gate array embedded control system. The optical head has a camera fitted by the objective with a resolution of 1 µm and 20x magnification. The camera broadcasts the video into the control computer, which enables precise navigation on the sample surface. Horizontal positioning is

done through electro motors that are moving the table in X and Y axes, while the precise movement is done again by the piezo element with an accuracy of ± 10 nm.

The sample can be mounted on a magnetic table for room temperature measurements or into a xSol 800 heat stage in case of high-temperature nanoindentation. The magnetic table is a stainless steel construction designed to mount up to 5 samples. There are two polycarbonate surfaces for an optic-probe tip offset calibration, one at each end of the table.

Figure 31: Magnetic table for sample mounting during room temperature nanoindentation

The xSol 800 high-temperature stage is composed of upper and bottom part. Each part has a ceramic heating element so the sample is heated from both sides which eliminates the thermal gradient within it. Temperature homogeneity of the sample claimed by the manufacturer is ± 0.2°C, while the temperature control precision is ± 0.1 °C. The actual temperature of upper and bottom part is measured by a total of four thermocouples (two thermocouples connected to each part from opposite sides) and controlled by the PID regulator. Inside the heat stage there is also a small orifice that serves as an inlet for the inert gas. Apart from the inert gas hose the heat stage is connected to the water circulation loop with a coolant temperature maintained at constant level. This ensures dimensional stability as well as fast and uniform heat removal. The xSol 800 is also equipped by the polycarbonate sample for tip-to-optics calibration.
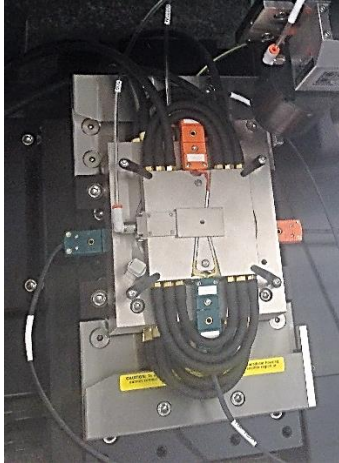
Figure 32: xSol 800 heating stage - closed
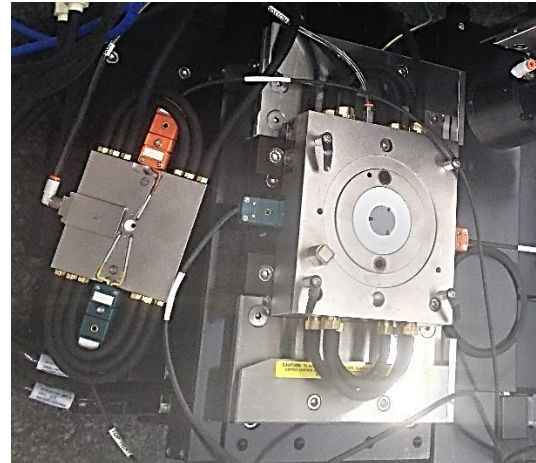
Figure 33: xSol 800 heating stage - disassembled

Although the TI 950 is normally delivered in an environmental isolation box, the entire apparatus in this case sits on an antivibration pedestal inside the semi-hot cell. Such separation from the outside environment should be sufficient for minimizing of all external interferences that could have a negative influence on the precision of nanoindentation measurements and also enable testing of active materials.
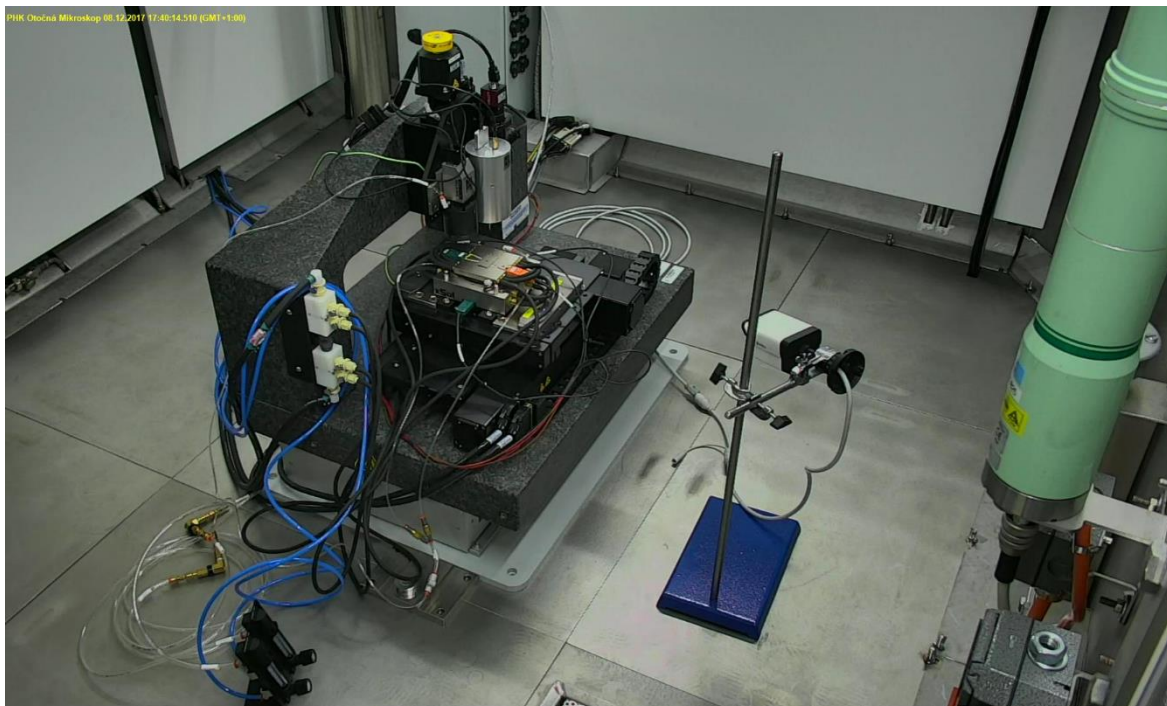
Figure 34: TI 950 placed inside the semi-hot cell

Concerning the non-active part, there are several other pieces of equipment that are providing support functions for the nanoindenter such as cooling, light and inert atmosphere. An air compressor is attached by a small hose to standard head, so the air can be blown down along the tip and provide thermal insulation of the sensitive electronics from the heat generated

below. Then there is a water cooling system with a circulation pump, which supplies a cooling water for the xSol 800 heat stage. To be able to prevent sample and tip oxidation, an inert atmosphere has to be crated around the specimen. Therefore, there is the argon injection system connected to the inside of the heat stage that supplies the argon 6.0 directly to the sample. Argon 6.0 was selected because of its purity that guarantees almost no presence of the oxygen that would cause corrosion of the sample surface. The last piece of external equipment is the light for the objective that is interconnected with the optical head by an optic cable. All those appliances must be located outside the semi-hot cell due to control and maintenance reasons.
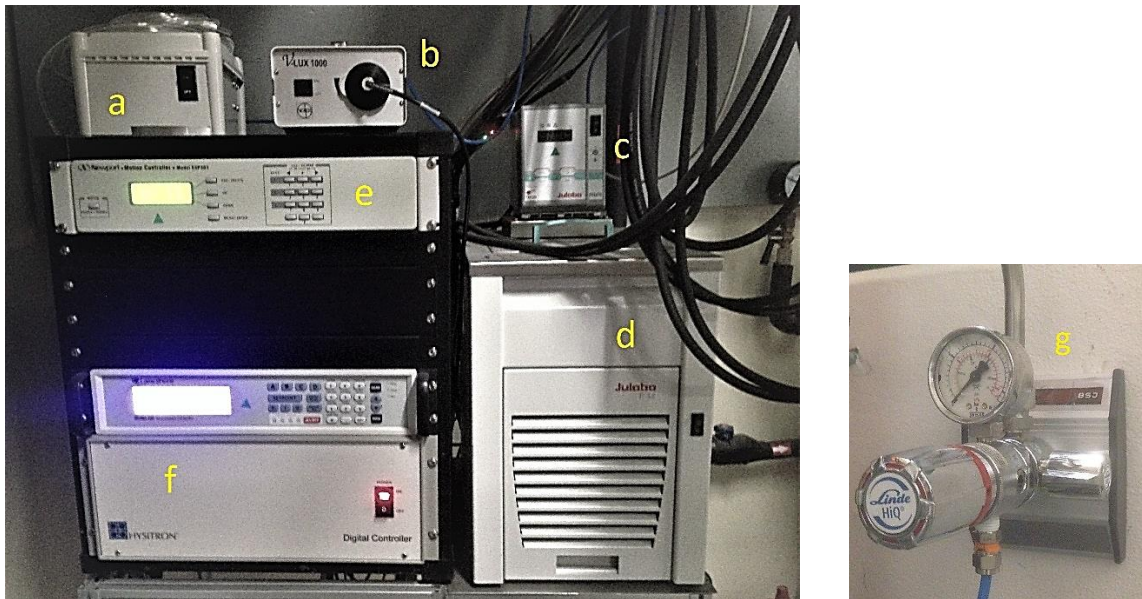
Figure 35: Non-active part of TI 950 assembly, a) air compressor, b) microscope light, c) water temperature controller, d) water circulation pump, e) motion controller f) dedicated digital-signal processor, g) argon regulation valve

2.4.   Calibration

Prior the testing of EUROFER 97 specimens by nanoindentation, it is necessary to carry out a series of calibration measurements in order to standardize the methodology of testing and to adjust key parameters that are affecting that are affecting measurement outputs. Number and order of necessary calibrations may vary between individual nanoindenters. Calibrations described in next paragraphs are specific to the TI 950 assembly.

Tip material selection can be considered as the initial part of calibration procedures. With regards to what was written in the theoretical part, the sapphire was chosen for the standard load tip, because it shows the most leveled characteristics of Young´s modulus and suitable decrease of hardness values with increasing temperature. If the Young´s modulus remains approximately constant within the entire temperature range (RT – 700°C), it means that the tip

compliance changes minimally over this range and less calibration measurements on the reference material can be done. Although the sapphire shows acceptable development of hardness as a function of temperature, its values are getting under 10 GPa at temperatures around 700°C and hardness generally much lower than the one of the diamond might cause significant wear during the measurements. The high load head is due to the supply reasons equipped by a diamond tip, so the measurements at elevated temperatures will have to be conducted with caution and certain limitations.

2.4.1. Optical head calibrations

Because the nanoindentation requires high precision, an accurate movement of the whole apparatus must be assured. At first, it is necessary to conduct so called zoom calibration, if the optical head was moved from its original position on the frame. An adjustment of the optical head position was done due to the installation of xSol 800 heating stage. The purpose is to calibrate the distances measured from the optical image. The optical head is aimed at a certain point visible on sample surface using the blue reticule. Once the point is located, the operator confirms its position and subsequently aims the red reticule at the same point. By doing this, the software of the stage control records the shift in X and Y axes. The initial part of this calibration is shown in the picture bellow.
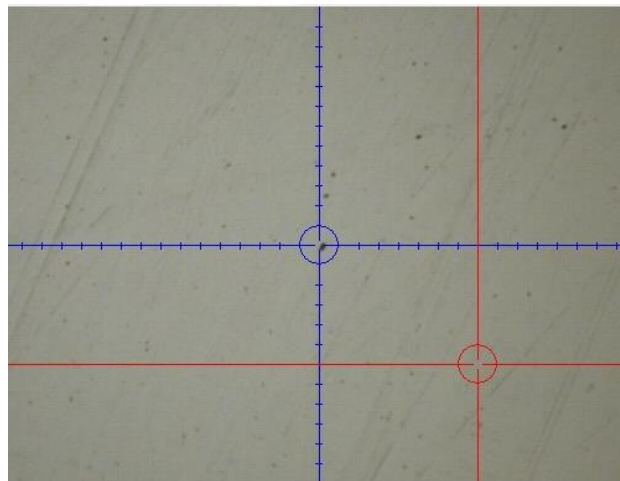
Figure 36: Blue reticule aimed at the point on the polycarbonate surface during the optical zoom calibration

Next is the optic-probe tip offset calibration (further referred as tip-to-optic calibration). This calibration must be done, so it is certain that the indent is made exactly on the spot previously aimed by the optics. Tip-to-optic calibration is conducted on a polycarbonate specimen placed on the periphery of the nanoindenter stage. Polycarbonate is used because it is relatively soft material which does not cause significant wear of the tip. In case of TI 950 TriboIndenter this

calibration is a semi-automatic process. Firstly, the optical head is aimed at an appropriate location within the polycarbonate sample and a sampling area is created. Then the operator selects the option to create a calibration H-pattern. The optical head withdraws and the tip moves above the sample. Because the mutual position of optics and the tip is unknown, the quick approach cannot be conducted and the operator must descend towards the sample manually. Aforementioned quick approach is a procedure, when the nanoindenter finds a height at which the contact occurs. As soon as the tip is in the vicinity from sample surface, the machine conducts 7 indents (2 columns of 3 indents with 1 indent in the middle) that form the calibration H-pattern. Once this is done, the optical head moves back above the polycarbonate and the operator is told to align the center cross exactly to the middle indent. By doing this the mutual position of the indenter tip and optics is adjusted. Such calibration procedure should be done every time the tip encounters an excessive force, which might cause a deflection of the tip from its original position. Tip-to-optic calibration procedure is the same for standard and high load head.
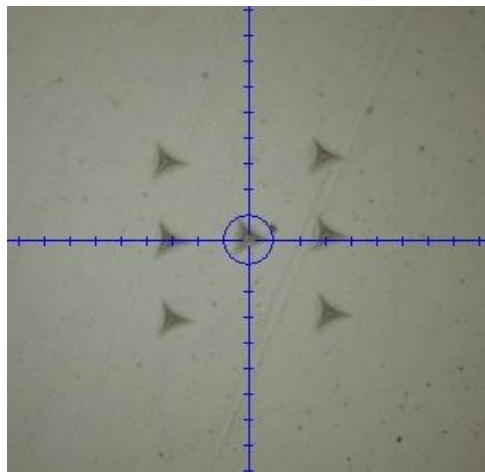
Figure 37: Optics aimed at the calibration H-pattern
(the sink-in behaviour of polycarbonate is apparent from these indents)

2.4.2. Tip area function and frame compliance calibration

The most important unknown to be determined is the tip area function, which must be calculated to be able to subsequently determine the frame compliance. A set of indents is done within the load range corresponding to the depth range intended to be reached during the nanoindentation. A good practice is to start with the highest load value and then decrease it with each indent towards the lowest load. The main reason for this is better stabilization of the transducer. If a calibration sample material of standardized hardness and modulus is available, the tip area function can be calculated from eqs. 6 and 8 given by the Oliver-Pharr

computational method. Such approach is established in the ISO 14 577 – 2 standard. The standard also recommends at least 100 indents to be conducted if a reliable tip area function is to be calculated.

For the standard load head the range of applied load from 1 mN to 10 mN was selected. Although this head is capable of indentation under loads in µN range, such loads and corresponding depths are irrelevant for measurements conducted in this work. Concerning the high load head, the range of applied load from 10 mN to 200 mN was selected, although this tip can be loaded up to 2 N.

Frame compliance test is another essential calibration procedure. The stiffness of the entire nanoindentation apparatus has severe influence on the results. To be able to determine the frame compliance, it is necessary to use a standard material with well known parameters. Calibration standard should mainly have constant values of Young´s modulus and hardness over various indentation depths at each temperature level. It should also have high thermal stability, negligible pile-up/sink-in behaviour and minimal creep. Constant values of hardness over various depths are associated with ISE, that should be completely prevented. Concerning the pile-up/sink-in, these phenomena are dependant on yield strength to Young's modulus ratio as described in the theoretical part. Regarding the primary creep, it can be diminished by selection of a load function that keeps the maximum load at a constant level for a certain time. In this case a load function with a trapezoidal shape was used as shown below.
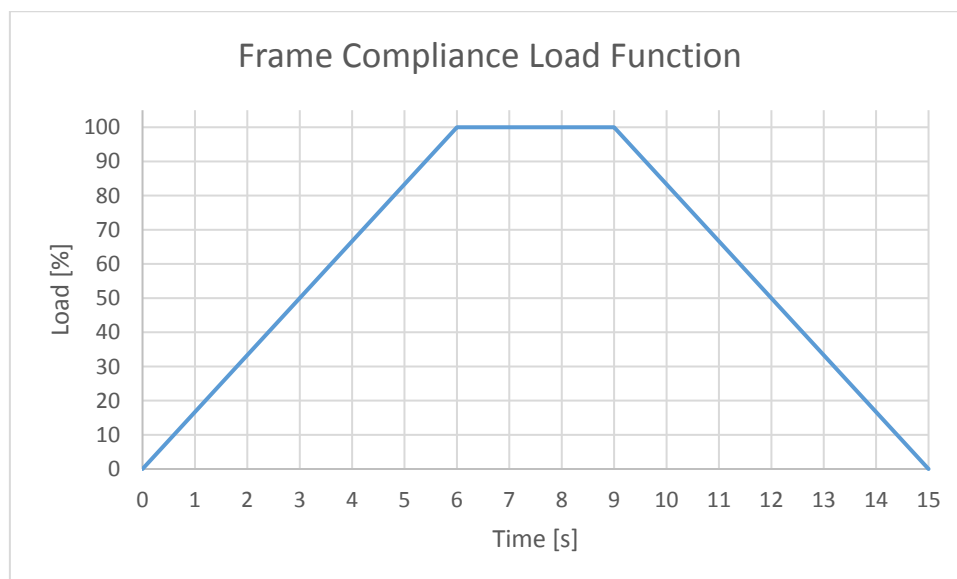
Figure 38: Load function used for frame compliance calibration

Tip area function and frame compliance calibrations were done on the sample made of fused quartz, which has a known value of hardness and reduced modulus at room temperature (diamond indenter: H = 9.25 GPa and E_{eff} = 69.6 GPa; sapphire indenter: H = 9.25 GPa and E_{eff} = 61.8 GPa). Therefore, it is possible to calculate the stiffness of the apparatus, that can be subsequently regarded within measurements. Frame compliance test should be done on other devices for each temperature at which the indentation is planned to be conducted. This is because the heat from the heat stage can affect the frame stiffness and distort the data. In case of TI 950 TriboIndenter the frame should be less affected by the heat coming from below because of several reasons. The shaft of the indenter tip has very low heat conduction, the sample is heated in closed heating stage with relatively small bore ($\emptyset$ = 2 mm) for the tip insertion and the compressed air is blown downwards along the shaft. These reasons significantly reduce the thermal affection of the shaft and therefore contribute to almost constant stiffness. Frame stiffness is represented by a coefficient, which is involved in the calculation of modulus as shown in eq. 8.

As it can be seen from the Oliver-Pharr method and preceding description of calibration procedures, the determination of tip area function and frame compliance is interrelated, so the final values usually result from numerous iterations. Such iteration process starts with the selection of initial frame compliance. A set of 100 indentations with decreasing loads is then conducted and the initial tip area function is calculated by the software. Initial frame compliance and tip area function lead to some values of H and E_{eff}, that are subsequently compared to reference values. If the obtained values are lower/higher than the reference ones, the frame compliance must be adequately increased/decreased. Adjusted frame compliance is than substituted into the previously done calculation of the tip area function and the new tip area function is consequently applied on the data from frame compliance calibration. This cycle is repeated until the values of H and E_{eff} are as close as possible to reference values.

2.4.3. Temperature stability verification

High-temperature nanoindentation is very sensitive to temperature stability that needs to be verified prior any measurement and it also needs to be continuously monitored. To make sure the temperature stays at the desired set point, the heat stage was heated up from 23-100-300-23°C and then again from 23-500-700-23°C with a ramp rate of 10°C/min. Similar heating cycles will be done during the measurements. Standard deviations between the average

temperature sensed by the top and bottom thermocouples and temperature set point were calculated.

2.5.   Nanoindentation

All nanoindentation measurements were done according to the load control method. A specific load function was designed for the purposes of metallic materials testing. This function regards creep behaviour of the material as well as the thermal drift. The load function originally from the Round-Robin Protocol is depicted in the figure 39.
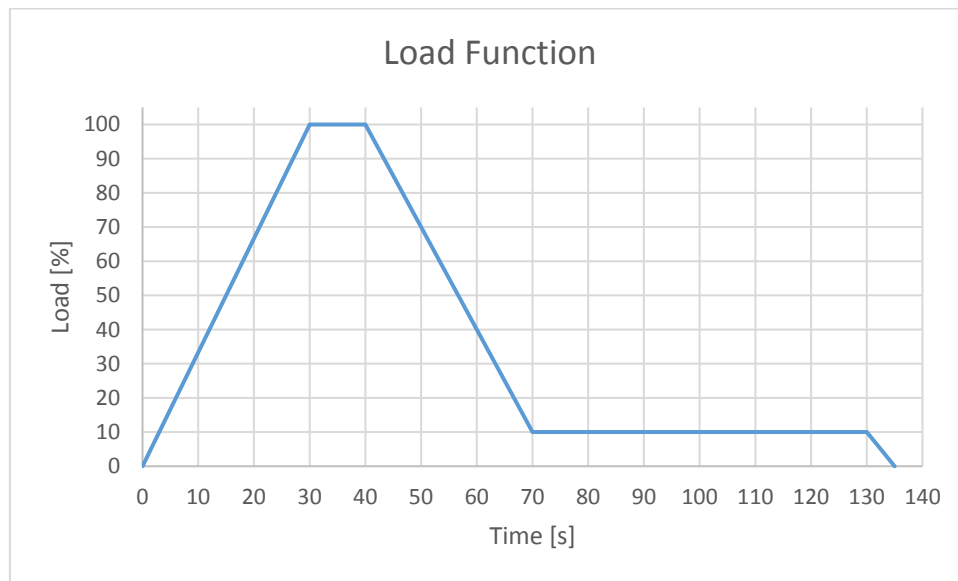
Figure 39: Load function used for the nanoindentation

The load is being applied and the maximum load (F_{max}) is reached within the first 30 seconds (t_{load}). F_{max} is then maintained for another 10 seconds during so called dwell time (t_{hold}). This part of the loading function is necessary to minimize the influence of creep on the measurement, as it was already mentioned in theoretical part. During another 30 seconds the tip is unloaded to 10% of F_{max}. Such load level is subsequently maintained for 60 seconds in order to check the stability and thermal drift. Final unloading back to the zero is done within another 5 seconds, but this part of the loading function does not have any significance for the measurements. The indentation conducted according to this load function is considered as quasi-static. The entire thermo-mechanical sequence of the measurements is tentatively depicted in a tentative graph below.
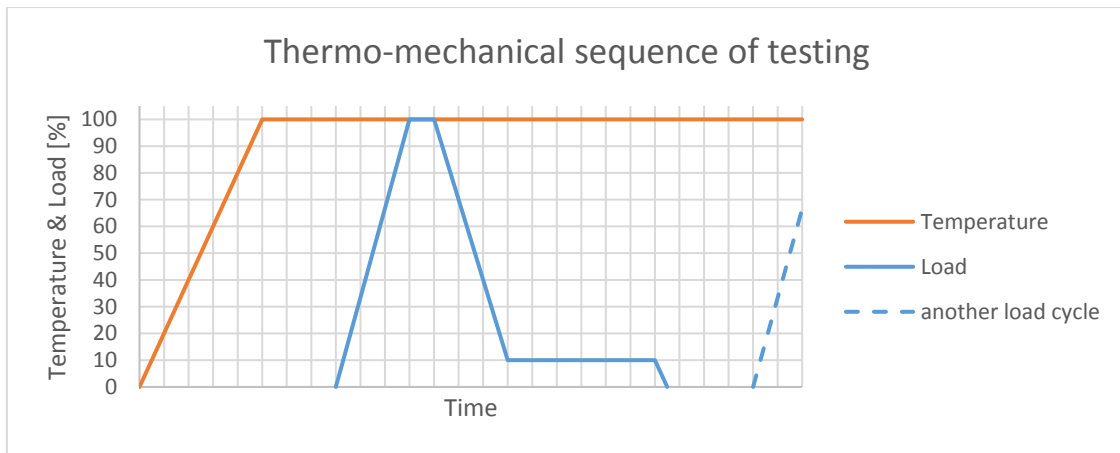
Figure 40: Thermo-mechanical sequence of high-temperature nanoindentation

Once the sample have reached the desired temperature according to thermocouples, it is left to stabilize for approximately one minute, before the nanoindentation sequence is launched. The nanoindenter then must move the tip above the target location and it leaves 45 seconds to settle the motors and then another 60 seconds for the piezo settle time before the loading. During that second interval the thermal drift measurement also takes place. After complete unloading the tip shifts to next position and repeats the motor and piezo settle time intervals, before it starts another loading cycle.

2.5.1. Room temperature nanoindentation

2.5.1.1.   *Standard head nanoindentation*

Due to a limited amount of time available for standard load nanoindentation, the room temperature tests were conducted on xSol heating stage with heating elements turned off. Using only one table for mounting of the sample means that it is not necessary to calculate the frame stiffness for each configuration. The test matrix contained 25 indents (5x5 array) that were conducted under 5 mN load. Horizontal and vertical spacing between each indent was 20 µm. Nanoindentation was conducted on electro etched, electro polished and OPS areas.

2.5.1.2.   *High Load head nanoindentation*

Samples were mounted on elevated steel pedestal and glued by the colloidal silver paste, so their position was fixed. This technical solution had to be done due to safer manipulation with the tip. Without the pedestal the optical head would have to descend too low in order to focus on the sample surface, that the indenter tips would get into a contact with other parts of the TI 950 assembly. Such unintended contact might cause a destruction of both tips that are located several centimeters bellow the level of the optical head. The same technical solution was

utilized during the calibration of the tip area function and frame compliance to achieve the same stiffness.
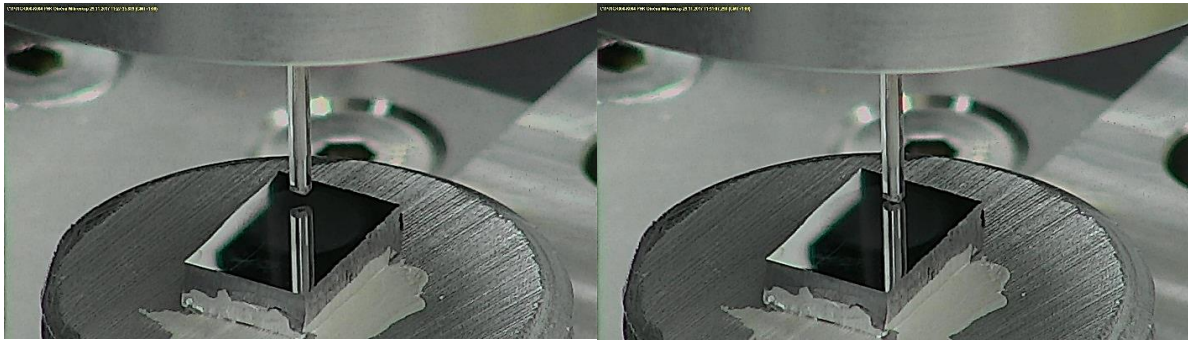
Figure 41:Indeter tip approaching the sample (left) and in contact (right)

Each measurement represents a set of 25 indents. Indents form a 5 x 5 matrix with 50 µm spacing in between each of them. Such gap should guarantee that the deformation induced by one indent will not affect material underneath the tip during another indentation. All three types of areas were indented.

2.5.2. High-temperature nanoindentation

During the nanoindentation at elevated temperatures the inert atmosphere and protective air flow must be provided. Sufficient flow rates were determined at the level of 1,5 l/min in case of argon 6.0 injected into xSol heating stage and 1 l/min for the compressed air going along the tip. The first value is based on the recommendation from device manufacturer. The Hysitron company recommends flow rates between 1,5 and 2 l/min when using argon 5.0. Since the gas with better purity was utilized, the lower flow rate was chosen from the recommended interval. The argon economy also had an influence on this decision. Concerning the air flow, the rate of 1 l/min was chosen based on experience and regarding relatively low impact on the tip. Such flow rate induces an acceptable thermal drift. The ramp rate of the temperature increase was 10 °C per minute. All high-temperature measurements were done under these conditions.

2.5.2.1. Standard load nanoindentation

The standard load nanoindentation was successfully conducted on all three areas at temperatures of 100, 300 and 500°C. Some indents were done also at 700°C, but the quality of the results was poor, so it was decided to abandon this temperature. The test matrix had a form of 2 x 8 array with 20 µm spacing between indents. Selected load level was 5 mN, which is in the middle of the calibration range. Up to 300°C it was possible to carry out the measurements

as a set of automated methods. The matrix had firmly defined dimensions and the operator selected only the position of the center or the first indent. The tip subsequently moved above the sample, descended on the position of the first indent, found contact and after 1 minute and 30 seconds begun the with indentation. At 500°C the thermal drift started to cause significant errors and the indentation had to be conducted in piezo automation mode. On the contrary to automated methods, piezo automation begins with the SPM scan of sampling area, which means that the tip stays much longer in contact with the surface. Indent positions are then manually selected by the operator from the topographic or gradient map obtained by the SPM. This method takes more time, but it brought the thermal drift values back into acceptable interval. Unfortunately, this way of indentation did not provide sufficient compensation of testing conditions at 700°C.

2.5.2.2.   *High Load head nanoindentation*

Due to a mistake of the supplier, the component that provides the cooling air for the high load head was not delivered on time for these experiments. In combination with the fact, that only a diamond tip was available, it was decided to conduct fewer indentations to avoid rapid tip oxidation and degradation that would distort measured data. As a result, the indentation was done only at temperatures of 100 °C, 200 °C and 300 °C. Also the range of applied loads was narrowed, so the first sample was loaded only by 50 mN, while the second one was indented under 100 mN. Indentation at 10 mN at RT showed the largest standard deviation, so it was omitted. Measurements were done on electro polished and electro etched area, but not on the OPS area. The reason for abandoning this area was also the need to reduce the number of high-temperature tests with diamond tip. Furthermore, the optical analysis on LOM showed that the OPS polishing does not reveal the material structure enough to be able to aim the indenter at a specific grain or boundary, as shown in results below. A matrix of 16 indents (2 x 8 array) with 20 μm spacing was done within each measurement.

3. Results & Discussion

Chapter 3, sections 3.1-3.5, present results from microscopy and nanoindentation. Firstly, the images of ferritic-martensitic structure in the test specimen from optical and contact microscopy (AFM, SPM) are shown as a prove of specimen surface quality for nanoindentation and SEM. Calibration outputs presented show the capability of the entire apparatus to perform measurements with sufficient precision. Finally, the nanoindentation data are going to be analyzed and discussed.

3.1.   Light Optical Microscopy
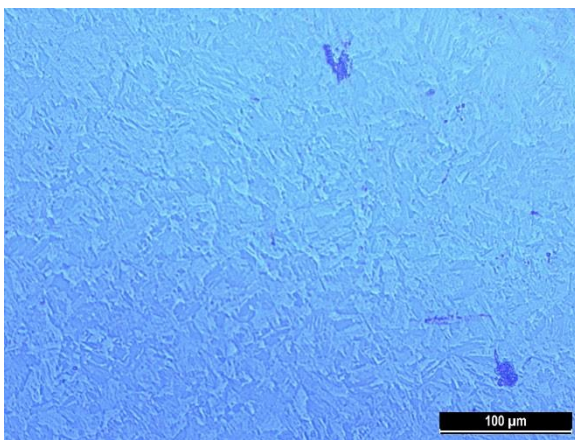
Figure 42: EU 97 after OPS (20x magnified)
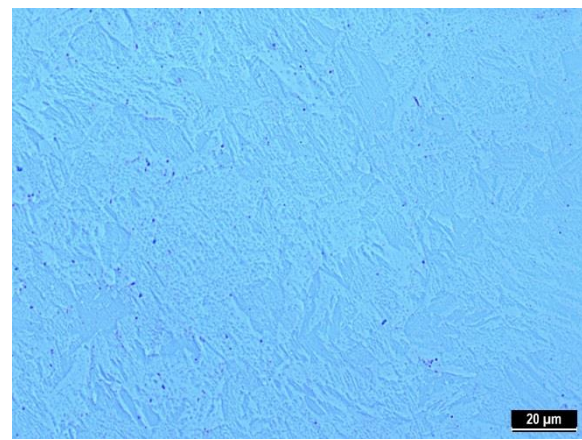
Figure 43: EU 97 after OPS (50x magnified)

Two specimens of Eurofer 97 from the same batch of material were mechanically grinded and fine polished by OPS so they were free from surface scratches. Figures 42-43 show the microgrpahs of specimens surface after OPS polishing. Images does not reveal the detailed structure but some precipitates can be observed on the surface (dark sports on bright surface). From OPS polished specimen surface it is hard to determine the grain size or to define the grain boundaries. Such information allow to utilize the capabilities of indentation on specific grain or boundary. Although these measurements were not intended within the scope of this work, they will be required in future nanoindentation experiments. Specimen 1 was electrolytically polished and specimen 2 was electrolytically etched to determine the structure of EUROFER 97 and at same time to reduce the residual stress created in the specimen surface by classical grinding and polishing. Figures 44-49 & Figure 50-55, represents micrographs from electrolytically polished and etched specimens respectively.

Sample 1 – Electro polishing
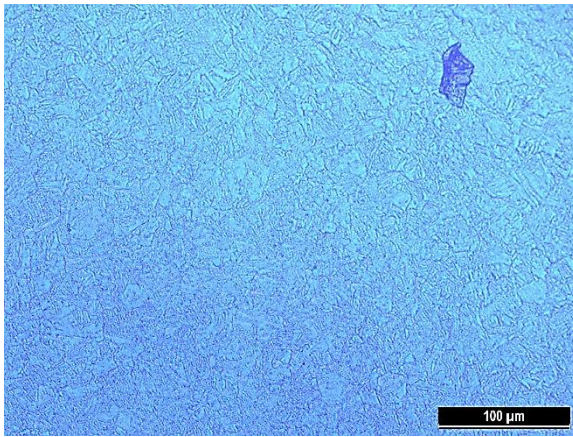
Figure 44:EU 97 after EP 10s (20x magnified)
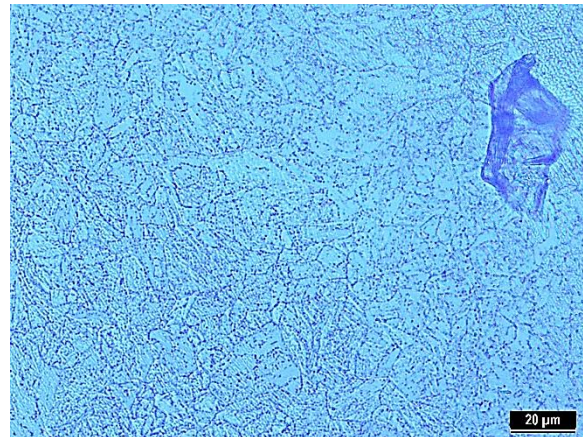
Figure 45: EU 97 after EP 10s (50x magnified)
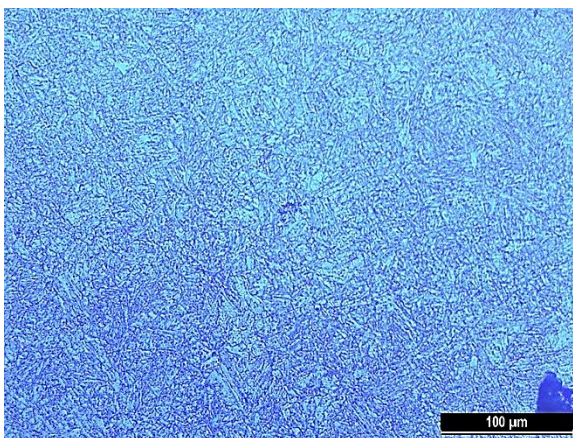
Figure 46: EU 97 after EP 20s (20x magnified)
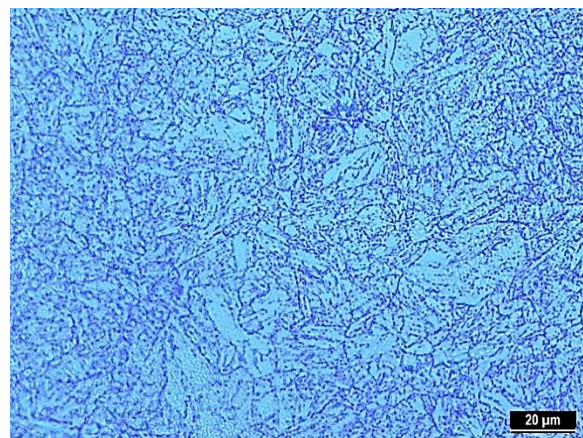
Figure 47: EU 97 after EP 20s (50x magnified)
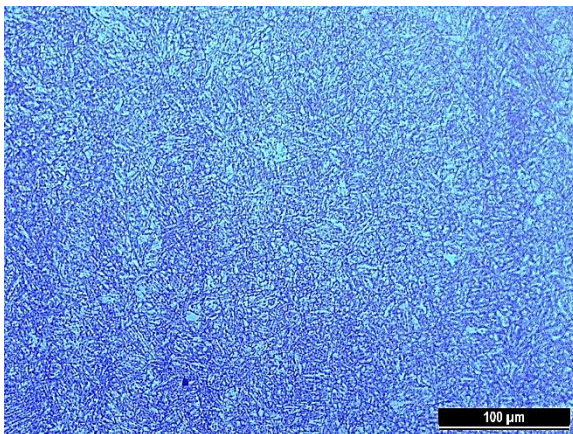
Figure 48: EU 97 after EP 30s (20x magnified)
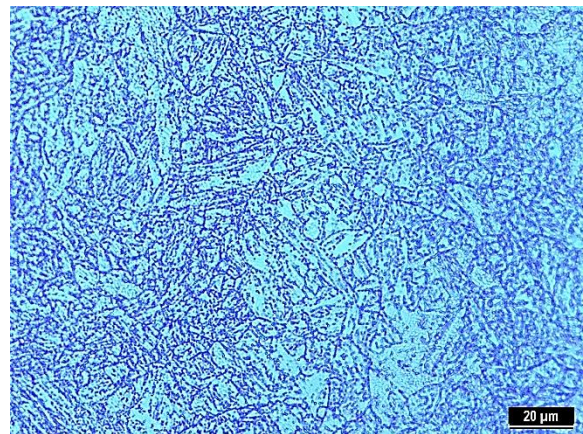
Figure 49: EU 97 after EP 30s (50x magnified)

Sample 2 – Electro etching
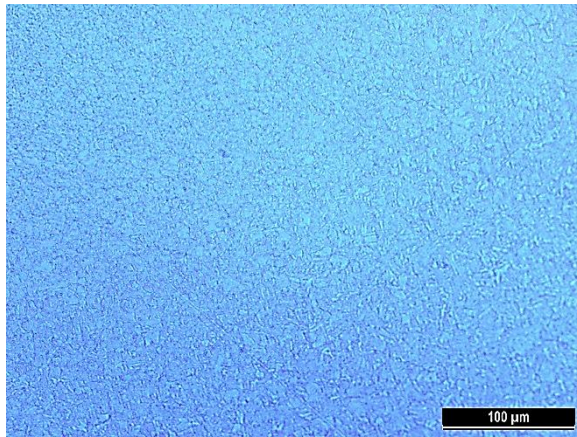
Figure 50: EU 97 after EE 10s (20x magnified)
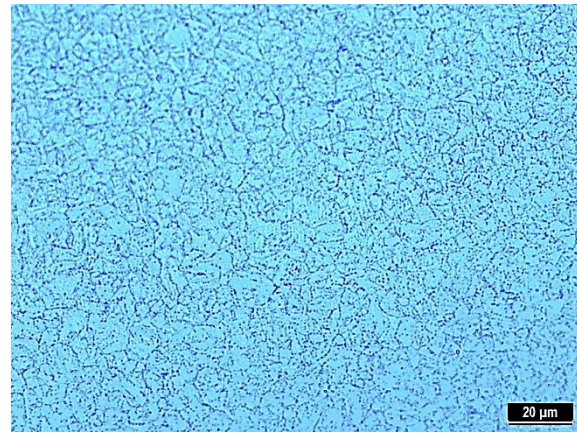
Figure 51: EU 97 after EE 10s (50x magnified)
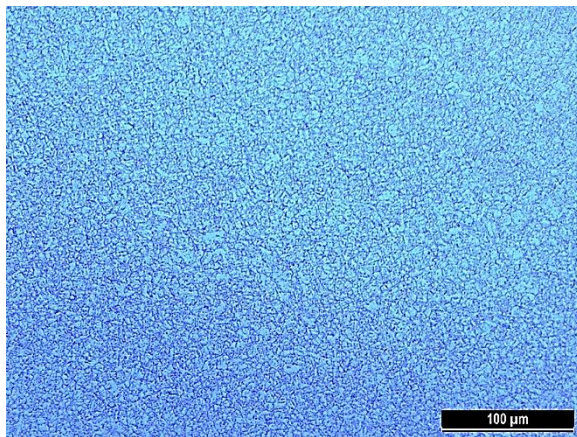
Figure 52: EU 97 after EE 20s (20x magnified)
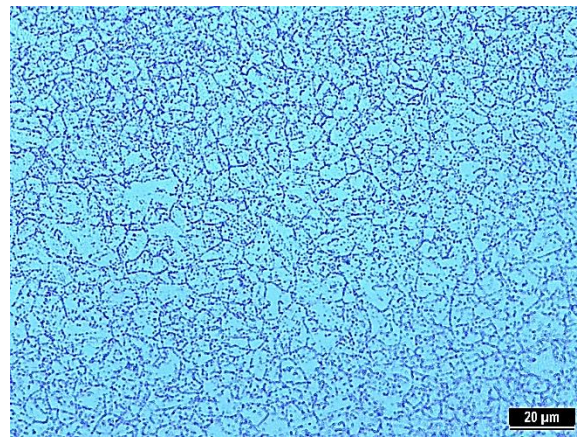
Figure 53: EU 97 after EE 20s (50x magnified)
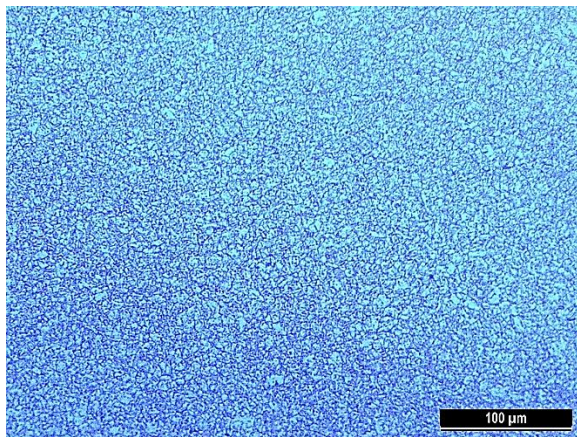
Figure 54: EU 97 after EE 30s (20x magnified)
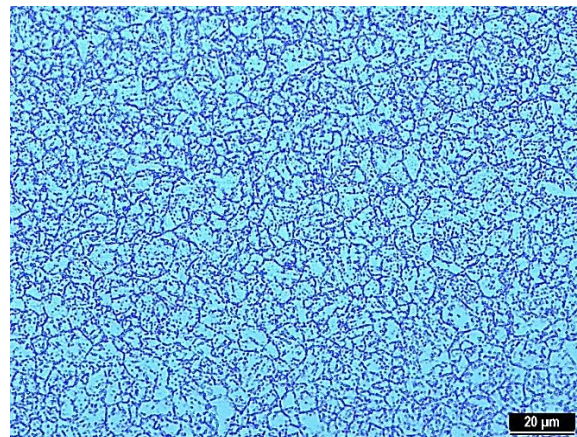
Figure 55: EU 97 after EE 30s (50x magnified)

Although it was intended to document each time the same area of sample surface, it was impossible to locate the exactly same place twice due to changes induced by polishing or etching procedures. As it can be seen, with each time step the structure was becoming clearer. After 30 seconds the surface structure visibility was considered as sufficient for the purposes

of the nanoindentation. Acquired images show the presence of ferritic (prior austenitic) grains together with martensitic grains. Prior austenitic grains are better visible on sample 2, while the needle shape martensitic grains can be observed on sample 1. This difference originates in manufacturing processes and it can also affect the material behaviour when subjected to deformations from diverse directions.

3.2.   Evaluation of SPM and AFM data

The contact microscopy was used to determine whether the surface quality corresponds to demands of nanoindentation (Ra < 30 nm). Outcomes of SPM and AFM scanning were evaluated in the Gwyddion software, which was developed by Czech Metrology Institute. Two values of surface roughness were calculated along two diagonal lines interlaced through each scanned area. This is in accordance with standard surface roughness measurement procedure that measures in one direction perpendicular to the traces after last grinding/polishing step. Because the last surface treatment was electro etching/polishing or OPS, which has no specific direction, two perpendicular measurement directions were chosen. The results were then averaged and compared in the table 8. Another reason for such measurement is the fact, that the dust particles inevitably settle on the sample surface and ostensibly increase its roughness.
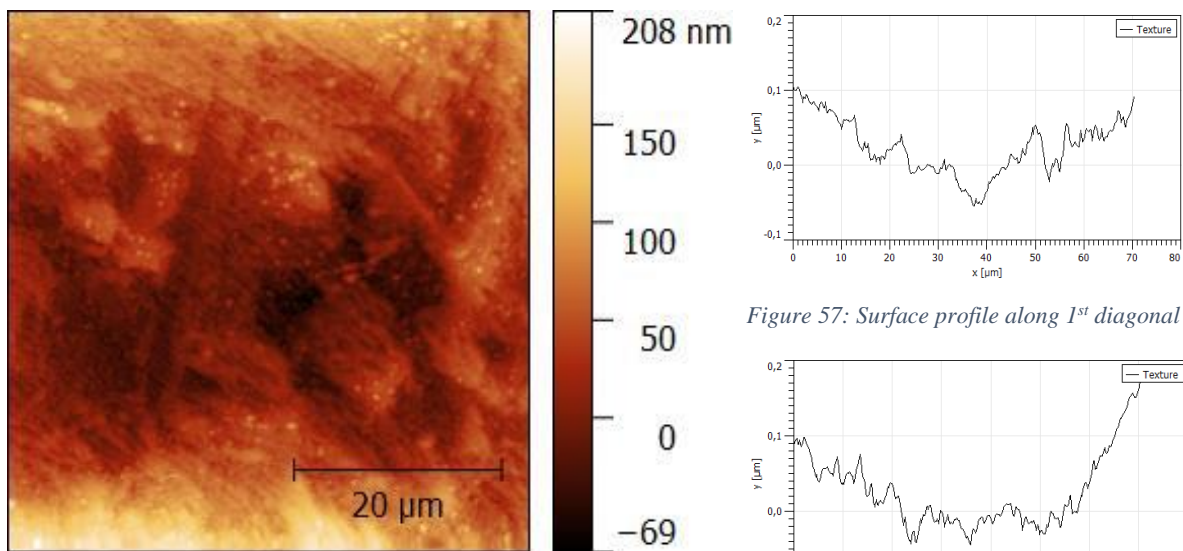
Figure 56: SPM scan of OPS area
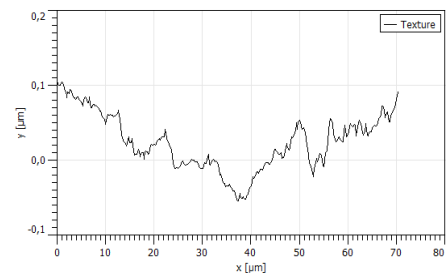
Figure 57: Surface profile along 1st diagonal
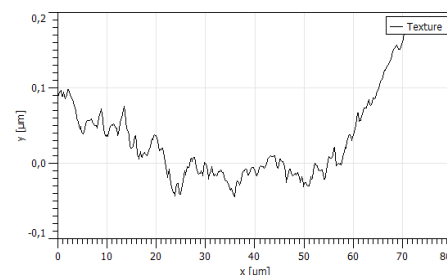
Figure 58: Surface profile along 2nd diagonal
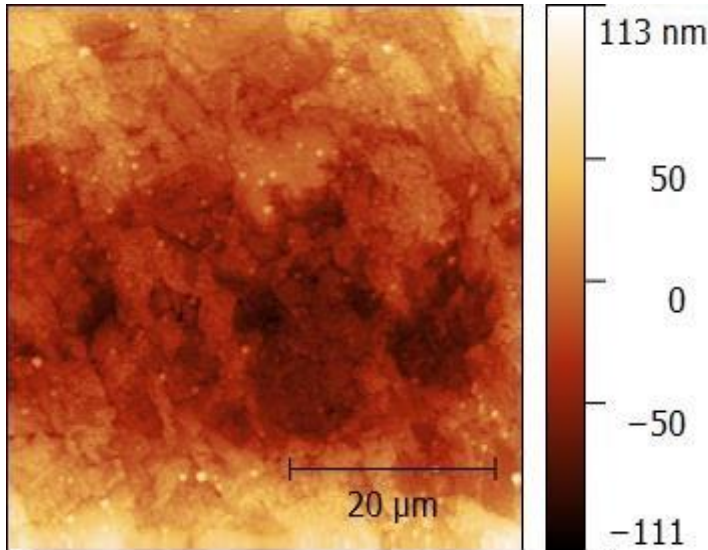
Figure 59: SPM scan of electro etched area
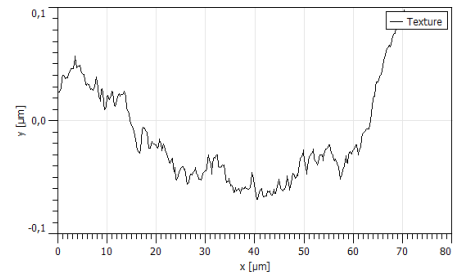
Figure 60: Surface profile along 1ˢᵗ diagonal
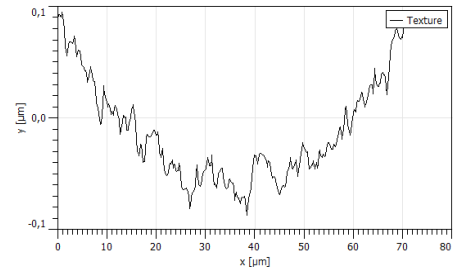
Figure 61: Surface profile along 2ⁿᵈ diagonal
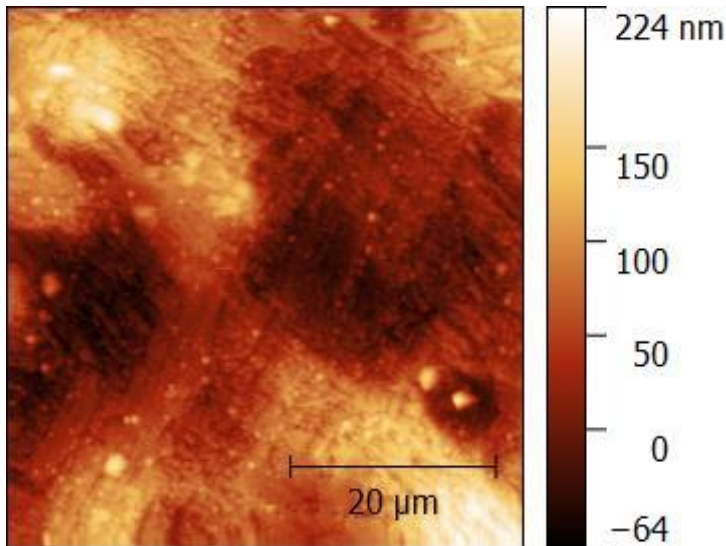
Figure 62: SPM scan of electro polished area
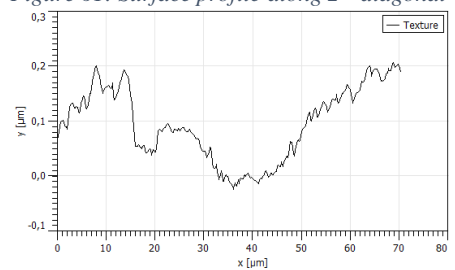
Figure 63: Surface profile along 1ˢᵗ diagonal
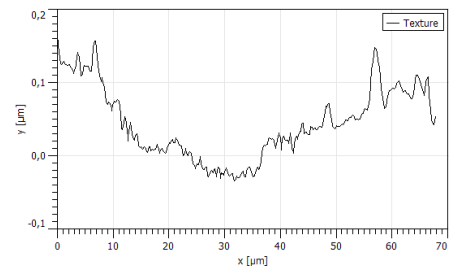
Figure 64: Surface profile along 2ⁿᵈ diagonal

Assessment of high-temperature micromechanical properties of ferritic-martensitic steels
by nanoindentation
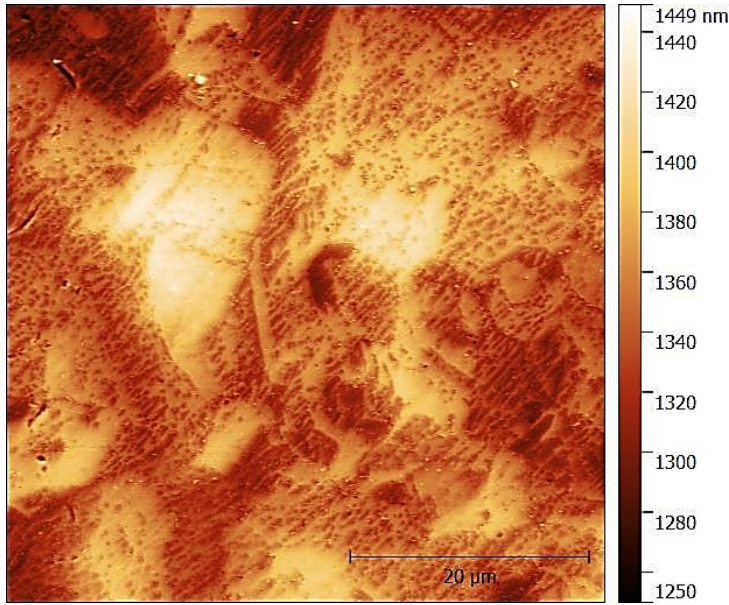
Figure 65: AFM scan of OPS area

Figure 68: AFM scan of electro etched area
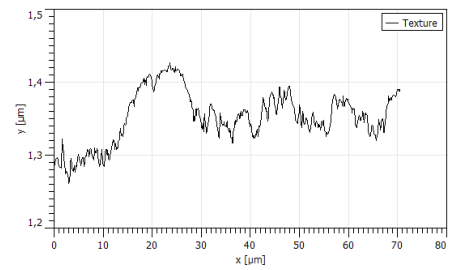
Figure 66: Surface profile along 1st diagonal
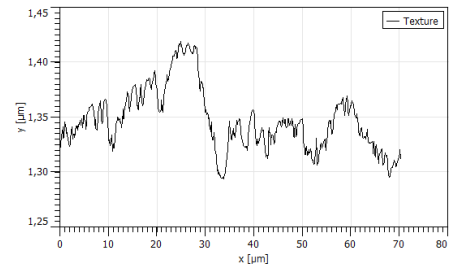
Figure 67: Surface profile along 2nd diagonal
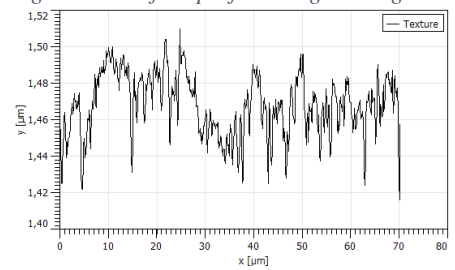
Figure 69: Surface profile along 1st diagonal
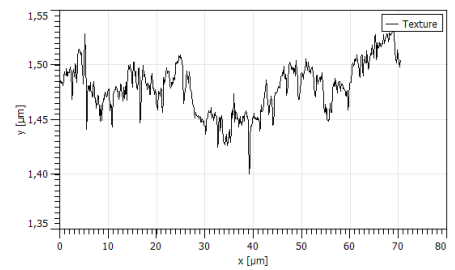
Figure 70: Surface profile along 2nd diagonal

Assessment of high-temperature micromechanical properties of ferritic-martensitic steels
by nanoindentation
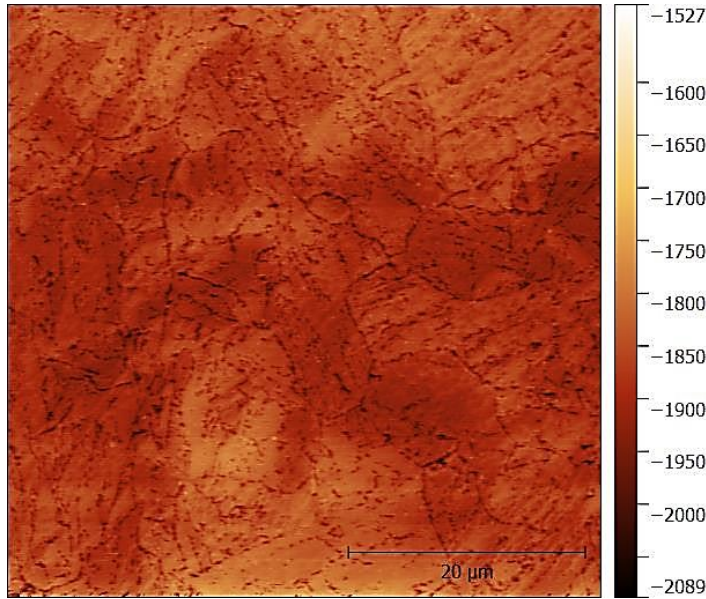
Figure 71: AFM scan of electro polished area
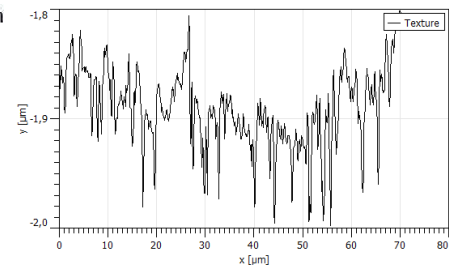
Figure 72: Surface profile along 1st diagonal
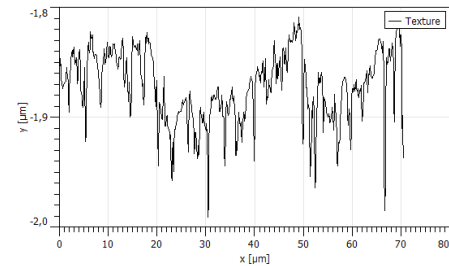
Figure 73: Surface profile along 2nd diagonal

	SPM Ra [nm]	AFM Ra [nm]
OPS	7	6.15
EE	7.95	7.5
EP	9.2	14.85

Table 8: Comparison of results from contact microscopy

Results from both methods of contact microscopy vary mostly because of different radii of AFM and SPM tips. The AFM tip has the radius of 2-12 nm, while the radius of SPM tip is around 100 nm. This corresponds to better resolution in case of AFM images as well as surface profile graphs. Sharper tip of the AFM allows to see the grains and grain boundaries, which is not possible in case of SPM tip. The table shows that the best value of average surface roughness is after OPS. This corresponds to the fact, that if the structure visibility is desired, the roughness must be aggravated. The highest value of average roughness in case of electro polished area might suggest that this method removes certain work hardening induced after the grinding and polishing procedures.

3.3. Scanning Electron Microscopy

Prior the EDX and EBSD analyses, electron images of sample surface were done using back-scattered and secondary electrons. Diverse electron spectra were selected due to a contrast difference. Secondary electrons show better the phase contrast, while back-scattered electrons better reveal the topography.
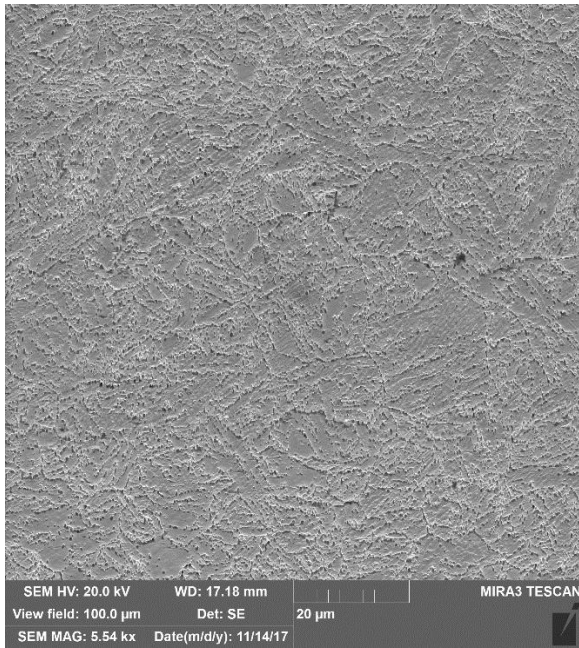
Figure 74: SEM image of EP area on sample 1 acquired by secondary electrons
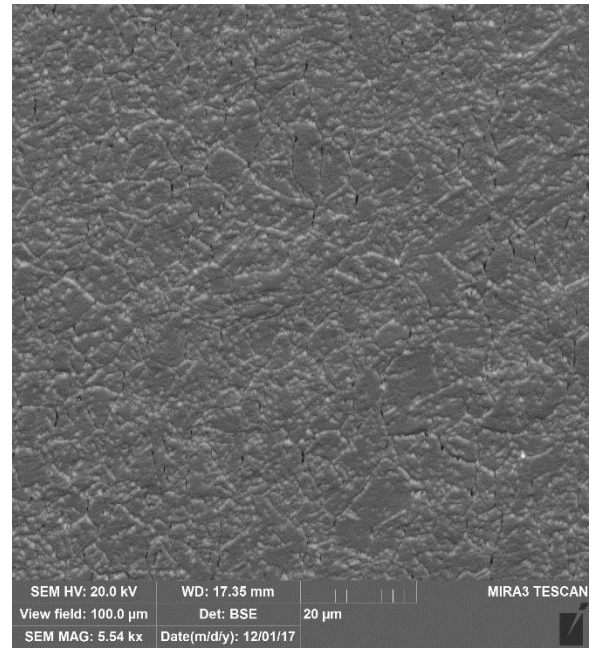
Figure 75: SEM image of EE area on sample 2 acquired by back-scattered electrons

3.3.1. EDX

Chemical composition of EUROFER 97 was already stated in theoretical part of this work (Table 5), so it can be compared with acquired data.

EUROFER 97 by EDX											
Element	Ni	Cr	Mo	Ta	V	W	Fe	Si	Mn	C	P	S
wt %	0.2	9.2	~ 0	0.5	0.2	1	86.1	~ 0	0.4	2.3	~ 0	~ 0

Table 9: Verification of EUROFER 97 chemical composition by EDX
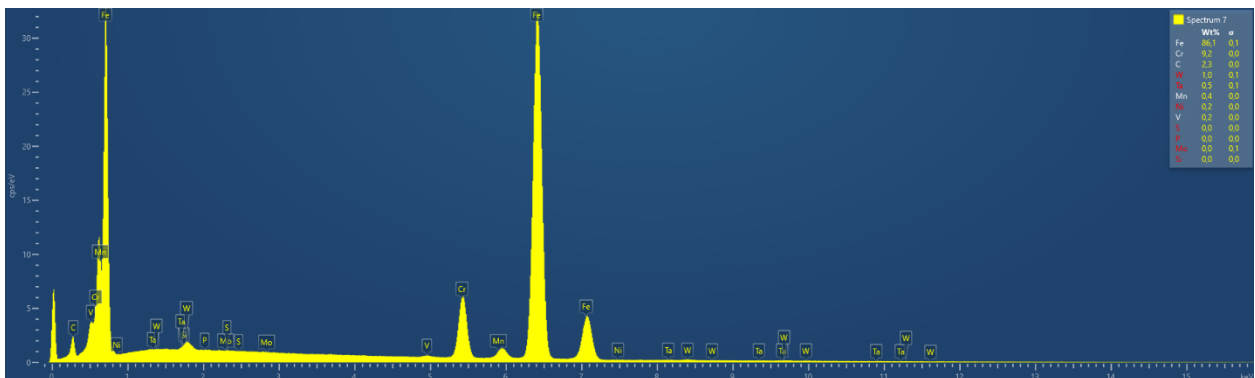
Figure 76: The spectrum of elements detected by EDX within EUROFER 97 sample

Assessment of high-temperature micromechanical properties of ferritic-martensitic steels by nanoindentation

The amount of C detected was most likely due to a diamond debris that sometimes get stuck in the sample surface after grinding and polishing procedures. Another reason could be the fact, that samples was rinsed in the isopropyl alcohol which contains carbon as well. Alcohol then creates maps even after the surface is dried. Although the amount of C has a certain effect on the concentrations of other elements, such tentative results are enough to verify the chemical composition claimed in the literature. Except C, the biggest deviations from the composition given in literature can be observed in case of Ni ($0.02 \rightarrow 0.2$) and Ta ($0.12 \rightarrow 0.5$). The chemical composition may also vary due to a size and location of analyzed area.
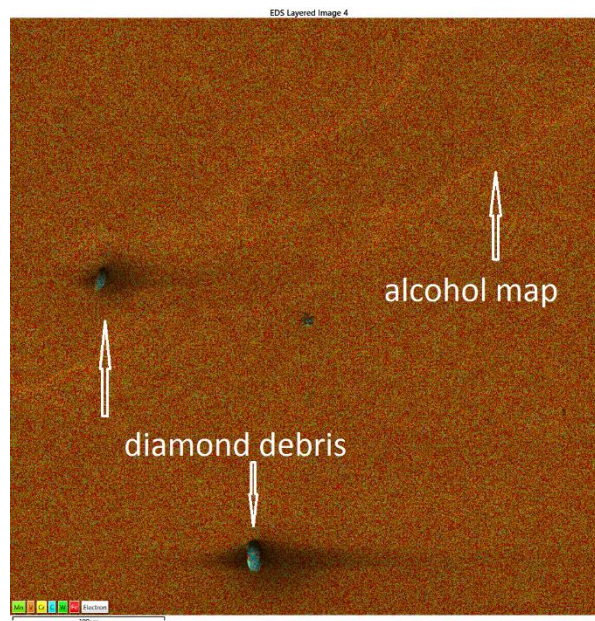
Figure 77: Electron image of the area of sample 1 scanned by EDX

3.3.2. EBSD

Phase distribution within each sample was determined by SEM in the figures 78 and 80. Body-centered tetragonal martensite has assigned a blue color, while the face-centered cubic structure of ferrite is colored in red. Images containing also the zero solutions (unidentified phases) were added for a comparison.
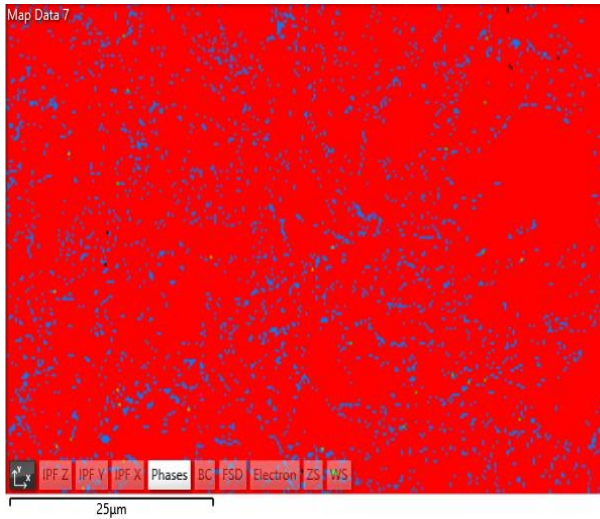
Figure 78: Distribution of martensite phase in sample 1
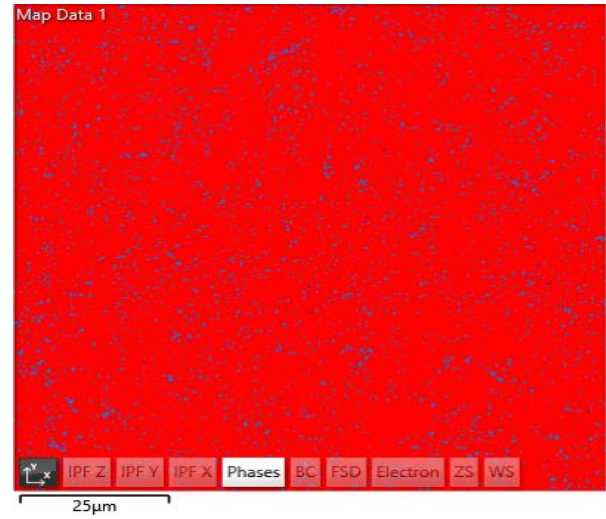
Figure 80: Distribution of martensite phase in sample 2
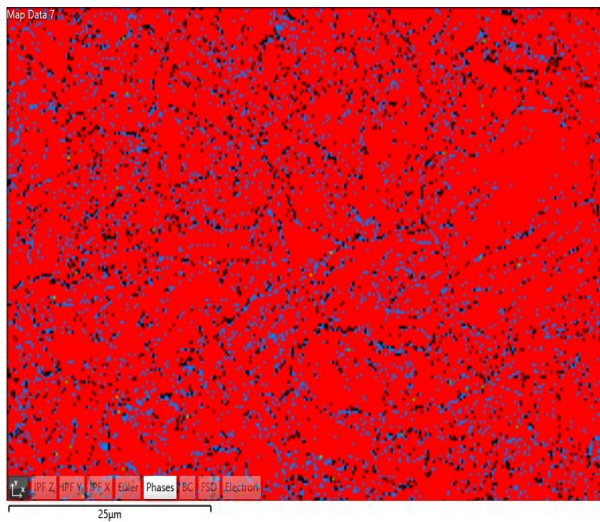
Figure 79: Distribution of martensite phase plus unidentified pahses in sample 1

Figure 81: Distribution of martensite phase plus unidentified phases in sample 2

The diffraction of Kikuchi patterns for body-centered cubic iron (ferritic or pre-austenitic phase) and tetragonal body-centered iron (martensite) are shown in figures 82 and 83 respectively.
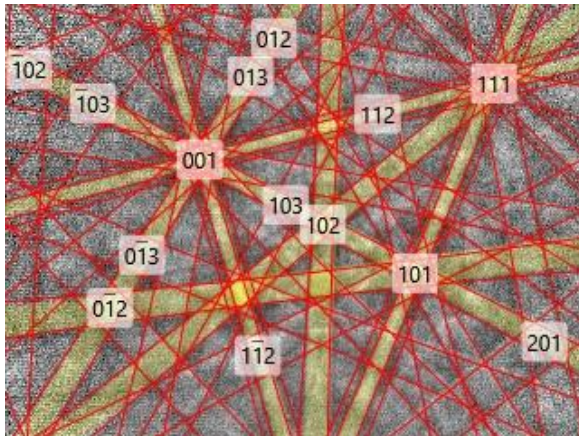
Figure 82: Diffraction of Kikuchi patterns for FCC iron grain
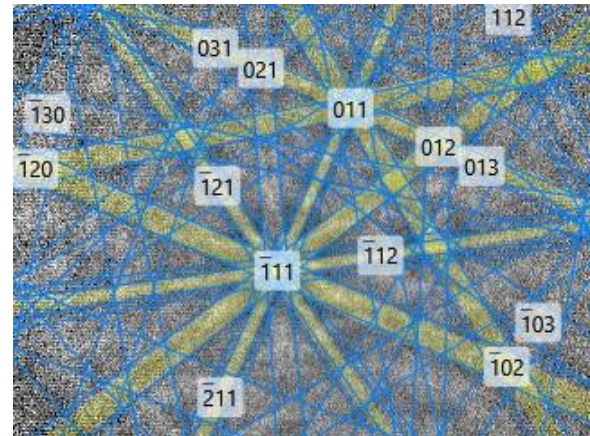
Figure 83: Diffraction of Kikuchi patterns for TBC iron grain

The grain structure and orientation are then visible on EBSD maps in figures 84 and 85, that are both associated with the legend attached underneath them. Ferritic grains are rather wider formations, while the martensite has needle shape grains. The orientation of ferritic and martensitic grains is described by shifted color coordinates in order to distinguish between both phases. The difference between both grain structures corresponds to the fact, that sample 2 was cut in a perpendicular plane to sample 1.
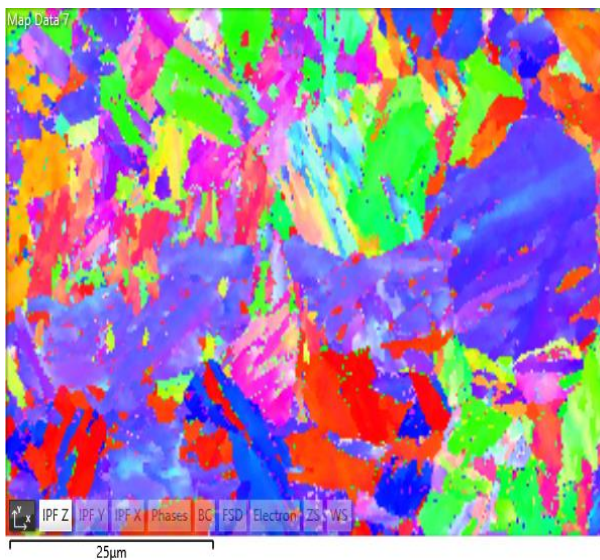
Figure 84: Grain structure and orientation map of sample 1
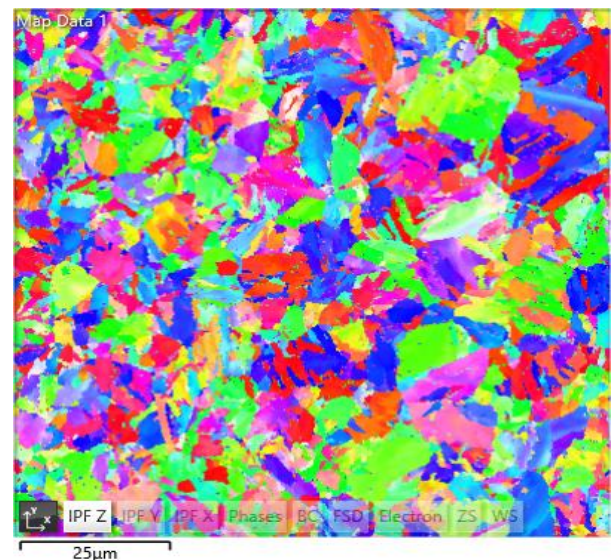
Figure 85: Grain structure and orientation map of sample 2
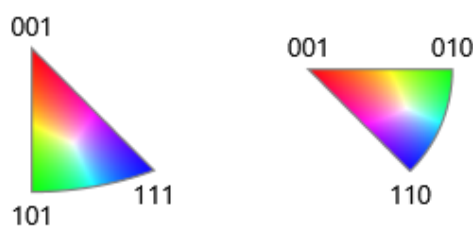
Figure 86: Orientation of FCC iron (left) and BCT iron (right)

3.4. Calibration

Capability of the xSol 800 heating stage to maintain desired temperature during the entire period of the nanoindentation was proved. Although the indentation matrix usually takes less than 6 hours, at high temperatures the total time increases due to thermal drift. The interval for maintaining the constant temperature was decided to be around 6 hours to make sure constant conditions will be kept during the entire measurement. The temperature stability is shown in figures 87 and 88. Maximal deviations from particular set point temperatures measured by thermocouples were:

- 100 ± 0,08 °C
- 300 ± 0,09 °C
- 500 ± 0,06 °C
- 700 ± 0,06 °C
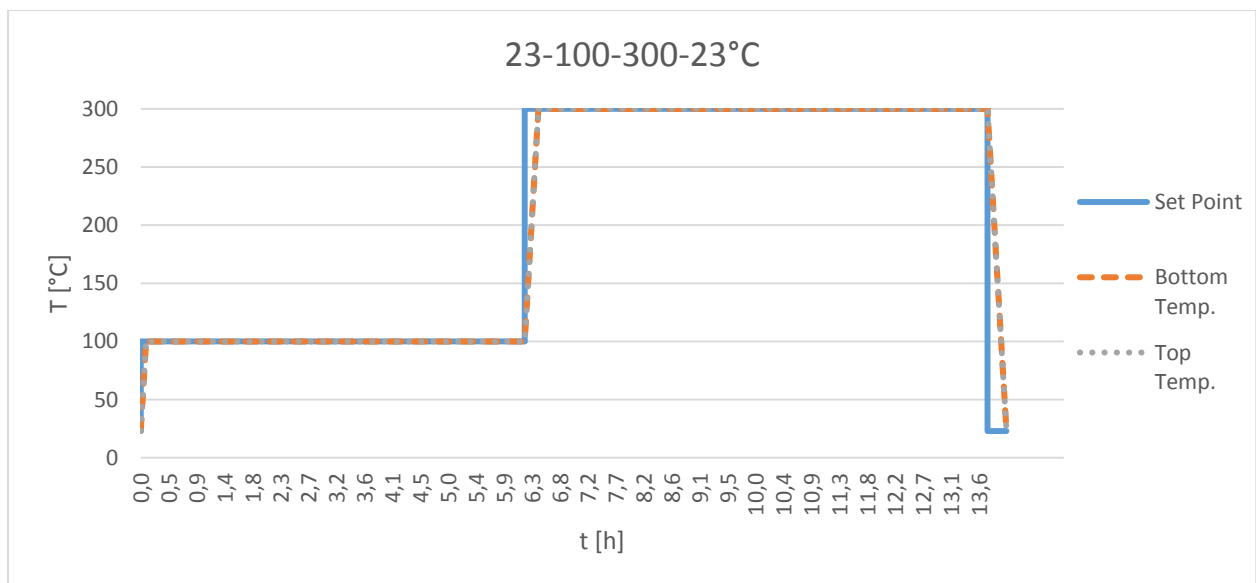
Figure 87: Graph of temperature stability for 100 and 300°C
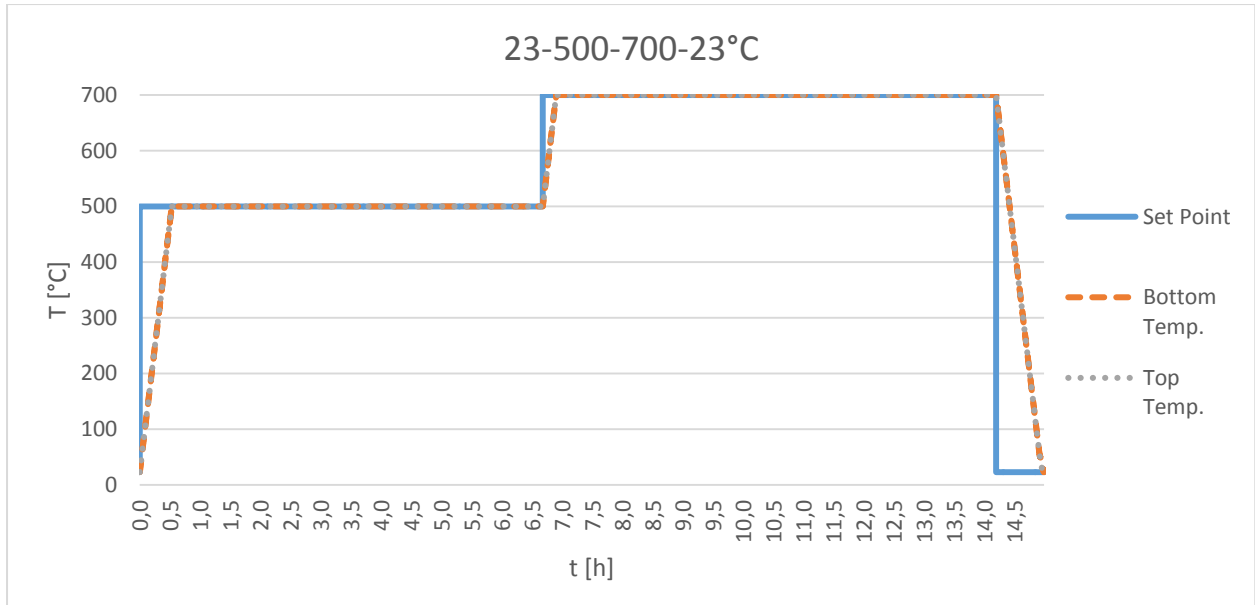
Figure 88: Graph of temperature stability for 500 and 700°C

In case of the high load head, the range of applied calibration loads was from 10 mN to 200 mN. For the standard load head the range of applied load from 1 mN to 10 mN was selected. Tip area functions obtained for Berkovich indenters of standard and high load head were calculated from indentation curves in figures 89 and 90.
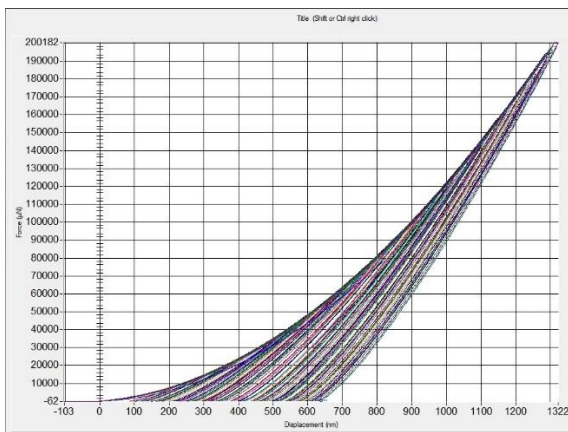
Figure 89: Tip area calibration curves fro high load tip
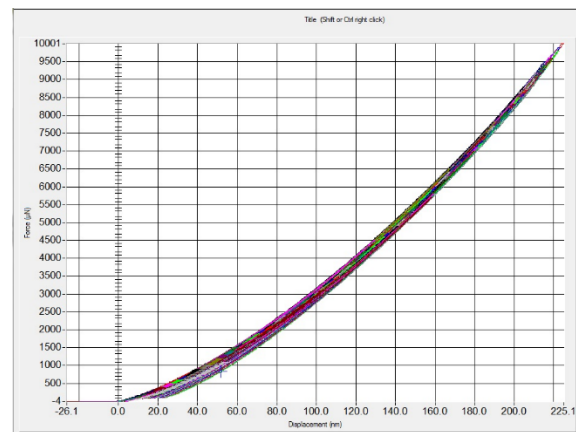
Figure 90:Tip area calibration curves fro standard tip

Unfortunately, the values of reduced modulus and hardness available for the fused quartz standard are only for room temperature. Therefore it must be assumed the frame stiffness remains unchanged within the range of all nanoindentation measurements.
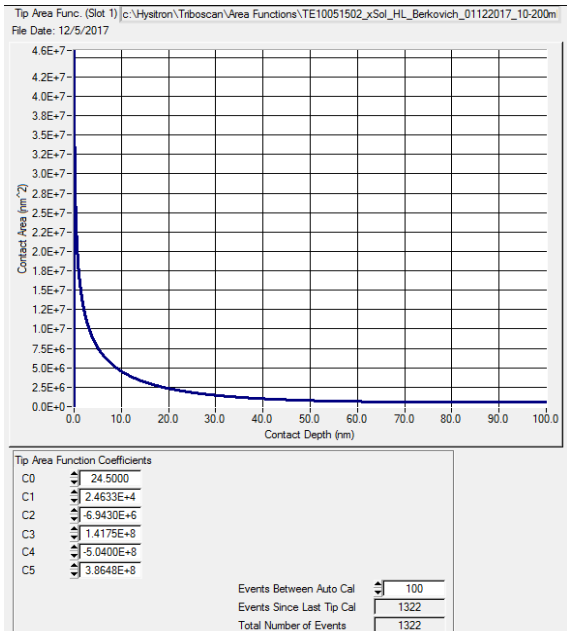
Figure 91: Calibrated tip area function of high load indenter
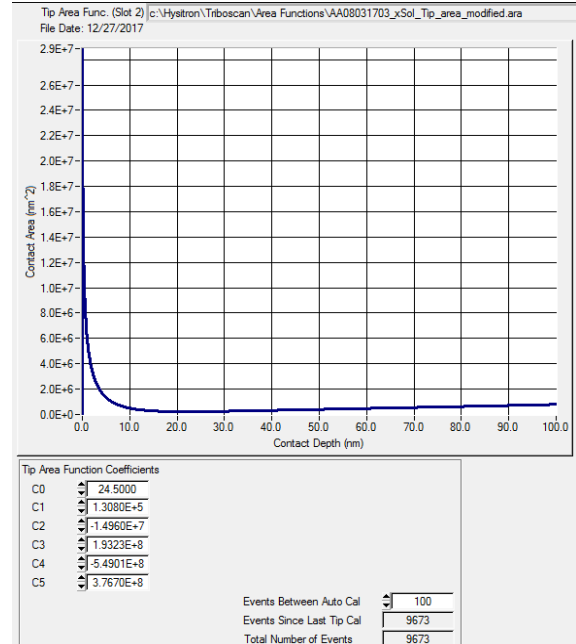
Figure 92: Tip area function used for standard load indenter

The machine compliance was determined as described in chapter 2.4.2. to the value of 1,32 nm/mN for high load head and 2,7 nm/mN for standard tip.

3.5.   Nanoindentation

Results of all measurements were calculated according to Oliver-Pharr method in TriboScan 9 software supplied with the TI 950 TriboIndenter. Remaining part of post-indentation analysis was done in Microsoft Excel and partially in MatLab. All conducted nanoindentation measurements are listed in table 10.

°C\mN	Electro polished area				Electro etched area				OPS area			
	5	10	50	100	5	10	50	100	5	10	50	100
23°C	✓	✓	✓	✓	✓	✓	✓	✓	✓	✓	✓	✗
100°C	✓	-	✓	-	✓	-	-	✓	✓	-	-	-
200°C	-	-	✓	-	-	-	-	✓	-	-	-	-
300°C	✓	-	✓	-	✓	-	-	✓	✓	-	-	-
500°C	✓	-	-	-	✓	-	-	-	✓	-	-	-
700°C	-	-	-	-	-	-	-	-	✓	-	-	-

Table 10: List of nanoindentation tests (✓ done, ✗ distorted, - not conducted)

Assessment of high-temperature micromechanical properties of ferritic-martensitic steels
by nanoindentation

To be able to compare the measured values of reduced modulus with the data from literature, the Young's modulus shown in table 6 (E = 213 GPa) was recalculated on reduced modulus for each tip using the eq. 9. The poison's ratios $v_i = 0.07$ for a diamond tip and and the $v_i = 0.29$ for a sapphire tip were used. The $v = 0.3$ was assumed for the EUROFER 97. Young's modulus of the diamond tip is $E_i = 1140$ GPa and for the sapphire tip the $E_i = 345$ GPa. Calculated values of reduced modulus for room temperature are shown in the table 11.

	Diamond tip (10, 50 and 100 mN)	Sapphire tip (5 mN)
E_{eff} [GPa]	194	144

Table 11: Values of Young's modulus recalculated from reduced modulus obtained by 100 mN indents

3.5.1. Room Temperature Nanoindentation

Hardness and reduced modulus were plotted as a function of load and contact depth for all three indented areas. The thermal drift was also analyzed and compared among all loads within one area.

Electro polished area
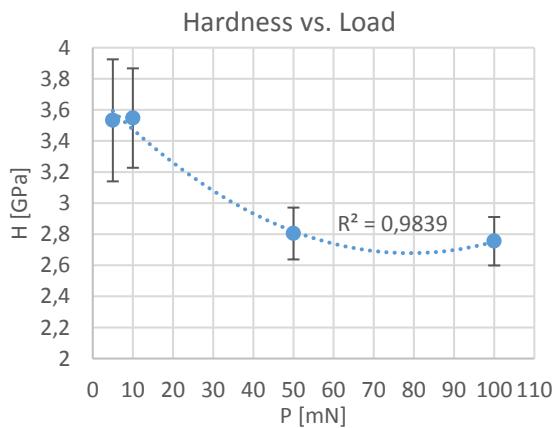
Figure 93: Graph of H = f(P) for EP area at RT
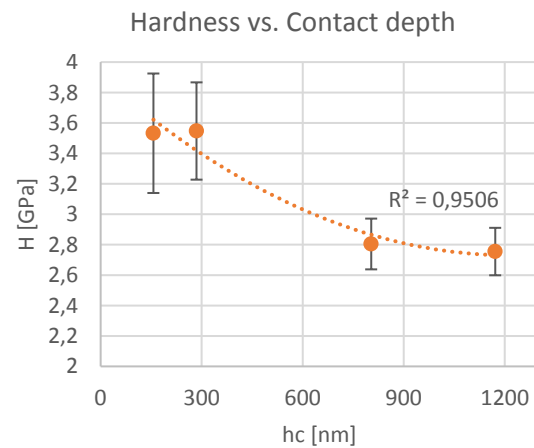
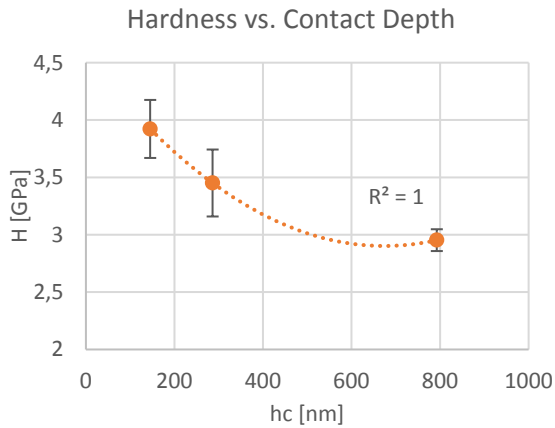*Figure 94: Graph of H = f(h_c) for EP area at RT*
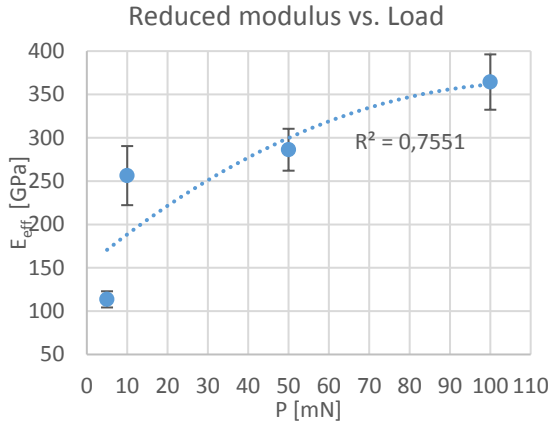
Figure 95: Graph of E$_{eff}$ = f(P) for EP area at RT
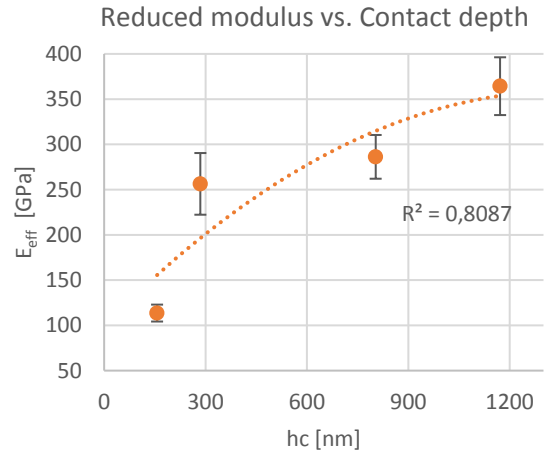
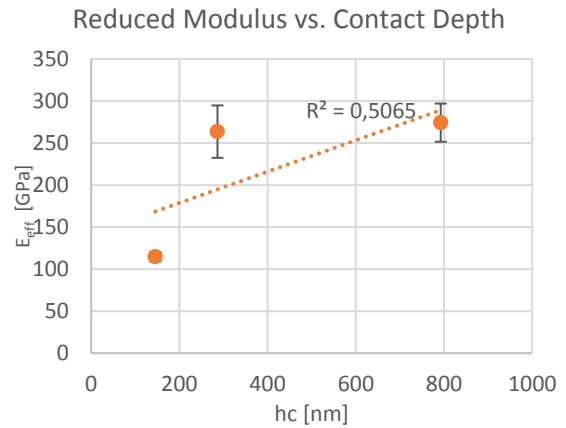*Figure 96: Graph of Eeff = f(h$_c$) for EP area at RT*
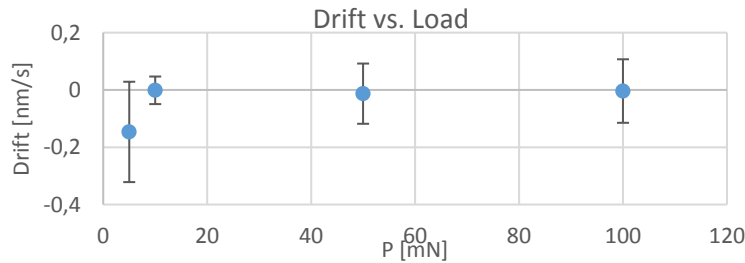
Figure 97: Graph of indenter thermal drift on EP area for all loads at RT

From these results, it is apparent, that the hardness is decreasing with increasing load or contact depth, while the reduced modulus shows exactly opposite trend. This might be due to an ISE. The deviations of hardness values are generally lower for higher loads. In case of reduced modulus, the deviations are minimal for 5 mN indents and almost constant for remaining loads. The thermal drift was considered as acceptable.

Electro etched area
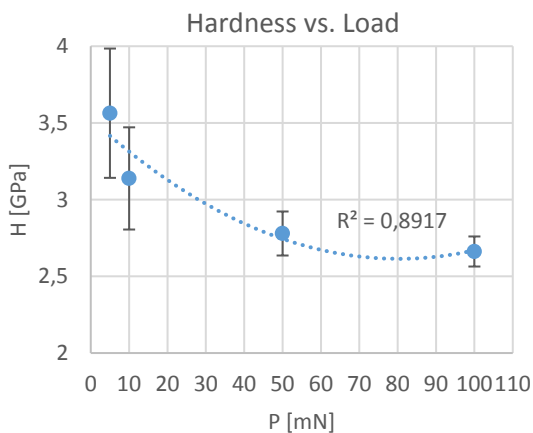
Figure 98: Graph of H = f(P) for EE area at RT
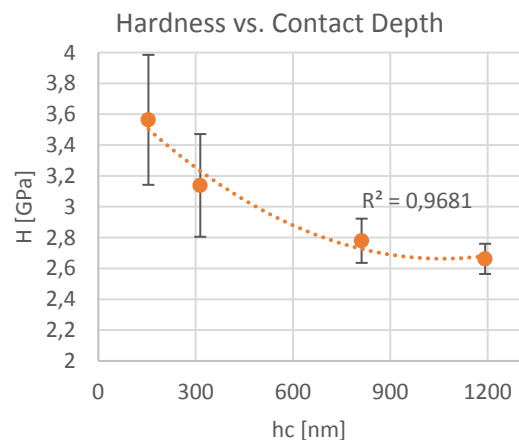
Figure 99: Graph of H = f(h$_c$) for EE area at RT
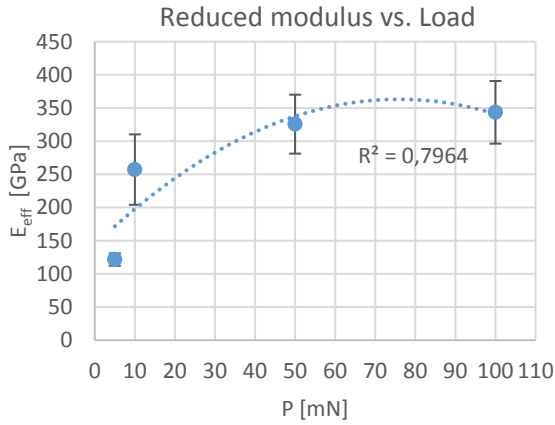
Figure 100: Graph of Eeff = f(P) for EE area at RT
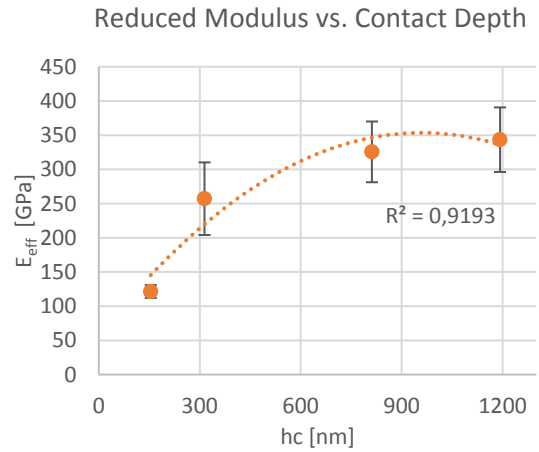
Figure 101: Graph of Eeff = f(h$_c$) for EE area at RT
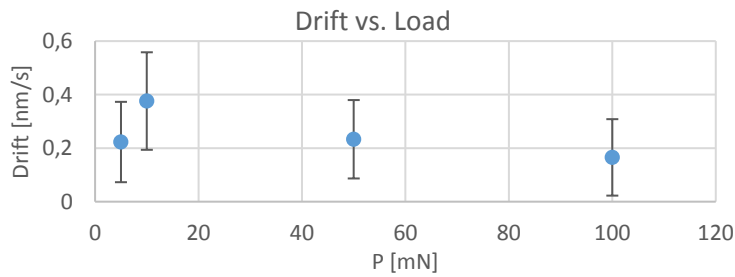
Figure 102: Graph of indenter thermal drift on EE area for all loads at RT

Similarly to EP area, the hardness is decreasing with increasing load or contact depth, while the reduced modulus shows exactly opposite trend. The deviations of hardness values are generally lower for higher loads. In case of reduced modulus, the deviations are minimal for 5 mN indents and almost constant for remaining loads. The thermal drift was greater than on previous area, but it was still considered as acceptable.

OPS area
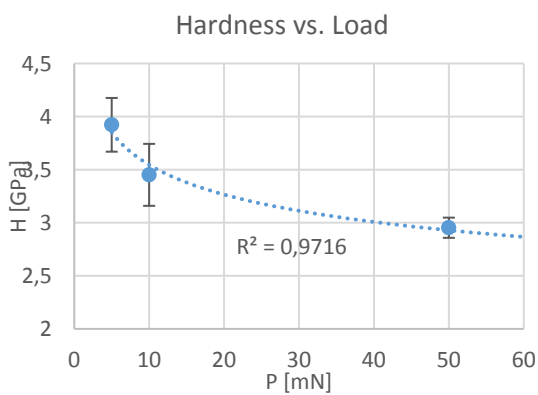
Figure 103: Graph of H = f(P) for OPS area at RT
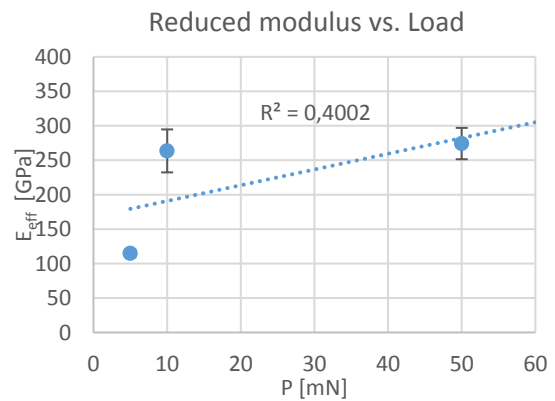
Figure 104: Graph of Eeff = f(P) for OPS area at RT

Hardness vs. Contact Depth

Figure 105: Graph of H = f(h_c) for OPS area at RT

Reduced Modulus vs. Contact Depth

Figure 106: Graph of Eeff = f(h_c) for OPS area at RT

Drift vs. Load
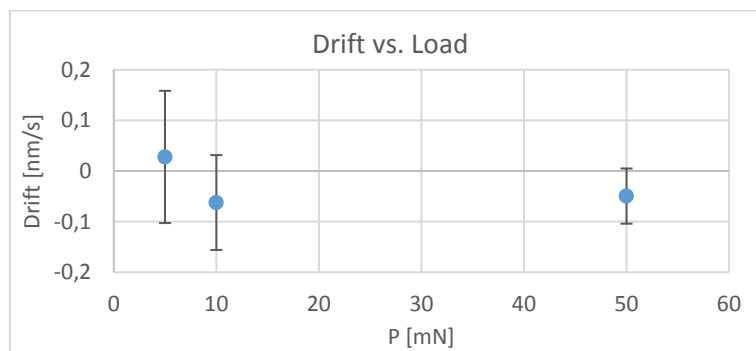
Figure 107: Graph of indenter thermal drift on OPS area for 5, 10 and 50 mN at RT

On the contrary to both preceding areas, the results from OPS are missing the values from 100 mN indentations. The measurement was conducted, but results got distorted and could not be involved in the analysis. An unknown error occurred during one of the final 50 mN indentations, which is observable in figure 137. Measurements were set up in series which caused the distortion of subsequent 100 mN indentations. Otherwise the hardness and reduced modulus show same trends as before. The thermal drift was minimal for all measurements.

As it can be observed, the reduced modulus shows an increasing trend with the increase of the indentation depth for all three areas of nanoindentation. The growth of reduced modulus seems to level up for higher indentation loads.

3.5.2. High-temperature nanoindentation

In this chapter, the data are again divided into three different sets corresponding to specific areas within the sample. Each set, except the OPS, contains two parts – the first is standard load and the second is high load nanoindentation. Hardness and reduced modulus were plotted

as functions of temperature for each load. Number of high-temperature high load indentations was reduced due to reasons stated in experimentation part.

3.5.2.1. *Standard load nanoindentation*

Electro polished area
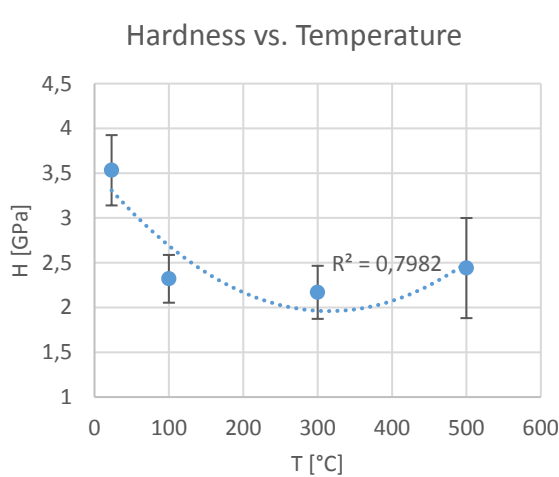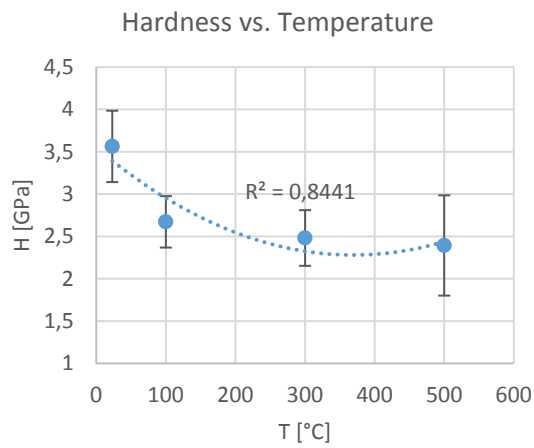

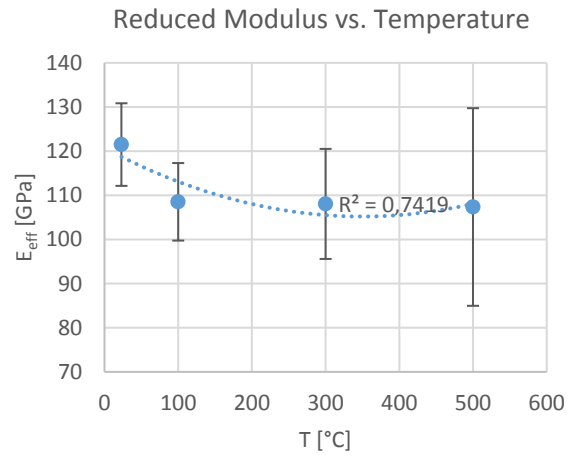Figure 108: Graph of H = f(T), T = 23 ÷ 500 °C for 5 mN indents on EP area
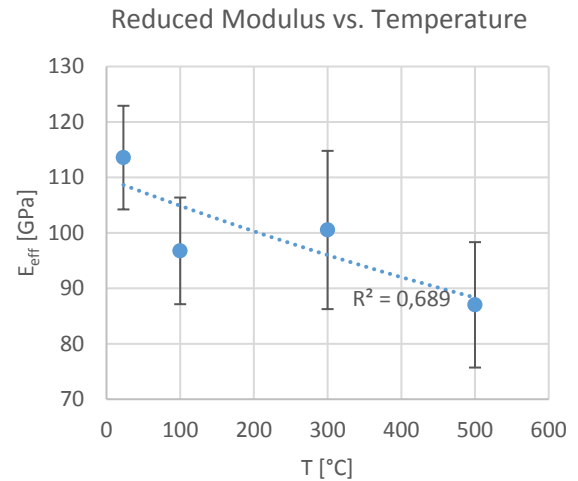
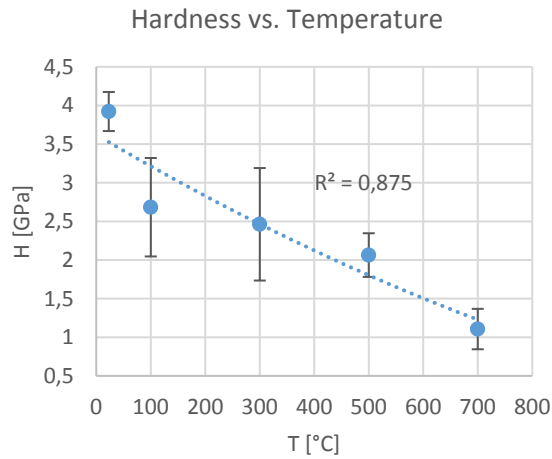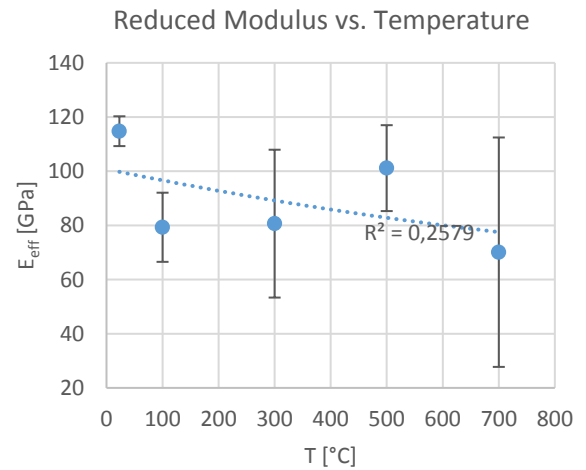Figure 109: Graph of E_{eff} = f(T), T = 23 ÷ 500 °C for 5 mN indents on EP area
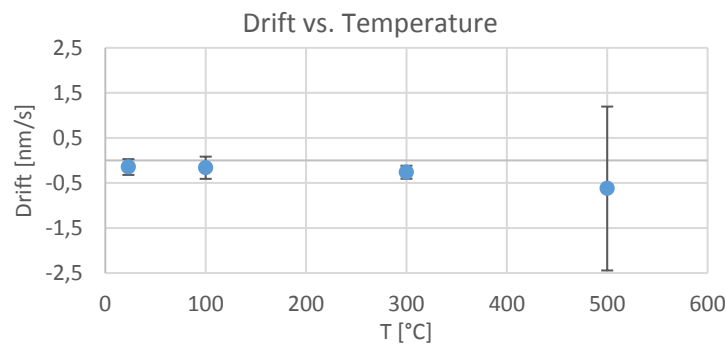
Figure 110: Thermal drift of standard tip on EP area at T = 23 ÷ 500 °C

Due to lower measurement precision at 500°C the results seem to show increasing values of hardness for this temperature. Hardness trend therefore do not correspond to the reality, but the reduced modulus seems to develop as expected. Apart from the measurement at 500°C, the thermal drift was minimal.

Electro etched area

Hardness vs. Temperature

R² = 0,8441

Figure 111: Graph of H = f(T), T = 23 ÷ 500 °C for 5 mN indents on EE area

Reduced Modulus vs. Temperature

R² = 0,7419

Figure 112: Graph of E$_{eff}$ = f(T), T = 23 ÷ 500 °C for 5 mN indents on EE area

Drift vs. Temperature
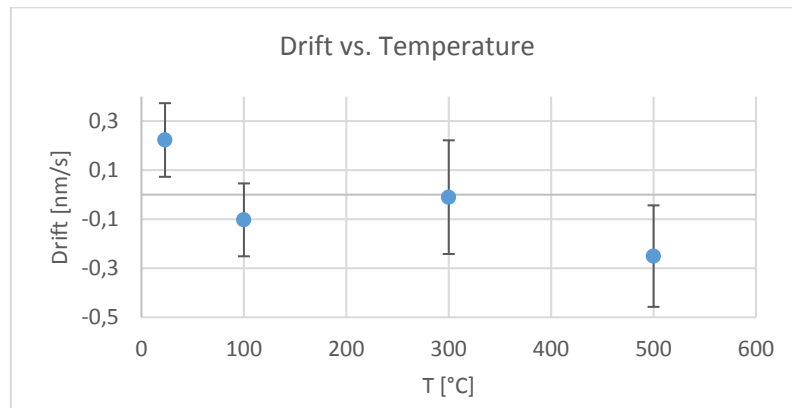
Figure 113: Thermal drift of standard tip on EE area at T = 23 ÷ 500 °C

Hardness and reduced modulus both show generally decreasing trend, even though the precision of indentation at 500°C is again significantly larger than in other cases. The thermal drift is slightly larger, but still acceptable.

OPS area

Hardness vs. Temperature

R² = 0,875

Figure 114: Graph of H = f(T), T = 23 ÷ 700 °C for 5 mN indents on OPS area

Reduced Modulus vs. Temperature

R² = 0,2579

Figure 115: Graph of E_{eff} = f(T), T = 23 ÷ 700 °C for 5 mN indents on OPS area

Drift vs. Temperature
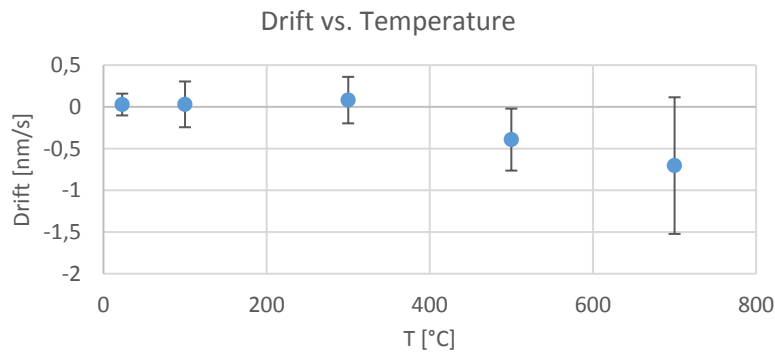
Figure 116: Thermal drift of standard tip on OPS area at T = 23 ÷ 700 °C

The nanoindentation on OPS area at 100 and 300°C was affected by preceding measurements at 700°C. Although the inert atmosphere should prevent surface oxidation, some degradation has occurred, which is going to be closer discussed in the chapter 3.5.3. Although the standard deviation for values of indents done at 700°C is very large, this data supplement the entire data set and confirm the decreasing trend of modulus changing with temperature. Large standard deviation was probably caused by higher thermal drift, which might be seen in preceding graph.

3.5.2.2.   High load nanoindentation

Electro polished area
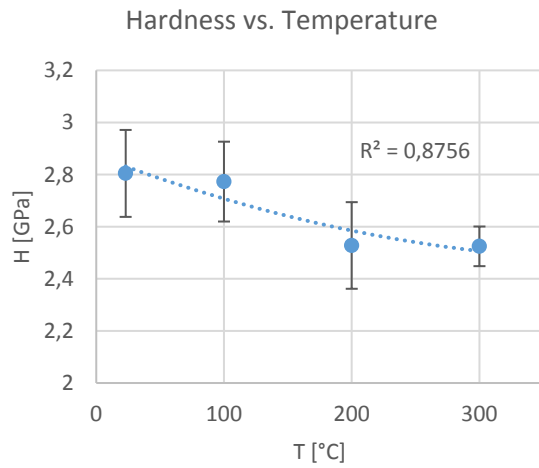
Figure 117: Graph of H = f(T), T = 23 ÷ 300 °C for 50 mN indents on EP area
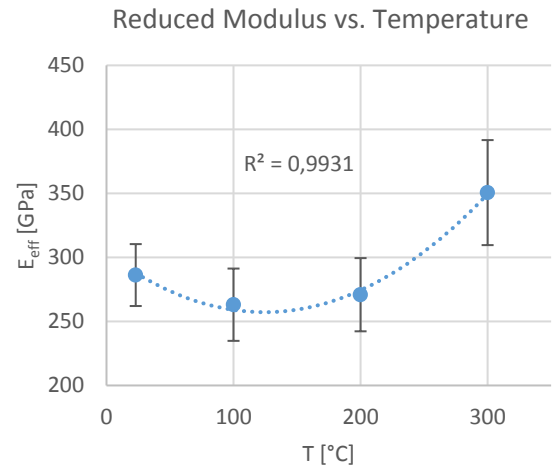
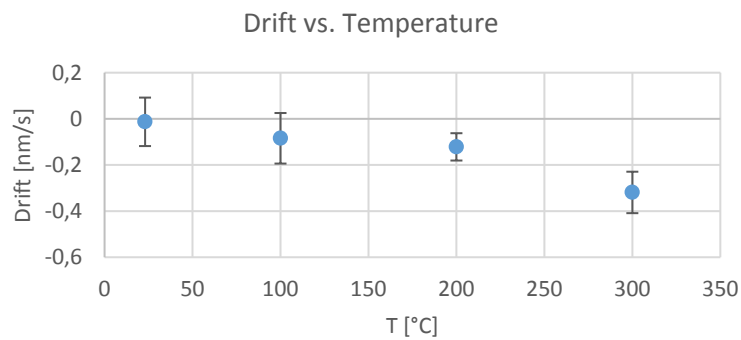Figure 118: Graph of Eeff = f(T), T = 23 ÷ 300 °C for 50 mN indents on EP area

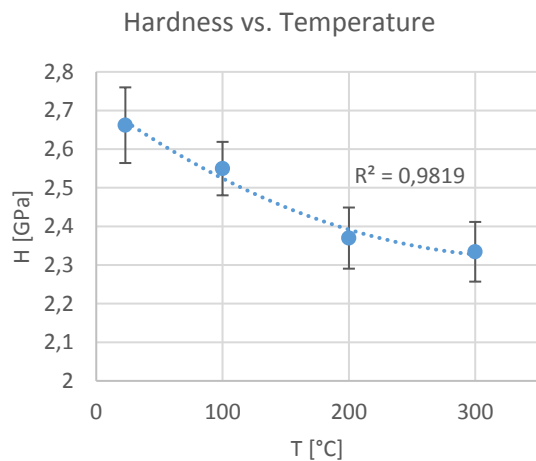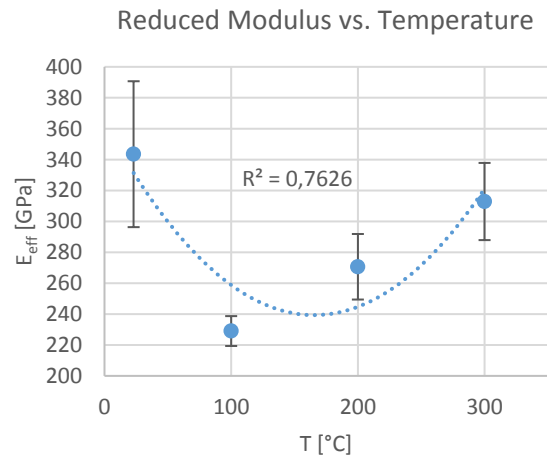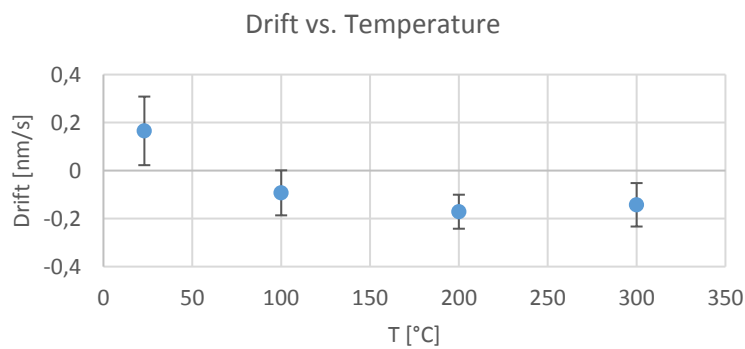Figure 119: Thermal drift of high load tip on EP area at T = 23 ÷ 300 °C

Electro etched area

Hardness vs. Temperature

$R^2 = 0,9819$

Figure 120: Graph of H = f(T), T = 23 ÷ 300 °C for 100 mN indents on EE area

Reduced Modulus vs. Temperature

$R^2 = 0,7626$

Figure 121: Graph of E$_{eff}$ = f(T), T = 23 ÷ 300 °C for 100 mN indents on EE area

Drift vs. Temperature

Figure 122: Thermal drift of high load tip on EE area at T = 23 ÷ 300 °C

During high load nanoindentation at high temperatures, the hardness is decreasing, but the modulus shows different behaviour for 50 and 100 mN loading than for 5 mN loading. This behaviour should be further investigated and more indentations should be made under similar conditions in future.

3.5.3. Post indentation analysis

The post indentation analysis was done using the LOM, AFM and SEM techniques. LOM was used for an optical check of the indents immediately after the nanoindentation finished. Load depth curves have been reviewed and in case of some abnormalities the indent was found in the matrix and opticaly evaluated. If the tip was damaged or in contact with some dust particle, the geometry of the indent would be changed. In-situ LOM post indentation analysis is more suitable for high load indents, as they are more visible by the optical head installed on TI 950.

It was also supposed that 5 mN indents will have much less probability of mutual affection than high load indents.
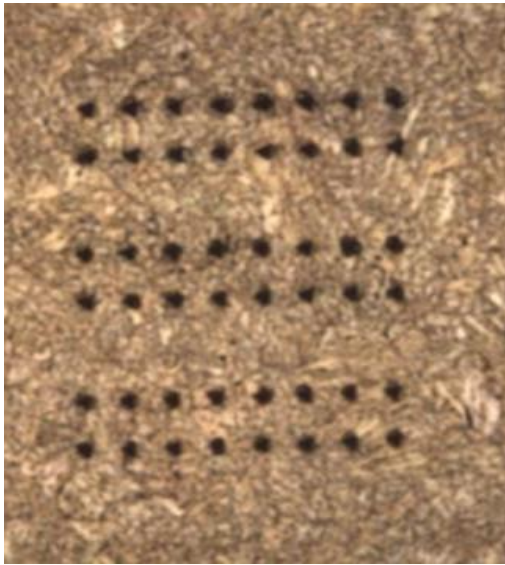

Figure 123: Post indentation in-situ LOM image (20x magnification) of 50 mN indents conducted at 100 (bottom), 200 and 300°C on EP area
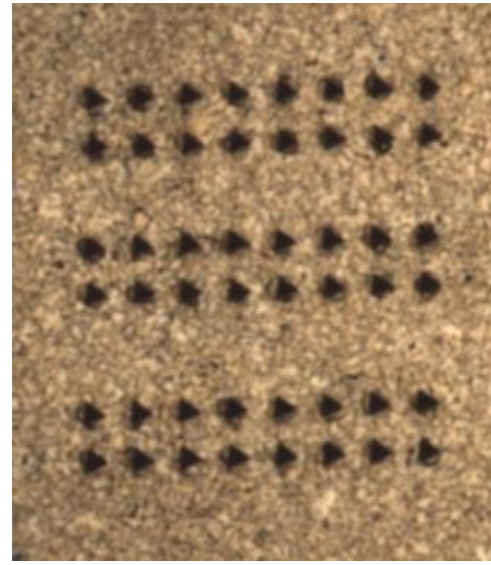

Figure 124: Post indentation in-situ LOM image (20x magnification) of 100 mN indents conducted at 100 (bottom), 200 and 300°C on EE area

Because of the size of high load indents and selected spacing in between them (20 µm), it was decided to carry out the AFM analysis as well in order to determine whether the pile up does not affect neighbouring indents. AFM scans were done on indents at 100 and 300°C to be able to compare the pile up.
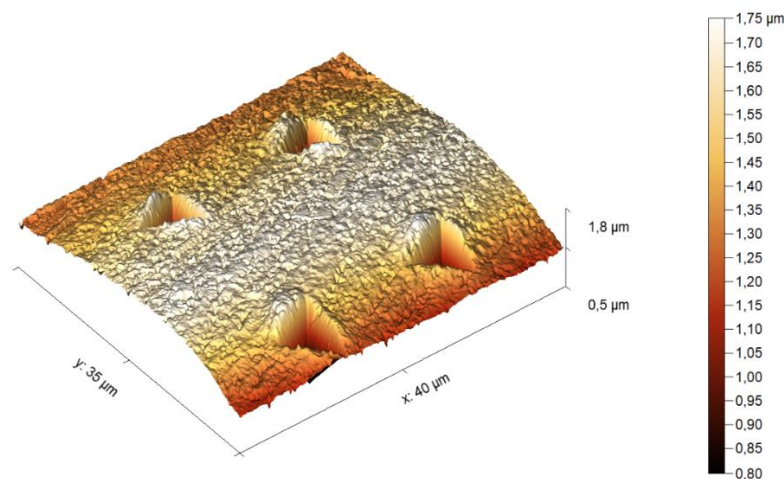

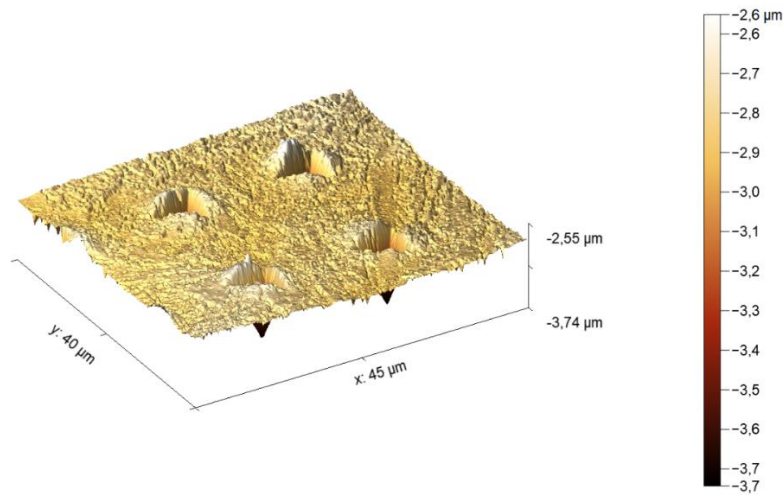*Figure 125: Post indentation topographic profile of 50 mN indents on EP area conducted at 100°C*

Figure 126: Post indentation topographic profile of 50 mN indents on EP area conducted at 300°C
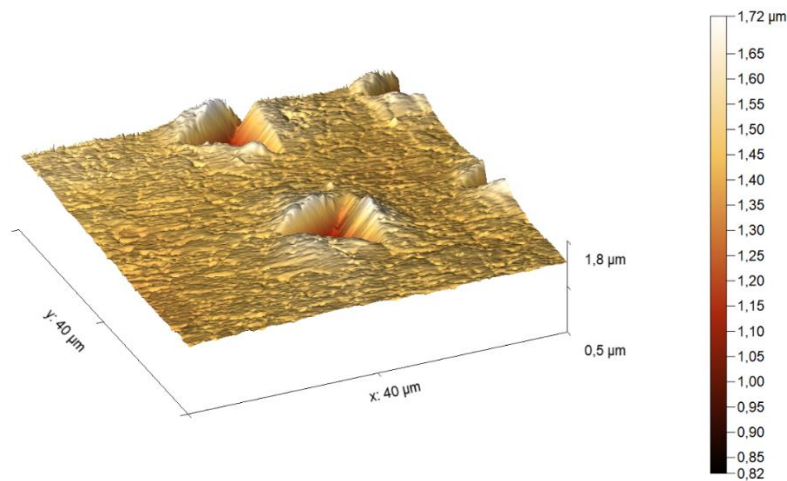

Figure 127: Post indentation topographic profile of 100 mN indents on EE area conducted at 300°C

Because of limited time given for AFM analysis, only the 100 mN indents done at 300°C were scanned. Both, optical and contact microscopy analysis, did not reveal the pile-up to have any influences on surrounding indents, but its existence suggests the need to compensate it in the calculation of results.

Finally, the EDX analysis was done on both samples to evaluate the extent of changes in chemical composition induced by high-temperature testing.
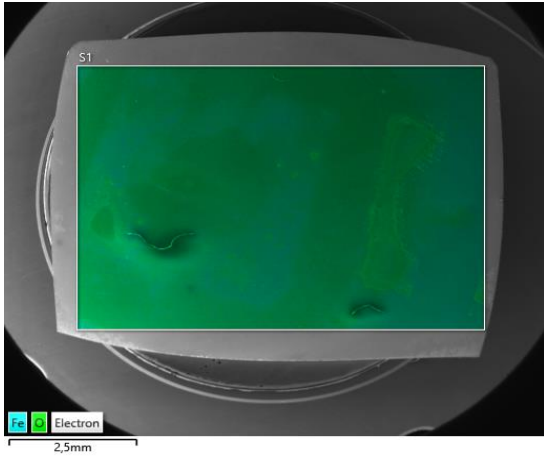
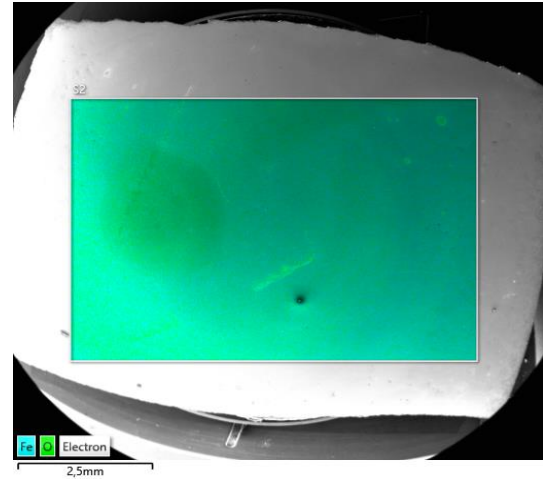*Figure 128: Map of chemical composition analyzed by EDX on sample 1*

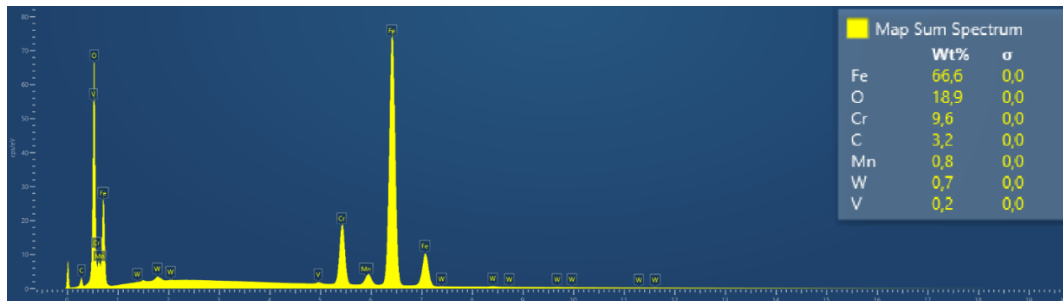*Figure 129: Map of chemical composition analyzed by EDX on sample 2*

Map Sum Spectrum		
	Wt%	σ
Fe	66,6	0,0
O	18,9	0,0
Cr	9,6	0,0
C	3,2	0,0
Mn	0,8	0,0
W	0,7	0,0
V	0,2	0,0

Figure 130: Spectrum acquired by EDX on sample 1

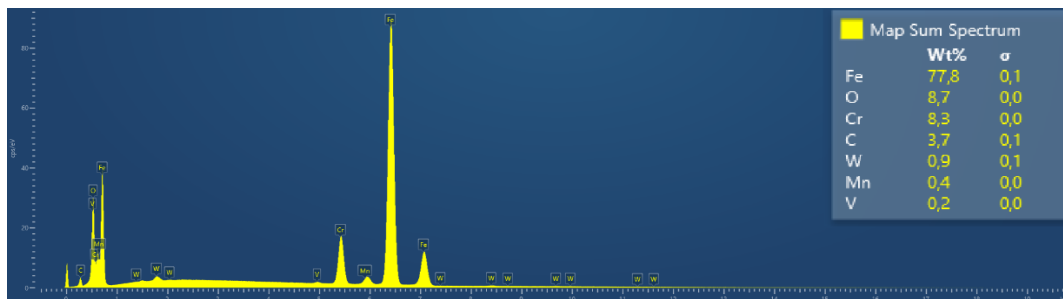| Map Sum Spectrum		
	Wt%	σ
Fe	77,8	0,1
O	8,7	0,0
Cr	8,3	0,0
C	3,7	0,1
W	0,9	0,1
Mn	0,4	0,0
V	0,2	0,0

Figure 131: Spectrum acquired by EDX on sample 1

According to the amount of oxygen present on both surfaces it is certain, that the oxidation occurred on both samples. The percentage of oxygen is greater at sample 1, which was exposed to temperature of 700°C. Sample 2 was heated only up to 500°C, therefore the extent of oxidation is lower. Oxide formations on both samples were documented by SE images shown below.
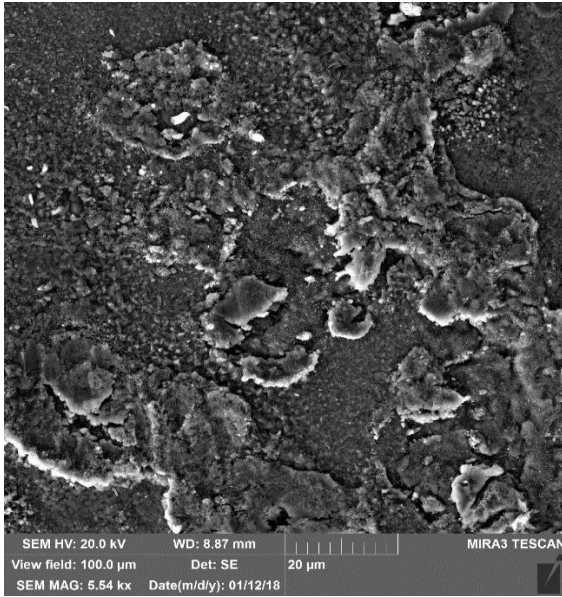
Figure 132: SEM secondary electron image of oxides created on the surface of sample 1 after heating up to 700°C (magnitude 5,54 kx)
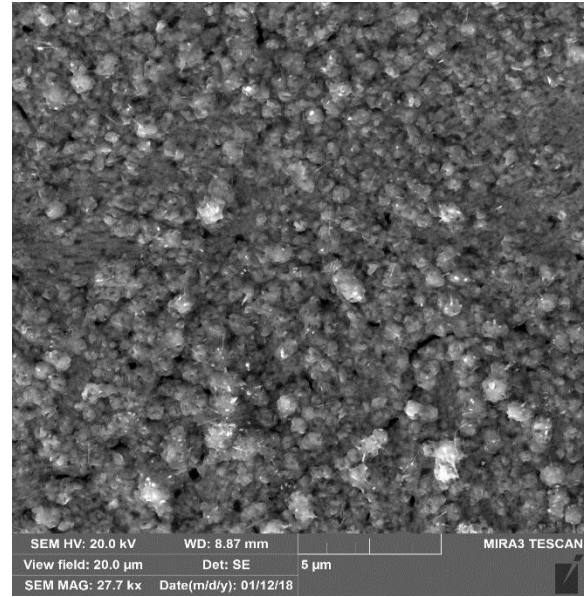

Figure 133: SEM secondary electron image of oxides created on the surface of sample 1 after heating up to 700°C (magnitude 27,7 kx)
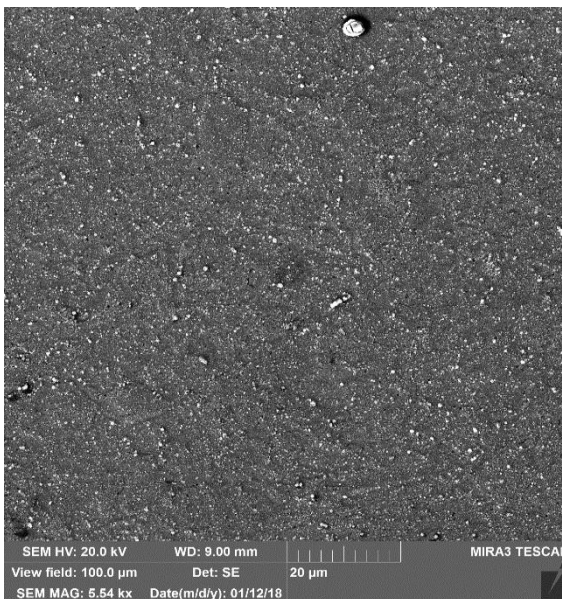

Figure 134: SEM secondary electron image of oxides created on the surface of sample 2 after heating up to 500°C (magnitude 5,54 kx)
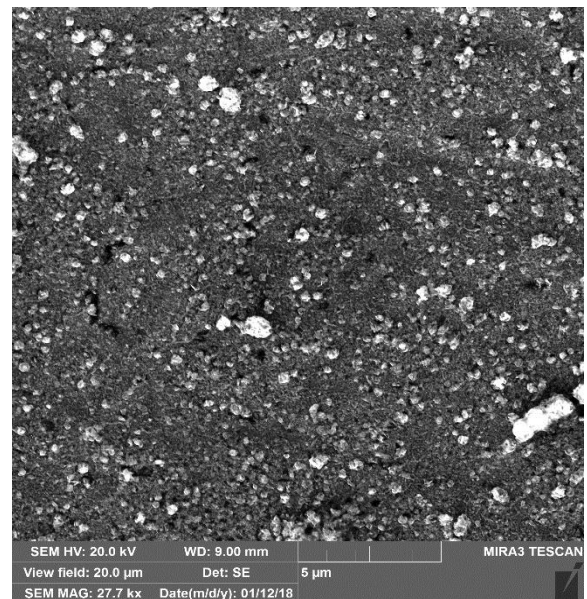

Figure 135: SEM back-scattered electron image of oxides created on the surface of sample 2 after heating up to 500°C (magnitude 27,7 kx)

4. Conclusions

4.1.   Sample preparation and microscopy

- On the contrary to the OPS polishing, the electrolytically prepared specimens showed good visibility of microstructure. LOM results showed well visible microstructure at low and high magnifications to identify the grains, grain boundaries and precipitates, which is crucial for site specific nanoindentation.

- The average surface roughness evaluated by contact microscopy (SPM, AFM) is within the limit of Ra < 30 nm required for nanoindentation

- In this thesis, the optimal method of nanoindentation specimen preparation by advanced metallography procedures was developed.

- The results from AFM scan are more appropriate to analyze the surface roughness of nanoindentation specimens in comparison to SPM method due to its smaller tip radius.

- Good visibility of the microstructure was confirmed also by SEM back-scattered and secondary electron imaging methods presented in chapter 3.3.

- Chemical composition of the specimen material EUROFER 97 was analyzed and corresponds to values found in the literature. The chemical composition comparison is given in tables 5 and 9.

- Detailed grain orientation and phase analysis were successfully determined by EBSD for both electrolytically treated areas, as summarized in chapter 3.3.2.

- In summary, principles and operation of advanced metallography techniques and advanced microscopy tools for characterizing materials structure as well as chemical analysis have been learnt.

4.2.   Calibration

- The temperature stability of xSol 800 heating stage was confirmed to be within the range claimed by the manufacturer (± 0.1°C), which is sufficient temperature stability for the nanoindentation.

- Tip area functions for standard and high load indentation tips were determined and calibrated on fused quartz. More accurate calibration of tip area function for high-temperature measurements is required in future studies, to determine values of hardness and reduced modulus at high temperatures.

- Machine compliance was determined as 1,32 nm/mN for high load head and 2,7 nm/mN for standard tip at room temp.

- A way to improve the calibration accuracy could be also a standardized sample with properties closer to the properties of subsequently nanoindented material. Due to hardness of 9.25 GPa, the indenter does not penetrate the material as deep as in case of FM steels, which might influence the calculation of tip area function as a function of indentation depth as shown in equation 2.

4.3.   Nanoindentation

- The nanoindentation at room temperature under various loads (depths) have shown the decreasing trend of hardness values with increasing load, while the reduced modulus behaved in exactly the opposite way. In both cases the values tend to level up for greater indentation depths. This might be explained by the presence of the work hardened surface layer that was induced by the mechanical grinding and OPS polishing, or a thin oxidic layer caused by oxidation. Both types of layer cause the ISE (chapter 1.6.6.) that has greater influence on low load indentation. Nanoindentation under higher loads is therefore proposed to be more suitable for determining the mechanical properties of ferritic-martensitic steels like EUROFER 97 (T91, P91, etc.).

- Electrolytically prepared specimens showed slightly lower values of hardness than OPS polished specimens at room temperature, which corresponds to assumed reduction of residual stress induced in specimen surface by mechanical grinding and polishing. Reduced modulus was determined similarly for all three indentation areas.

- Figures in chapter 3.5.2. show the average hardness and modulus of high-temperature indentation at low load and high loads with error bars representing standard deviations. A general trend of decreasing hardness with increasing temperature has been shown. A similar trend has been exhibited by reduced modulus (decreasing with increasing temperature) at low load high-temperature indentation. At high load high-temperature, reduced modulus behavior is in contradiction. This might be associated with thin oxide layer formation at test temperatures above 200 °C related to experimental technique problem. More experiments need to be conducted at these conditions to determine the root cause.

- Surface oxidation was also encountered in case of 5 mN nanoindentation at 100 and 300°C on OPS area (chapter 3.5.3. and figure 140 in the appendix). Prevention of oxidation should be further studied especially at temperatures higher than 300°C.

- The thermal drift did not have significant influence on the nanoindentation up to 300°C. For higher temperatures longer time of tip specimen contact prior the indentation would be more suitable.

- The nanoindentation also showed high sensitivity to external influences like vibrations and air circulation, which can be observed on some loading curves depicted in the appendix (the loading curve should be smooth). More attention should be therefore paid at surrounding conditions of nanoindentation.

- Concerning the tip material, the diamond tips cannot be used for indentation of steel at temperatures higher than 300°C because of their rapid degradation. Sapphire tips should be used instead.

- Corrections of the pile-up effect should be further investigated and more innovative methods should be implemented into calculations, that would regard this behaviour. The presence of pile-up was proven in chapter 3.5.3.

- In summary, during the master thesis special attention has been given to determine the mechanical properties by nanoindentation of advanced fusion – fission cross cutting material ferritic-martensitic steel EUROFER 97. High-temperature nanoindentation experiments were performed in hot-cells on nuclear grade steels first of its kind in Czech Republic.

This master´s thesis was done in accordance with the following time plan:
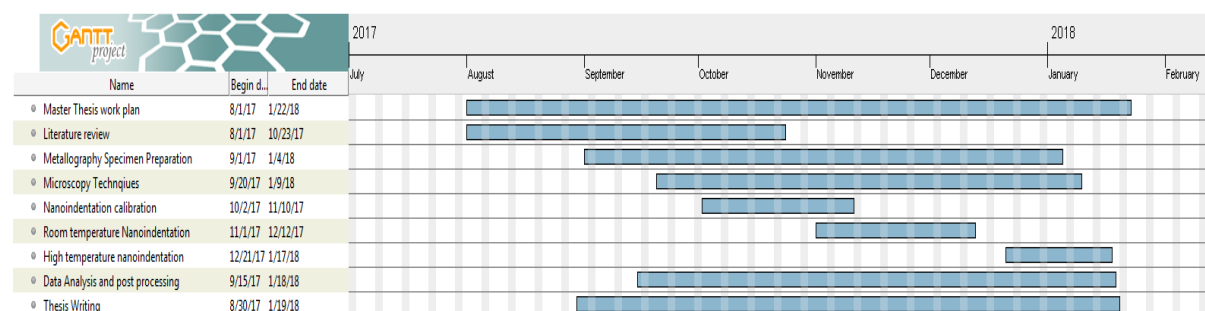
5. References

1. PRIS - Home. *IAEA Data Center - PRIS.* [Online] [Cited: August 3, 2017.] https://www.iaea.org/pris/.

2. *All America Threaded Products.* [Online] [Citace: 8. August 2017.] https://www.aatprod.com/hrf_faq/what-is-the-difference-between-austenitic-ferritic-and-martensic-stainless/.

3. Stainless Steel 304 - Alloy Composition. *ESPI Metals.* [Online] August 2017. http://www.espimetal.com/index.php/technical-data/200-Stainless%20Steel%20304%20-%20Alloy%20Composition.

4. Stainless Steel 316 - Alloy Composition. *ESPI Metals.* [Online] August 2017. http://www.espimetal.com/index.php/technical-data/202-Stainless%20Steel%20316%20-%20Alloy%20Composition.

5. Mahmoud, H., Vlasic, F. and Mazal, P. Simulation of Operational Loading of Pressure Equipment by Means of Non-destructive Testing. *Metal 2015.* [Online] July 2015. [Cited: August 10, 2017.] http://konsys2.tanger.cz/files/proceedings/21/papers/3732.pdf.

6. Jandová, D., a další. Microstructure of 08CH18N10T austenitic steel after thermo-mechanical fatigue tests. *Metal 2015.* [Online] July 2015. [Citace: 10. August 2017.] http://konsys2.tanger.cz/files/proceedings/21/papers/4132.pdf.

7. Gelles, D. S. Development of martensitic steels for high neutron damage applications. *Journal of Nuclear Materials.* December 1996.

8. Fernández, P., a další. Reduced Activation Ferritic/Martensitic Steel Eurofer´97 as Possible Structural Material for Fusión Devices. Metallurgical Characterization on As-Received Condition and after Simulated Service Conditions. *www.iaea.org.* [Online] December 2004. [Citace: 10.   August   2017.] http://www.iaea.org/inis/collection/NCLCollectionStore/_Public/36/026/36026402.pdf.

9. Tanigawa, H. et al. Development of benchmark reduced activation ferritic/martensitic steels for fusion energy applications. *Nucl. Fusion 57 092004.* [Online] 2017. http://iopscience.iop.org/article/10.1088/1741-4326/57/9/092004/meta.

10. Mateus, R. et. al. Microstructure Characterization of ODS-RAFM Steels. [autor knihy] F. Chun Chun. *Materials for Future Fusion and Fission Technologies.* 2009.

11. Cavitation in Centrufugal Pumps. *Nuclear Power for Everybody.* [Online] [Citace: 27. December 2016.] http://www.nuclear-power.net/nuclear-engineering/fluid-dynamics/centrifugal-pumps/cavitation/.

12. Wenjie, Bai, Quan, Duan a Zaoxiao, Zhang. Numerical investigation on cavitation within letdown orifice of PWR nuclear power plant. *Cience Direct.* [Online] 15. August 2016. [Citace: 27. December 2016.] http://www.sciencedirect.com/science/article/pii/S0029549316301108.

13. Light Water Reactor Sustainability Program: Materials Aging and Degradation Technical Program Plan. *Energy.gov.* [Online] September 2012. [Citace: 20. December 2016.] https://www.energy.gov/ne/downloads/light-water-reactor-sustainability-program-materials-aging-and.

14. Generic Aging Lessons Learned (GALL) Report. *U.S. NRC, Generic Aging Lessons Learned (GALL) Report — Final Report (NUREG-1801, Revision 2).* [Online] December 2010. [Citace: 27. December 2016.] https://www.nrc.gov/reading-rm/doc-collections/nuregs/staff/sr1801/r2/.

15. Zhang, Y., a další. Investigation on thermal stratification and turbulent penetration in a pressurizer surge line with an overall out-surge flow. *ScienceDirect.* [Online] 28. December 2015. [Citace: 31. December 2016.] http://www.sciencedirect.com/science/article/pii/S0306454915300153.

16. G.R. Odette, G.E. Lucas. Embrittlement of Nuclear Reactor Pressure Vessels. *The Minerals, Metals & Materials Society.* [Online] July 2001. [Citace: 27. December 2016.] http://www.tms.org/pubs/journals/jom/0107/odette-0107.html.

17. Katona, Tamas Janos. Plant life management (PLiM) practices for water-cooled water-moderated nuclear reactors (WWERs). *Understanding and mitigating ageing in nuclear power plants: Materials and operational aspects of plant life management (PLiM).* místo neznámé : Woodhead Publishing Limited, 2010.

18. Lupinacci, A., et al. Characterization of ion beam irradiated 304 stainless steel utilizing nanoindentation and Laue microdiffraction. *Journal of Nuclear Materials.* November 2014.

19. Assessment of Void Swelling in Austenitic Stainless Steel Core Internals. *U.S. Nuclear Regulatory Commission.* [Online] https://www.nrc.gov/docs/ML0607/ML060720151.pdf.

20. Tipping, Ph. G. Plant life management (PLiM) practices for pressurized light water reactors (PWR). *Understanding and mitigating ageing in nuclear power plants: Materials and operational aspects of plant life management (PLiM).* místo neznámé : Woodhead Publishing Limited, 2010.

21. *Aging Management for Nuclear Power Plants.* Vienna : International Atomic Energy Agency, 2009. ISBN 978–92–0–112408–1.

22. Material Hardness Review. *Engineers Edge.* [Online] [Cited: August 16, 2017.] http://www.engineersedge.com/material_science/hardness.htm.

23. Torres, H., Varga, M. a Ripoll, M. R. High temperature hardness of steels and iron-based alloys. *MaterialsScience&EngineeringA.* June 2016.

24. Walley, S. M. Historical origins of indentation hardness testing. *Materials Science and Technology.* October, 2012.

25. Qian, L., a další. Comparison of nano-indentation hardness to microhardness. *Surface & Coating Technology.* September 2004.

26. NanoIndentation Testing. *MechAction, Inc.* [Online] August 7, 2017. https://www.mechaction.com/nanoindentation.

27. Zinkle, S. J. and Oliver, W. C. Mechanical property measurements on ion-irradiated copper and Cu-Zr. *Journal of Nuclear Materials.* November 1986.

28. Fisher-Cripps, C. A. *Nanoindentation.* New South Wales : Springer, 2011. ISBN 978-1-4419-9872-9.

29. Liu, P. P., Wan, F. R. and Zhan, Q. A model to evaluate the nano-indentation hardness of ion-irradiated materials. *Beam Interactions with Materials and Atoms.* September 2014.

30. Oliver, W. C. a Pharr, G. M. An improved method for determining hardness and elastic modulus using load and displacement sensing indentation experiments. 1992.

31. Hoon-Seop, K., a další. A novel way to estimate the nanoindentation hardness of only-irradiated layer and its application to ion irradiated Fe-12Cr alloy. *Journal of Nuclear Materials.* 20. February 2017.

32. Merle, B., Maier-Kiener, V. a Pharr, G. M. Influence of modulus-to-hardness ratio and harmonic parameters on continuous stiffness measurement during nanoindentation. *Acta Materialia.* 2017.

33. Menčík, J. Uncertainties and Errors in Nanoindentation . [Online] [Citace: 27. November 2017.] http://cdn.intechopen.com/pdfs/40035/InTech-Uncertainties_and_errors_in_nanoindentation.pdf.

34. Nix, W. D. and Gao, H. Indentation Size Effects in Crystalline Materials: A Law for Strain Gradient Plasticity. *Journal of the Mechanics and Physics of Solids.* 1998.

35. Huang, Y, Nix, W.D. a Feng, G. A model of size effects in nano-indentation. *Journal of the Mechanics and Physics of Solids.* 2006.

36. Wheeler, J. M. a Michler, J. Review of Indenter Materials for High Temperature Nanoindentation. [Online] https://www.anton-paar.com/corp-en/products/applications/. G93-IA-041-EN-A.

37. Yabuuchi, K., a další. Evaluation of irradiation hardening of proton irradiated stainless steels by nanoindentation. *Journal of Nuclear Materials.* December 2013.

38. Li, S., et al. Evaluation of hardening behaviors in ion-irradiated Fe-9Cr and Fe-20Cr alloys by nanoindentation technique. *Journal of Nuclear Materials.* May 2016.
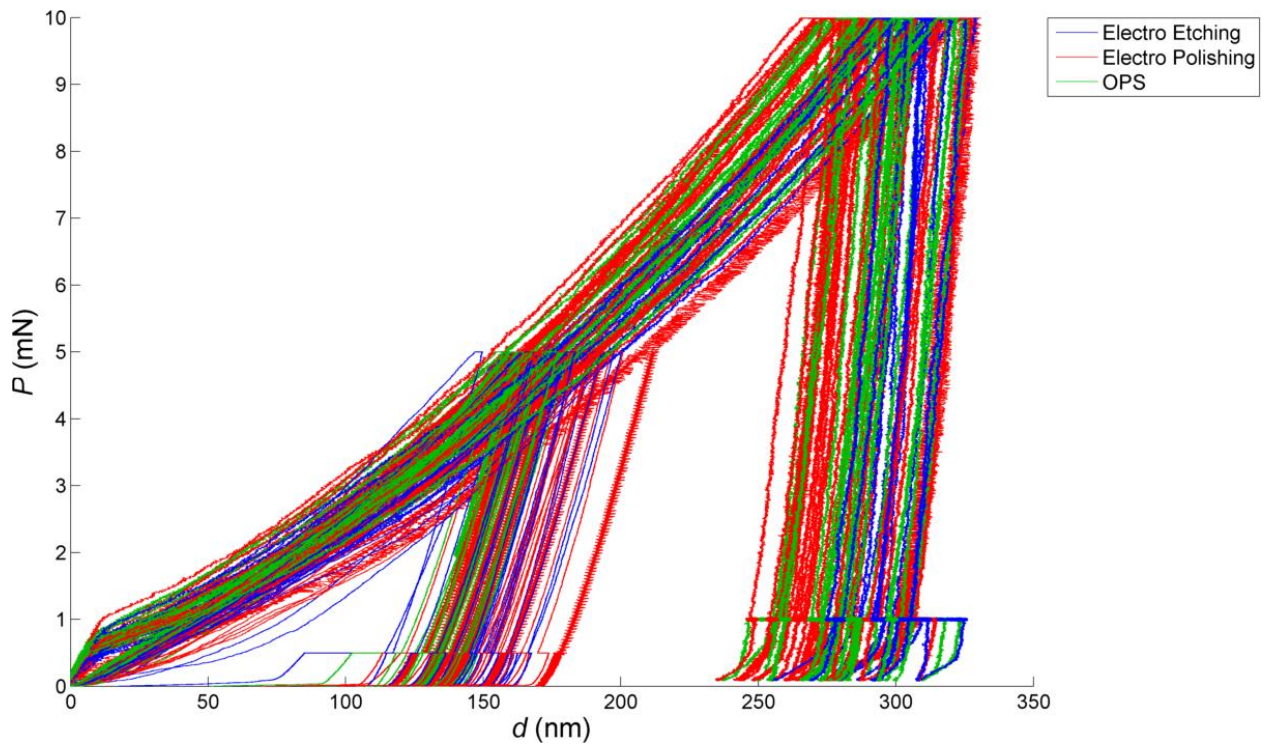
6. Appendix

Figure 136: 5 and 10 mN loading curves from indentations on all three surfaces at 23°C
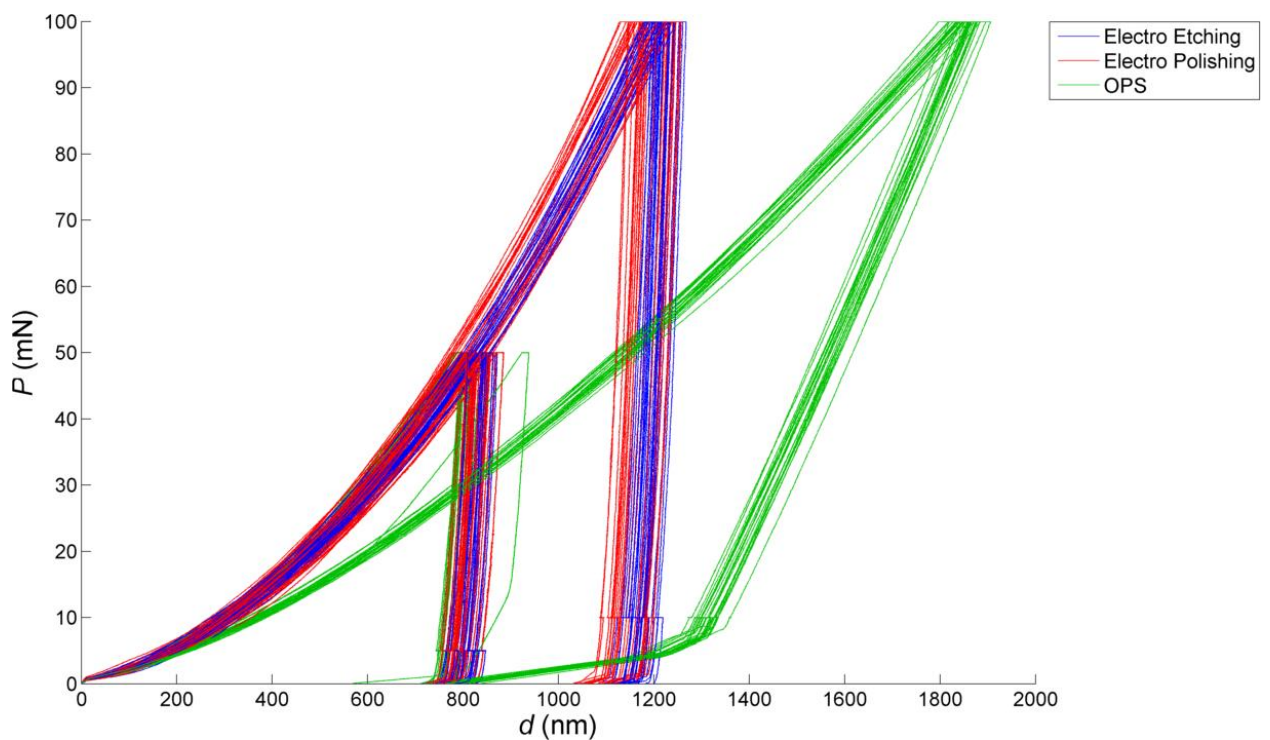

Figure 137: 50 and 100 mN load curves from indentation on all three areas at 23°C (the single green curve that goes beyond other 50 mN indents represents an unknown error that caused a shift of 100 mN indentations conducted after)
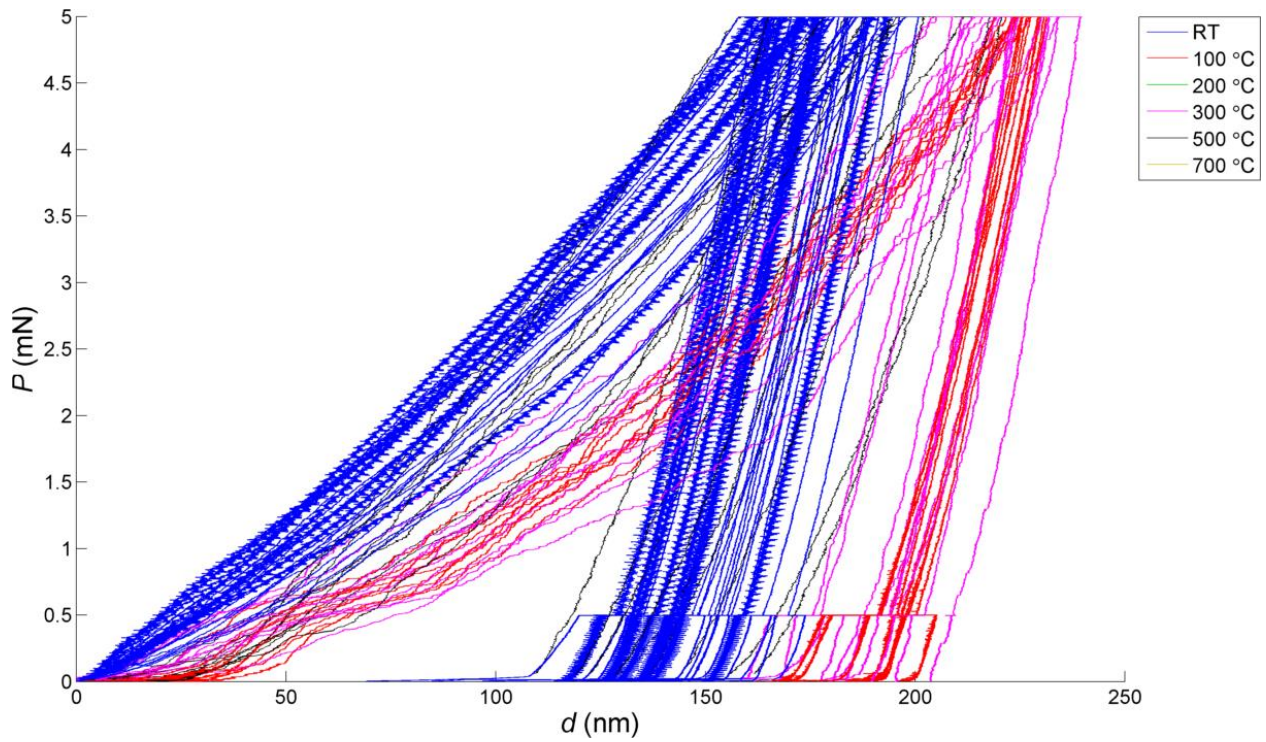
Figure 138: 5 mN indents conducted on electro polished area for temperatures from 23-500°C
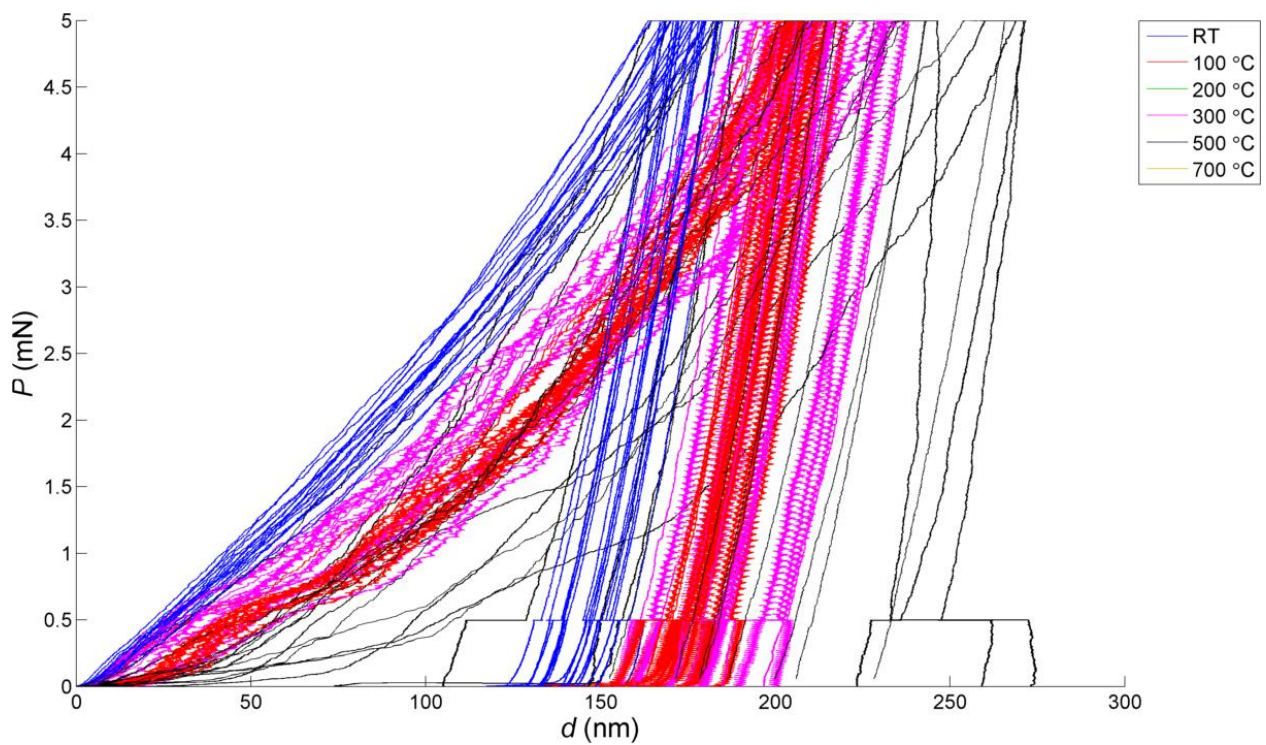

Figure 139: 5 mN indents conducted on electro etched area for temperatures from 23-500°C
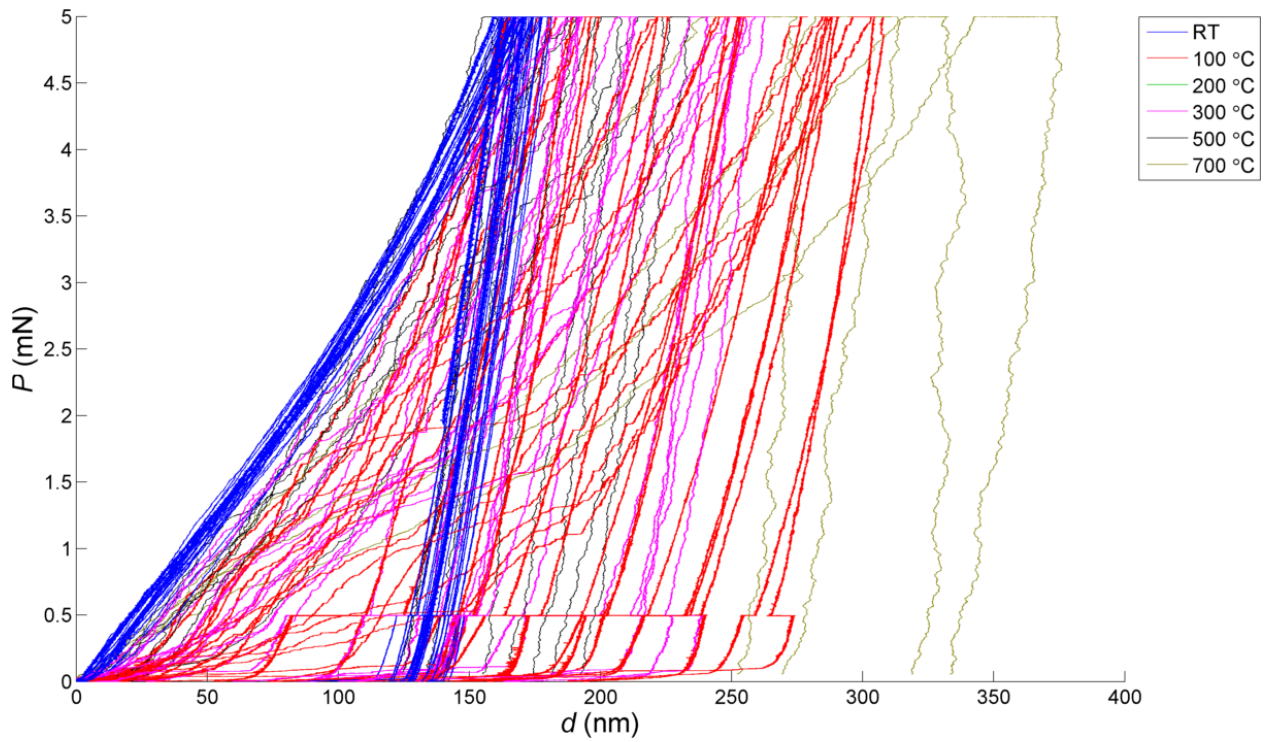
Figure 140: 5 mN indents conducted on OPS area for temperatures from 23-700°C
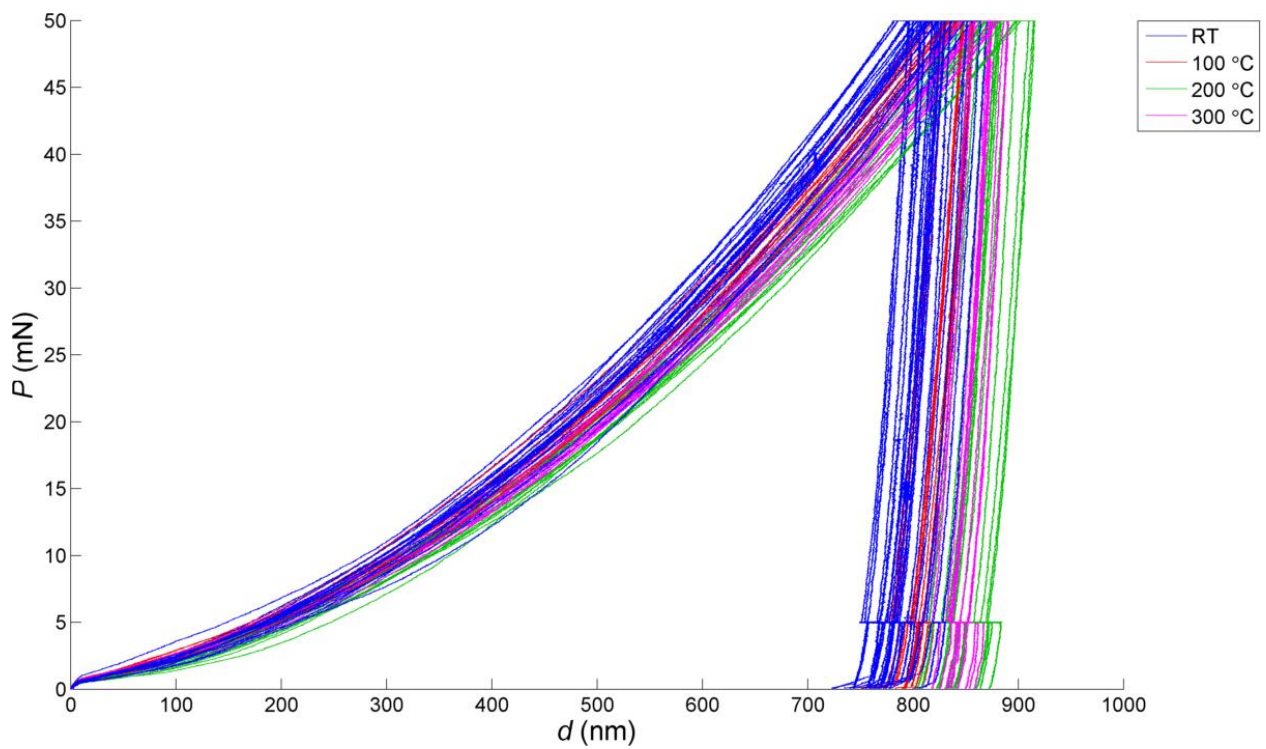

Figure 141: 50 mN indents conducted at electro polished area for temperatures from 23-300°C

Assessment of high-temperature micromechanical properties of ferritic-martensitic steels
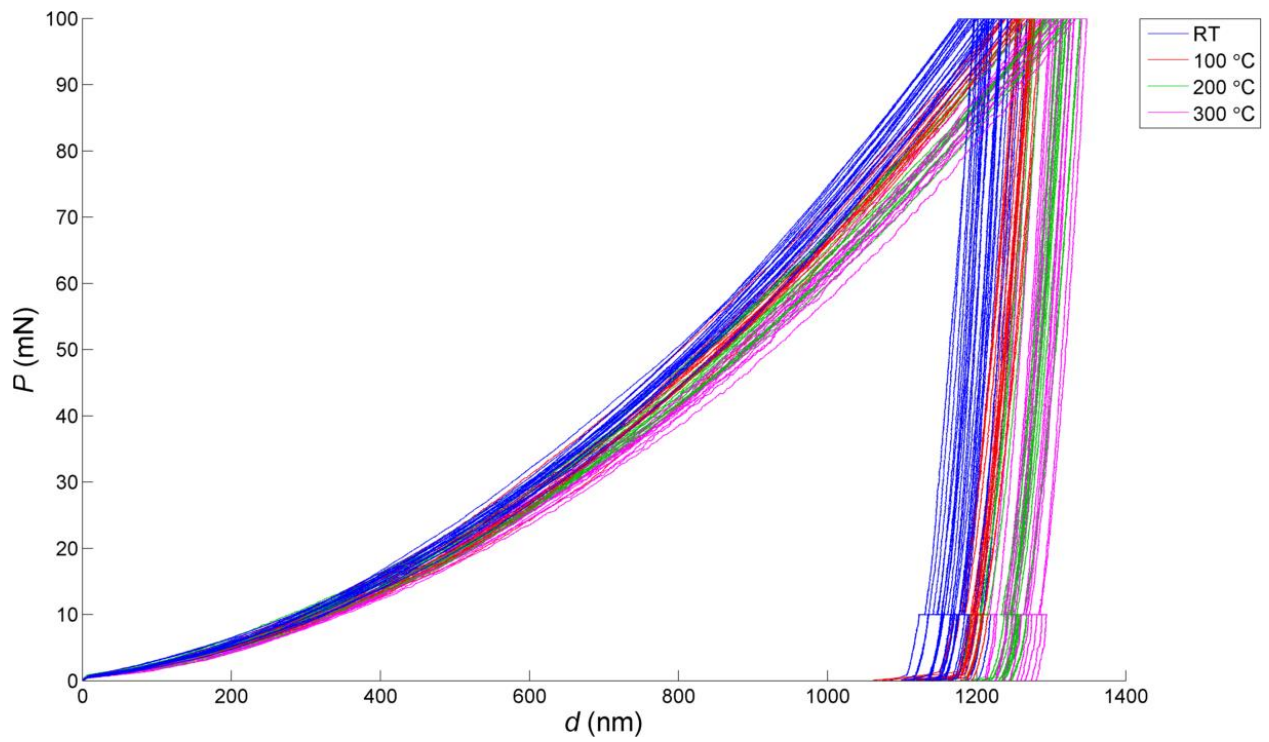by nanoindentation

94

Figure 142: 100 mN indents conducted at electro etched area for temperatures from 23-300°C